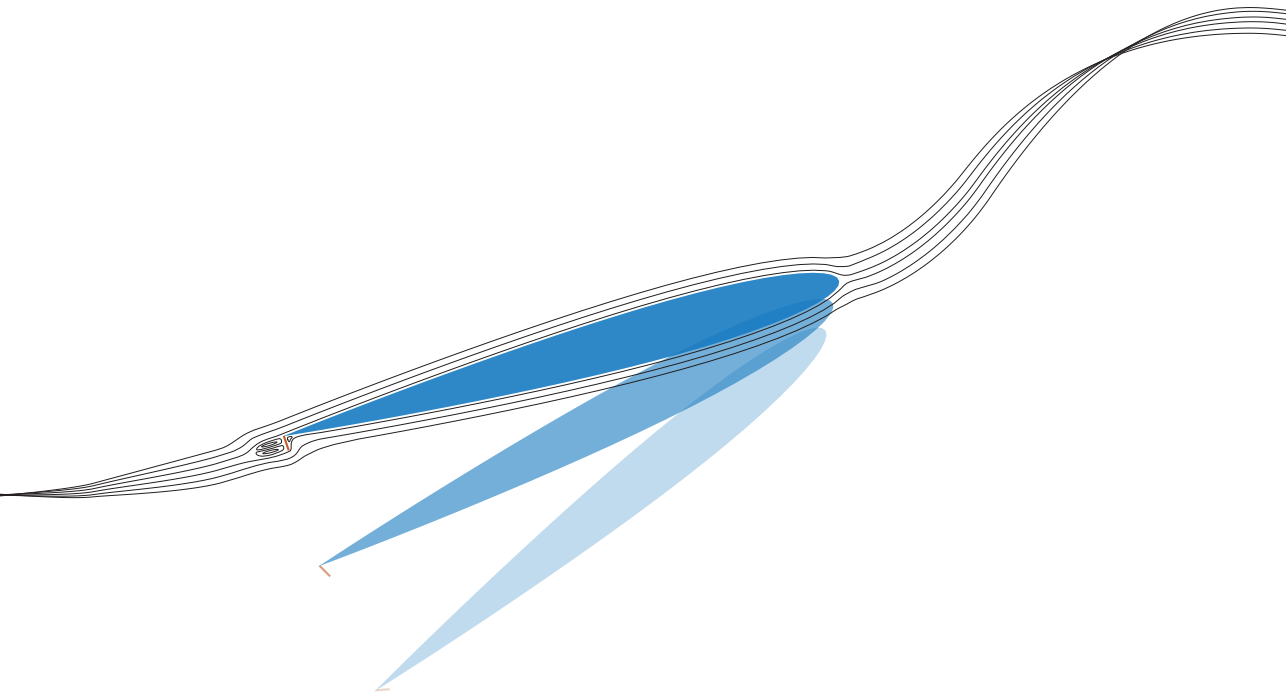


SMART ACTUATION MECHANISMS FOR HELICOPTER BLADES

Design Case for a Mach-scaled Model Blade



Alexandre Paternoster

**SMART ACTUATION MECHANISMS
FOR HELICOPTER BLADES**

DESIGN CASE FOR A MACH-SCALED MODEL BLADE

Alexandre René Alain Paternoster

**SMART ACTUATION MECHANISMS
FOR HELICOPTER BLADES**

DESIGN CASE FOR A MACH-SCALED MODEL BLADE

PROEFSCHRIFT

ter verkrijging van
de graad van doctor aan de Universiteit Twente,
op gezag van de rector magnificus,
prof.dr. H. Brinksma,
volgens besluit van het College voor Promoties
in het openbaar te verdedigen
op donderdag 28 februari 2013 om 12.45 uur

door

Alexandre René Alain Paternoster

geboren op 28 september 1985
te Lomme in Frankrijk

Dit proefschrift is goedgekeurd door de promotoren

Prof.dr.ir. A. de Boer

Prof.dr.ir. R. Akkerman

Summary

Today's helicopters are the result of collaborative work in mechanical engineering and aeronautics. The European project "Clean Sky" aims at improving the efficiency and the global transport quality of aircraft. In the field of rotorcraft, the research in this project is currently focussing on active blade systems to adapt the aerodynamic properties of the blade to the local aerodynamic conditions. Fuel-efficiency, reduction of vibration and noise and increase of the helicopter maximum speed are the benefits expected from these new technologies. To envision the implementation of these innovative blade concepts, this thesis investigates the selection process for actuators, the methods to design and optimise actuation systems and the procedures to validate them through simulations and testing.

Integrating an actuation system in helicopters is especially difficult because of a combination of challenges. To begin with, these include the tremendous loads due to the rotation of the blade, the limited space available, and constraints regarding durability. Secondly, the impact that the actuation system will have on the rotor blade behaviour has to be taken into account. And lastly, integrating the component inside the actual structure of a rotor blade should be feasible. A system based on piezoelectric actuators provides a potential solution to meet these challenges. A selection process has been established in Chapter 2 to match an actuation technology to application requirements. For the actuation of helicopter active systems, high performance "Macro Fibre Composite" actuators and Physik Instrumente patch d_{33} actuators turned out to be the best choice. The tests discussed in Chapter 3 showed the superior properties of the d_{33} patch actuator

from Physik Instrumente for the purpose of integration inside a rotor blade.

Among many of the smart blade concepts under development, the active Gurney flap is considered in the framework of the Clean Sky Innovative Technology Development project “Green Rotor Craft”, for its potential impact on the blade performance and technology readiness. Actively deploying the Gurney flap on the retreating side of the helicopter increases the lift of the rotorcraft and its overall performances. To validate this technology, numerical studies and wind-tunnel testing on reduced-scale rotor blades are necessary. The procedures detailed in this work are applied to the design of an actuation system to fold and deploy a Gurney flap for a Mach-scaled rotor blade. Additional challenges arose due to the reduction in size: the centrifugal acceleration is increased and the space available inside the blade is drastically reduced.

Computational Fluid Dynamic simulations are performed in the first step of the design procedure to obtain the aerodynamic loads on the Gurney flap for various realistic combinations of deployment levels, orientations of the blade in the flow and airspeeds (Chapter 4). Secondly, the design of the actuation mechanism is performed using a two-step approach: (1) computer generated topologies are analysed to find a suitable initial geometry; (2) an optimisation is carried out to maximise the displacement and force of the structure integrating a piezoelectric patch actuator. The resulting structure presents the characteristic shape of a “Z” (Chapter 5). It converts the strains generated by the piezoelectric actuator into relatively large displacements and delivers sufficient mechanical work at the trailing edge, where the Gurney flap is positioned. Finally, Chapter 6 describes how the mechanism is refined and connected to the Gurney flap to fully deploy and retract the flap.

A multi-domain numerical validation of the mechanism is done in Chapter 7. The aerodynamic model is combined with a multi-body simulation and an electro-mechanical finite element simulation to assess the performance of the mechanism during actual operation. The mechanism achieves sufficient authority to fold and deploy the Gurney flap under external loads caused by the rotation of the blade and the aerodynamic loads. Chapter 8 concludes this work with the prototyping of a z-shaped structure and a successful experimental verification of the geometry motion.

The z-shaped actuation mechanism developed in this thesis demonstrated great capabilities and ease of integration, while highlighting the potential of piezoelectric components in actuation systems. The development of these innovative technologies provides solutions for implementing actuation in the very demanding environments encountered in the aeronautic field and will help the next generation of smart rotorcraft to take off.

Samenvatting

Moderne helikopters zijn het resultaat van een nauwe samenwerking tussen de disciplines werktuigbouwkunde en luchtvaarttechniek. Het Europese project "Clean Sky" heeft als doel het verbeteren van de efficiëntie en de algemene transportprestaties van vliegtuigen en helikopters. Het onderzoek op het gebied van helikopters is in dit project momenteel sterk gericht op actieve systemen in de rotorbladen. Deze systemen zijn in staat om de aerodynamische eigenschappen aan te passen aan de lokale stromingscondities. De verwachting is dat deze ontwikkeling zal leiden tot een reductie in het brandstofverbruik, geluids- en trillingsonderdrukking en een toename van de maximale snelheid van helikopters. Het doel van dit proefschrift is een methode aan te reiken om deze innovatieve systemen te kunnen implementeren. Er wordt ingegaan op de selectieprocedure van actuatoren, het ontwerp en het optimaliseren van het actieve systeem en het uitvoeren van validatie en testprogramma's.

De integratie van actieve systemen in helikopter rotorbladen is bijzonder uitdagend door een combinatie van factoren. Hiertoe behoren onder andere de enorme krachten als gevolg van de rotatie van het blad, de zeer beperkte ruimte die ter beschikking staat en de eisen ten aanzien van de duurzaamheid en betrouwbaarheid van de systemen. Tevens moet het effect van het actieve systeem op de prestaties van het blad worden meegenomen en dient deze, in het ideale geval, minimaal te zijn. Vervolgens moet een dergelijk systeem goed zijn te integreren in de bestaande structuur van het blad. Op piezoelektrisch materiaal gebaseerde actuatiemechanismen hebben de potentie om aan deze eisen te voldoen. Hoofdstuk 2 beschrijft een selectieprocedure die dient om

de beste actuatortechnologie te koppelen aan een gegeven pakket van eisen. In het geval van actieve systemen in rotorbladen van helikopters bleken de "Macro Fibre Composite" actuator en de zogenaamde d_{33} -patch-actuatoren van Physik Instrumente de beste keus ten opzichte van andere actuatietechnologiën. Hoofdstuk 3 beschrijft een experimentele evaluatie van deze patch-actuatoren waaruit blijkt dat de d_{33} -actuator van Physik Instrumente de beste keuze is voor gebruik in een rotorblad.

Van alle actieve-bladsystemen die momenteel in ontwikkeling zijn, is de "Active Gurney Flap" geselecteerd in het kader van het Clean Sky Innovative Technology Development project "Green Rotor Craft", vanwege de positieve invloed op het aerodynamisch gedrag van het blad en omdat deze techniek zich in een vergevorderd stadium van ontwikkeling bevindt. Het uitklappen van de Gurney Flap tijdens de teruggaande beweging van het blad verbetert de lift van het blad en de algehele prestatie ervan. Numerieke studies en windtunnel experimenten van een schaalmodel zijn nodig om deze techniek te valideren. De in dit proefschrift aangedragen procedures worden toegepast op een actuatiesysteem dat een Gurney Flap bedient op een Mach-geschaald rotorblad. Extra uitdagingen ontstaan door het verkleinen van het rotorblad: de centrifugale belastingen nemen toe tot extreme waarden en de beschikbare ruimte binnen het blad wordt drastisch verkleind.

Numerieke aerodynamicamodellen zijn gebruikt in de eerste stap van de ontwerpprocedure om de aerodynamische krachten te verkrijgen die op de Gurney Flap werken onder verschillende realistische combinaties van uitklapniveau's van het mechanisme, stromingsrichtingen en vliegsnelheden (Hoofdstuk 4). Vervolgens wordt in een tweestapsbenadering een mechanisme ontworpen: (1) Talloze door de computer gegenereerde configuraties worden geanalyseerd om een geschikte topologie te krijgen; (2) Een optimalisatie van het ontwerp wordt uitgevoerd om de verplaatsing en de actuatiekracht te maximaliseren, gebaseerd op een geïntegreerde piezoelektrische patch-actuator. Het resultaat is een constructie in de vorm van een "Z" (Hoofdstuk 5). Dit mechanisme vergroot de door het piezoelement gegenereerde rek tot een relatief grote verplaatsing en is in staat om voldoende arbeid te leveren op de locatie waar de Gurney Flap is gepositioneerd. Als laatste wordt in Hoofdstuk 6 nader uitgelegd hoe de details van het mechanisme zijn ontworpen en hoe het mechanisme is verbonden met de Gurney Flap, zodat deze volledig kan worden in- en uitgeklapt.

Een multi-domein numerieke validatie van het mechanisme wordt besproken in Hoofdstuk 7. Het aerodynamische model is gecombineerd met een multi-body simulatie en een electro-mechanisch eindiger-elementensimulatie om de prestaties van het mechanisme te beoordelen in een werkelijke situatie. Het mechanisme presteert voldoende om de Gurney Flap in- en uit te klappen, terwijl deze onderhevig is aan de krachten die worden opgewekt door de luchtstroom en de hoge centrifugale versnellingen. In Hoofdstuk 8 wordt dit werk afgesloten met een prototype ontwerp van het z-vormige mechanisme. De verplaatsingen binnen het

mechanisme worden zo op experimentele wijze gevalideerd.

Het z-vormige mechanisme dat in dit werk is ontworpen vertoont uitstekende prestaties en is eenvoudig in het blad te integreren. Tevens demonstreert het de potentie van piezoelektrisch materiaal in actuatiemechanismen. Het ontwikkelen van dergelijke innovatieve technologieën biedt oplossingen voor de implementatie van actuatiesystemen in de veeleisende luchtvaartindustrie en zal mede zorgdragen dat de volgende generatie slimme helikopters het luchtruim zal kiezen.

Contents

Summary	v
Samenvatting	vii
Contents	xi
1 Introduction	1
1.1 Early helicopters	1
1.2 Smart helicopter blades	5
1.2.1 Flaps	
1.2.2 Morphing blades	
1.2.3 Active flow control	
1.3 Challenges of actuation system for smart blades	11
1.3.1 Weight and space constraints	
1.3.2 Mechanical constraints	
1.3.3 Reliability and environmental constraints	
1.3.4 Failure	
1.3.5 Power requirement	
1.4 Research objectives	15
1.5 Conclusion	15
1.6 Thesis outline	16

2	Performance of piezoelectric actuation systems	19
2.1	Introduction to piezoelectricity	19
2.1.1	Piezoelectric characteristics	
2.1.2	Analytical formulation	
2.1.3	Piezoelectric materials	
2.2	Piezoelectric actuators	24
2.2.1	d_{31} effect actuators	
2.2.2	d_{33} effect actuators	
2.2.3	d_{15} effect actuators	
2.3	Performance of piezoelectric actuators	29
2.3.1	Piezoelectric actuation characteristics	
2.3.2	Amplification	
2.3.3	Linear piezoelectric actuators	
2.3.4	Bandwidth	
2.3.5	Power consumption and voltage	
2.3.6	Reliability and operational environment	
2.4	Selection of an actuator technology	35
2.4.1	Mechanical work per weight	
2.4.2	Time to complete one actuation cycle	
2.4.3	Number of actuators required	
2.4.4	Toughness, fatigue and environmental conditions	
2.4.5	Power consumption and integration	
2.5	Conclusion	38
3	Performance investigation of d_{33} patch actuators	41
3.1	Introduction	41
3.2	Materials and experimental setup	42
3.2.1	Specimen manufacturing	
3.2.2	Experimental setup	
3.2.3	Determination of the actuator performance	
3.3	Results and discussion	46
3.3.1	Comparison with manufacturer specifications	
3.3.2	Comparison of the two actuator technologies	
3.4	Conclusion	49
4	The Gurney flap: aerodynamic forces	51
4.1	Introduction	51
4.1.1	Baseline blade definition	
4.1.2	Mach-scaled rotor blade	
4.2	Computational Fluid Dynamics	53
4.2.1	Theory	
4.2.2	Finite Element Model	
4.2.3	Comparison with aerodynamic data	

4.3	The Gurney flap	63
4.3.1	Meshing strategies with the Gurney flap	
4.3.2	The Gurney flap principle	
4.3.3	Aerofoil section and Gurney flap for the Mach-scaled blade	
4.4	Aerodynamic constraints on the Gurney flap	69
4.4.1	Force on the Gurney flap	
4.4.2	Maximum mechanical work required to fold the Gurney flap	
4.5	Conclusion	70
5	Actuation mechanism: design and optimisation	73
5.1	Introduction	73
5.2	Actuation selection and principle	74
5.2.1	Control strategies	
5.2.2	Deployment duration	
5.2.3	Gurney flap deployment	
5.2.4	Actuation technologies	
5.3	Geometrical investigation	77
5.3.1	Structural and spatial considerations	
5.3.2	Computer generated truss designs	
5.4	Geometry optimisation	81
5.4.1	Parametrized FEM analysis	
5.4.2	Surrogate optimisation	
5.5	Optimisation results & discussion	85
5.5.1	Optimised geometry	
5.5.2	Performance of the optimised mechanism	
5.5.3	Load path	
5.6	Conclusion	90
6	Refinement of the deployment mechanism	93
6.1	Introduction	93
6.2	Refinement of the flexible mechanism	95
6.2.1	Flexible hinges for the bending arms	
6.2.2	Modelling the contact on the profile skin	
6.2.3	Performance improvements	
6.3	Deploying and folding the Gurney flap	99
6.3.1	Final design of the Gurney flap deployment system	
6.4	Conclusion	105
7	Dynamic simulation	107
7.1	Introduction	107
7.1.1	A multi-domain problem	
7.1.2	Simulation environments	
7.2	Multi-body simulation – Rigid blade simulation	109

7.2.1	Model	
7.3	The Gurney flap mechanism – Constraints calculations	113
7.3.1	Inertia loads on the mechanism	
7.3.2	Aerodynamic loads	
7.4	The mechanism validation	115
7.4.1	FEM transient analysis – Mechanism simulation	
7.4.2	Results	
7.4.3	Additional research	
7.5	Conclusion	117
8	Prototyping	119
8.1	Introduction	119
8.1.1	Spark erosion	
8.1.2	Geometry modifications	
8.2	Prototype manufacturing and testing	121
8.2.1	Experimental setup	
8.2.2	Results	
8.3	Conclusion	124
9	Conclusions and recommendations	125
9.1	Conclusions	125
9.2	Recommendations	127
	Nomenclature	129
	Appendices	132
A	Mesh convergence for CFD simulations	133
A.1	Introduction	133
A.2	CFD simulation convergence	134
A.3	Computation time	134
A.4	Conclusion	136
B	The ordinary Kriging model	137
	Bibliography	139
	Publications	153
	Acknowledgements	155

Introduction

1.1 Early helicopters

The first helicopter to successfully achieve stable hovering flight and decent forward flight performances was demonstrated in 1935 and is attributed to Louis Breguet and René Dorand [1] as shown in Figure 1.1. Their patent details the two coaxial counter-rotating blades which resulted in an unprecedented level of performance, stability and safety for a rotorcraft [2]. This success was soon matched by other helicopter pioneers. Henrich Focke at the Focke Wulf Company and Juan de la Cierva at the Weir company demonstrated the hovering capabilities of a side-by-side rotor configuration in 1936 and 1938 respectively [1, 3, 4]. In 1940 Sikorsky flew a single rotor helicopter configuration with three auxiliary tail rotors to negate the counter-torque effect [1, 5] as shown in Figure 1.2. Sikorsky refined his design and produced a significant number of helicopters during World War II, some of which were used in the Pacific theatre [1]. After the war, this configuration was widely adopted across the growing helicopter industry. Today almost every helicopter uses a single-rotor configuration.

These successes and the birth of the modern helicopter are the results of the convergence of technology, knowledge and experience. Before the Breguet and Sikorsky flights, many aircraft enthusiasts and pioneers built complex contraptions that merely hopped a few metres. In the 1930s, engines were refined by the booming aircraft industry. They were delivering unprecedented power-to-weight ratios [3], enabling helicopters to sustain hovering flights more efficiently. Besides the Breguet design, other inventors used two and even quad-rotor configurations

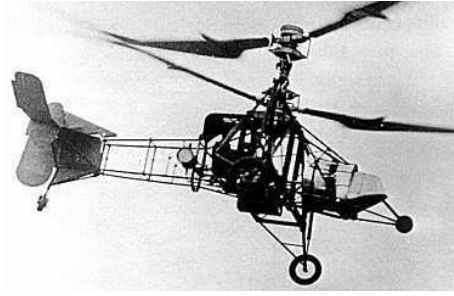


Figure 1.1: Picture of the Breguet-Dorand helicopter.

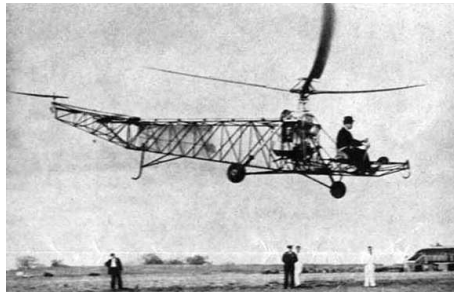


Figure 1.2: Picture of Sikorsky VS300 prototype.

to tackle the counter-torque effect [1, 4, 6]. Patents show the level of engineering that was achieved to overcome the complexity of the various designs. However, successful machines came when mature engine and mechanical technologies met scientific study and a good understanding of the specificity of helicopter aerodynamics. When hovering, each blade experiences the same distribution of incident airflow velocity. This distribution is linear and proportional to the blade radius and the blade rotation. The lift generated by each blade can be estimated using the lift formula for the lift generated by an aerofoil section f_l :

$$f_l = \frac{1}{2}c\rho v^2 c_l \quad (1.1)$$

where c is the chord length of the profile considered, ρ is the density of the air, v is the velocity of the airflow on the profile and c_l is the section lift coefficient. The section lift coefficient is a function of the pitch angle of the blade. Assuming the helicopter is hovering, the pitch angle and the airspeed distribution are the same regardless of the position of the blade relative to the helicopter. The lift force of each blade F_l is obtained from the integration of the lift formula along the length R of a helicopter blade:

$$F_l = \int_0^R \frac{1}{2} c \rho c_1 (\omega r)^2 dr \quad (1.2)$$

where ω , the rotational velocity of the blade as shown in Figure 1.3.

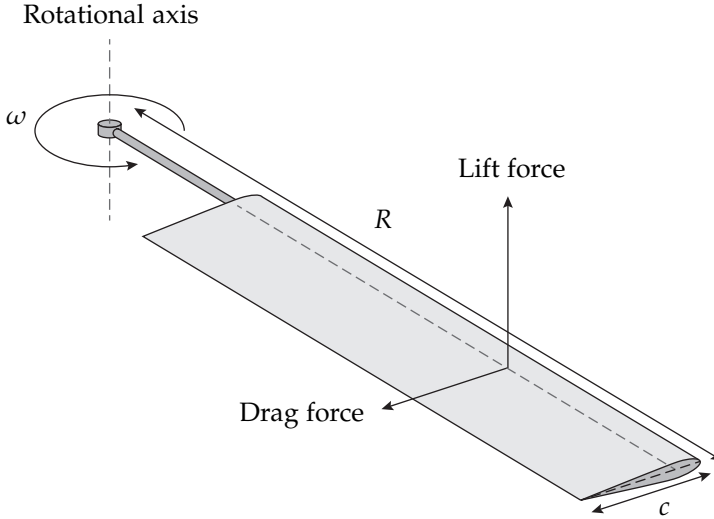


Figure 1.3: Sketch of a rotor blade under rotation.

After integration, the lift is obtained for one blade, assuming c and c_1 are constant along the length of the blade:

$$F_l = \frac{1}{6} c \rho c_1 \omega^2 R^3 \quad (1.3)$$

As soon as the helicopter goes forward an extra velocity component is added to the velocity profile [7, 8]. We can distinguish the retreating side where the blade motion points in the opposite direction of the helicopter motion and the advancing side where the blade motion is in the same direction as the helicopter motion as shown in Figure 1.4. Therefore, the incident airflow speed is increased on the advancing side and reduced on the retreating side. This asymmetry causes a difference in the lifting capabilities of the two sides. The lift for a blade in the retreating side becomes:

$$F_l = \int_0^R \frac{1}{2} c \rho c_1 (\omega r - v_n)^2 dr \quad (1.4)$$

where v_n is the air velocity component normal to the blade induced by the helicopter motion and ω is the rotational velocity of the blade. The v_n value is depending on the position of the blade element over the lifting surface as well as

the angle between the profile and the airflow. After integration along the length of the blade, the lift results in:

$$F_l = \frac{1}{2} \rho c C_l \left(\frac{1}{3} \omega^2 R^3 - \omega v_n R^2 + v_n^2 R \right) \quad (1.5)$$

The difference between equations 1.3 and 1.5 gives the loss of lift Δ_{F_l} on the retreating side due to the helicopter overall motion:

$$\Delta_{F_l} = \frac{1}{2} \rho c C_l \left(v_n^2 R - \omega v_n R^2 \right) \quad (1.6)$$

The quadratic relation between the loss of lift on the retreating side and the helicopter forward motion velocity shows the importance of this phenomenon. Reverse flow is another important consequence of the forward motion of the helicopter. It happens where the helicopter speed is larger than the velocity of the blade due to its rotation. At high speeds, this region can cover a significant portion of the blade, meaning most of the lift is generated by the outer part of the blade. A cyclic control input was the key to balance the lift. Breguet-Dorand aircraft as well as Cierva and Sikorsky helicopters used a swashplate to vary the pitch of each blade during revolution [1, 5, 9, 10]. Modifying the pitch of the blade changes the angle of attack and thus the lift for various positions of the blade around the helicopter. The angle of attack is increased on the retreating side and decreased on the advancing side. The lift is therefore evened out on the two sides of the helicopter. Other early rotorcraft pioneers considered a change of the twist of the blade or the deployment of flaps at the trailing edge of the blade to control the lift [1, 11].

Today, all helicopters use cyclic pitch control for tuning the lift as the blades rotate. But lift can only be maintained by improving the angle of attack up to the stalling point of the blade profile. The maximal speed of a rotorcraft is therefore limited to the amount of lift the rotor blade can develop on the retreating side. In the case of a rotor blade, the stall is dynamic, due to the unsteady nature of the flow. The vertical motion of the blade along with time-dependent pitching moments allows the angle of attack of the blade to exceed the quasi-static stalling angle of the profile. This effect is followed by the development of vortices close to the leading edge which can move towards the trailing edge causing large downward pitching moments [1, 7, 8]. Consequently, the rotor performance and the stability of the aircraft are reduced.

To further improve the helicopter blade performance, adaptive blade concepts are studied. The aim is to adapt the aerodynamic characteristics of the blade to maximise performance on both the advancing and the retreating side of the blade and improve the stall performance for large angles of attack. These systems range from changing the shape of a full blade profile to smaller devices acting on the boundary layer of the airflow to control its separation.

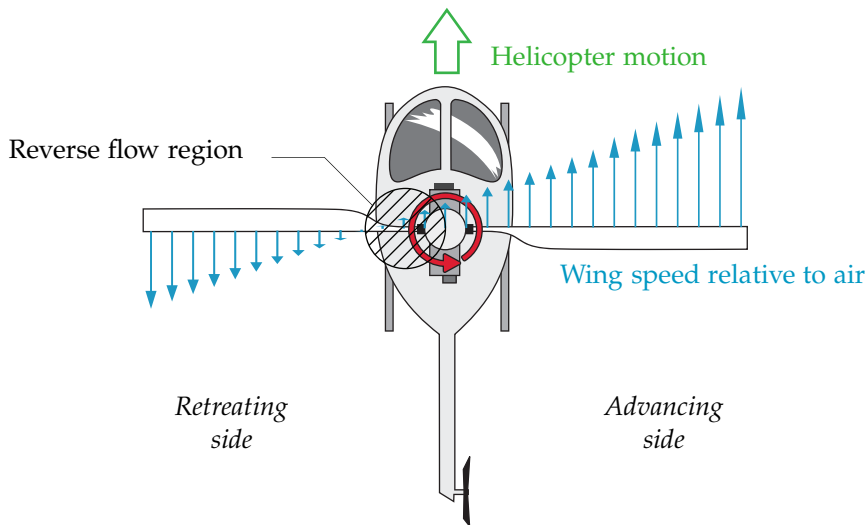


Figure 1.4: Helicopter in forward flight.

1.2 Smart helicopter blades

Smart helicopter blades integrate active systems to adapt the blade characteristics depending on localised conditions encountered in flight. Smart blades can greatly enhance the performances of modern helicopters by modifying the aerodynamic characteristics of a blade profile for a short time to provide an optimised performance across the full blade revolution. Most concepts improve the lift of the blade to cope with the lift unbalance on the retreating side. Other systems increase the helicopter efficiency by improving the stall behaviour of the profile or by reducing the vibrations on the rotor. Vibrations decrease the effectiveness of a helicopter blade, influence its dynamic stall and generate noise. The latter is a great concern for helicopters operating in an urban environment. Smart systems can be classified by their means to affect the aerodynamics of the blade. Flaps modify the flow using tabs and slats, morphing systems change the shape of the blade in a continuous manner and flow control mechanisms act directly on the flow around the blade.

1.2.1 Flaps

Flaps on helicopter blades are not designed as a primary control surface like airplanes. They act as a secondary control to improve the efficiency of the rotor blade by modifying the lift of the blade and by reducing vibrations on the rotor.

Active trailing edge flaps

Active trailing edge flaps are flaps situated at the trailing edge that actively modify the rotor blade performance. A schematic of a trailing edge flap for a helicopter blade [12] is shown in Figure 1.5. Although research has been conducted to study the possibility of using them for control in a swashplateless configuration [13], most of the studies focus on the ability to reduce the vibrations of helicopter blades [12, 14, 15, 16, 17, 18, 19]. The angle of the flap directly relates to a change of the bending of the blade during rotation [12, 18]. These flaps only need a few degrees of deflection to affect the system dynamics [12, 15]. Loads on the helicopter rotor are a function of the rotational frequency of the blade. The largest loads occur at 1, 2, 3 and 4 times the rotational frequency of the blade [7]. Therefore the flaps need to be actuated at similar frequencies to cancel undesired vibrations. With multiple flaps, the phase between the flaps is another key element. Under a suitable control authority, the literature shows that the vibratory loads on the rotor can be reduced up to 80% [15, 18]. Finally, the position of the flaps along the rotor has a great influence on the final performances of the mechanism. Although the optimum positioning of the flap depends on the application objective, studies show that multiple flaps achieve a better vibration reduction than a single flap [17, 18, 19].

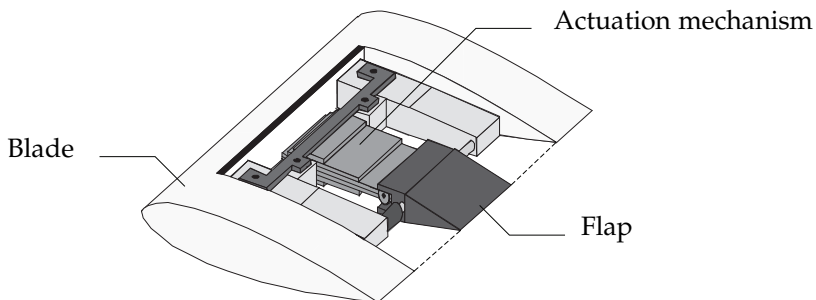


Figure 1.5: Schematic of a trailing edge flap and its actuation system (adapted from [12])

The amount of noise generated by helicopters is another important issue, especially because many helicopter missions involve flying over densely populated areas. Noise generated by the helicopter blade comes mainly from the interaction between one blade and the vortices generated by the previous blade [20]. This phenomenon is called blade-vortex interaction (BVI). Decreasing the effects of blade-vortex interaction can not only lead to a reduction in the noise emitted, but also to a decrease in the power requirement. Active trailing edge flaps are studied to limit this effect by an individual control on each blade [16, 18, 20]. Controlling the trailing edge flap at 2/rev shows potential for consequent noise reduction [16].

The Gurney flap

The Gurney flap is a small trailing edge flap deployed at 90 degrees with respect to the chord line of the profile, as shown in Figure 1.6. The Gurney flap modifies the flow at the blade trailing edge and induces a low pressure zone which brings the separation point closer to the trailing edge [21]. The result is an increase of the lift over a large range of angles of attack with a small drag penalty [21, 22, 23, 24]. Although the Gurney flap induces a pitching moment, it provides a beneficial improvement of the efficiency of the rotor blade profile for the hovering situation [23]. In forward flight, the Gurney flap provides the blade with additional lift on the retreating side to balance the lift distribution [22]. For large forward velocity, the Gurney flap improves the aerofoil behaviour in light stall conditions, which directly increases the flight envelope of a helicopter [23]. The behaviour of the Gurney flap is related to its length and placement. Studies about the length of the Gurney flap show an increase in drag and pitching moments with increasing lengths [21, 23, 24, 25]. Depending on the application, the Gurney flap length will be limited to the point where these disadvantages outweigh its benefits in lift and stall characteristics. Typically its length is 2% of the chord length of the blade profile.

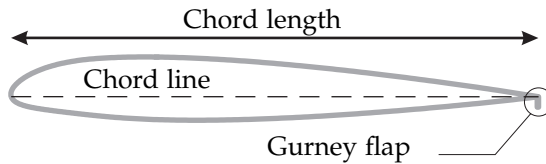


Figure 1.6: Sketch of a NACA 23012 profile with a 2% Gurney flap.

Furthermore, the Gurney flap can have a positive effect on blade-vortex interaction. Similarly to a trailing edge flap, the Gurney flap acts on the blade mechanical behaviour [23]. Actuating the Gurney flap at 4/rev and with suitable control would lead to a decrease in vibration and noise similar to active trailing edge flaps [20, 26, 27].

1.2.2 Morphing blades

The idea behind morphing blades is to change the aerodynamic characteristics of the blade by a continuous change in its shape, therefore mimicking the way birds and flying animals are modifying their wings to adapt to the various situations they encounter while flying. Most of these solutions involve a stiff structure that supports the loads and a flexible skin to keep the outer surface of the rotor blade without discontinuities. The shape modification must affect the profile sufficiently to alter its characteristics while maintaining stability and control. Eligible changes of the profile can be obtained by affecting the camber of the profile, changing the

chord length or modifying the cross-section orientation along the blade span to create a twist.

Variable droop leading edge

The concept behind the nose droop is to advance the front part of the profile at an angle. It increases the profile curvature, as shown in Figure 1.7. The variable droop leading edge (VDLE) is used to alleviate the dynamic stall by ensuring that the flow passes smoothly over the leading edge for high angles of attack [28]. Although the lift is increased during the downward motion of the leading edge [28], the maximum lift is reduced by 10% [29, 30, 31]. More significantly, the drag and pitching moments are reduced by 50% [31]. The variable droop leading edge concept provides a decrease in helicopter vibrations and loads due to the suppression of dynamic stall within the retreating blade region. However, the helicopter maximum speed is reduced due to a decrease in lift when the droop nose is deployed. Therefore, the variable droop leading edge is studied in combination with the Gurney flap to negate the lift reduction [32]. This concept can also be applied to reduce the noise generated by a helicopter [33].

Basic VR-12



Drooped VR-12

Figure 1.7: Sketch of the VR-12 profile used for wind tunnel testing at NASA Research Center from Lee paper [28].

Camber change

Changing the camber of a profile increases its lift for the same chord length [34]. The benefit is a larger flight envelope of the helicopter by improving the lift on the retreating side of the rotorcraft in the same way as the Gurney flap concept. Once again, harmonic actuation at 2/rev can reduce the noise and the vibratory loads on the rotor, improving the rotor performance [18, 35]. Most studies on this concept consider the airplane as the main application, envisioning morphing flaps as a main control surface [36]. Like many aeronautic technologies, the application is always

focused first on fixed-wing test and airplane where the flow is well understood. However, changing the camber of a helicopter rotor blade can potentially combine the benefit of many smart-blade concepts described previously such as the variable droop leading edge and the Gurney flap.

Active twist

Among early helicopter prototypes, some considered cyclic twist control [11] for changing the lift of the rotating blades. The idea behind active twist is to modify the twist and the torsional stiffness of the rotating blade not only to improve the lift and the global helicopter performance but also to actively damp vibrations. Early experiments on active twist involved changing the twist of the helicopter blade at the root of the blade [37]. Later experiments used a distributed actuation system to modify the blade twist [38, 39, 40, 41]. In a similar manner to the active trailing edge, the placement and the number of actuators modify the amount of vibration that is reduced. Thakkar's study [40] shows that up to 69% of reduction in vibrations can be achieved with the actuation of two sections. Wind tunnel tests on a model helicopter demonstrated a 95% reduction in vibrations [38]. Each of the four model blades mounted on the helicopter was equipped with 24 actuators bonded onto the skin of the blade. Torsional vibrations at 3/rev and 5/rev were successfully damped by changing the pitching angle of the blade by only 1.4 degrees. In addition, the noise generated by the blade-vortex interaction can be reduced by up to 90% using an appropriate control of the blade twist [42].

Extended trailing edge

The amount of lift a blade can deliver depends on its surface area. The lift is proportional to the blade chord length as shown in equation 1.1. Therefore, extending the chord length of a profile increases the lift generated. Studies on extended trailing edge active blades have shown an increase in the lift without significant increase in the lift-to-drag ratio [43]. A helicopter can benefit from an increase in lift on the retreating side as mentioned before. The limitation of this concept is the increase of the drag that hinders the blade efficiency.

1.2.3 Active flow control

Active flow control devices take another approach to improve the lift on a profile. Instead of modifying the aerofoil geometry to act on the flow, they directly modify the air flow by re-energising the boundary layer on the top of the profile with a high speed jet. Such a flow is called a synthetic jet. Lift is not generated by the portion of the blade in the turbulent region, situated after the separation point. The objective is to bring the separation point closer to the trailing edge and therefore improve flow over a larger portion of the aerofoil [44, 45]. Actuators for this application are placed inside a cavity which has a tiny opening [46] or a full slot perpendicular to

the flow direction on the top part of the blade [47]. Figures 1.8 and 1.9 show these two types of synthetic jet actuator. An alternative approach is to accelerate the flow by means of a plasma obtained with high voltage electrodes [48].

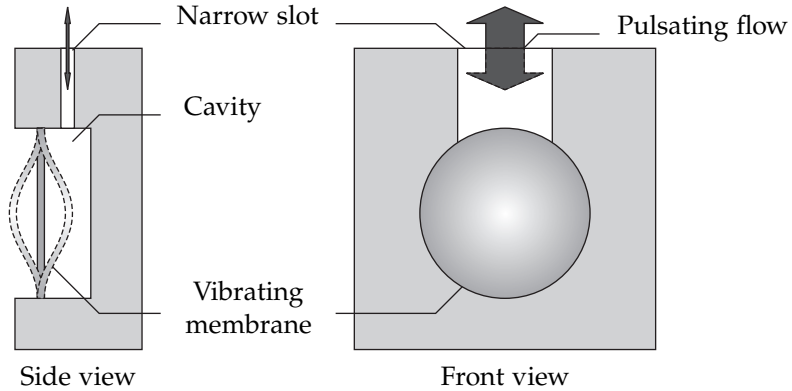


Figure 1.8: Sketch of a slot synthetic jet system.

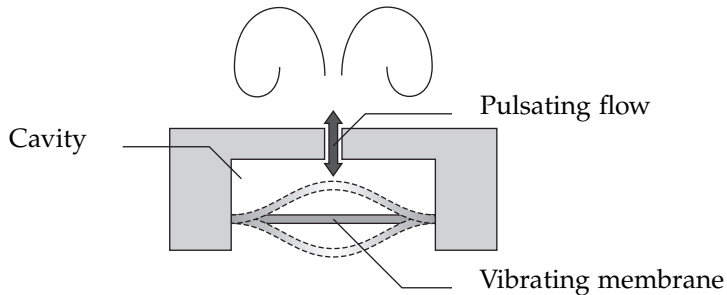


Figure 1.9: Sketch of a synthetic jet system with a circular orifice.

Wind tunnel experimentations have shown that synthetic jets improve the aerodynamic performance when driven at a specific frequency [44]. Much better performance is obtained when the actuation mechanism is combined with sensor arrays before and after the position of the synthetic jet system [49]. The sensors monitor the instabilities that will trigger the flow transition and actuate the synthetic jet system so that it damps the instabilities further delaying the transition. The actuation frequencies are in the kHz range and are related to the airflow speed [50]. Most of the literature focuses on fixed-wing wind tunnel tests [50] but simulations show a potential increase in the maximum lift of an aerofoil by 34% with an increase in the maximum stall angle of a profile [51].

These characteristics make synthetic jet systems very promising for improving the characteristics of a profile for helicopter applications.

1.3 Challenges of actuation system for smart blades

Smart systems suitable for rotorcrafts need to answer challenges specific to the integration in helicopter blades. This section details the problems arising from the weight and space taken by the mechanism, the mechanical constraints due to the blade motion and constraints related to the long-term operation of an actuation system. The combination of these challenges is the main constraint that makes smart-blade concepts very difficult to design.

1.3.1 Weight and space constraints

Helicopter blades are designed to handle large centrifugal loads. The structural material takes up most of the section of a rotor blade. Carbon fibre composites provide strength in the direction of the blade and external reinforced layers give the blade impact resistance. The only space available is in the tail of the profile. Therefore, it is very difficult to integrate a system directly in the rotor blade skin for structural reasons. Additional weight from an active system should be limited, and its distribution in the profile must not affect the chordwise balance of the blade. Therefore, it is critical to compensate any weight added behind the aerodynamic centre by an extra mass in the leading edge. For the whirl tower test of the "SMART" active flap rotor, weight was added in the leading edge to maintain the blade balance [52]. This constraint makes distributed and light systems like the active twist very relevant to maintain the distribution of mass across the profile chord. In comparison, the variable droop leading edge requires a very heavy mechanism to deform the leading edge of the profile that would heavily change the weight distribution around the aerodynamic centre [53].

1.3.2 Mechanical constraints

The large rotational speeds of the blades result in significant centrifugal accelerations and centrifugal loads. The centrifugal acceleration a is given by:

$$a = \omega^2 r \quad (1.7)$$

where ω is the rotation speed of the blade in rad/s and r is the position along the length of the blade. An 8 m rotor blade rotating at 250 rpm will generate close to 560 g of acceleration at the tip. The active system needs to be placed near the tip of the blade to maximise the effect on the blade aerodynamics. However, this location is subjected to the largest centrifugal acceleration. The resulting centrifugal loads depend on the mass of the actuation system. Obviously, a very light system does

not lead to large loads. Some actuation systems designed for micro-positioning only measure a few cm in length and are very robust. For instance, the “Squiggle” linear drive motor, developed by NewScale technology, features a shock resistance of 2500 g [54, 55]. For larger mechanisms most of the designs limit the load transfer along the blade length [52, 56, 57]. The designs can be approximated to a two-dimensional structure that is extended along the blade axis. For distributed systems that use patch actuators bonded onto the structure, like the active-twist technology developed by DLR, the actuators are being supported by the blade structure [41]. The main concern with these actuators is related to the deformation of the blade during its rotation. The peak strain at the surface of the blade must not exceed the maximum strain of the actuator as this will lead to fracture or debonding.

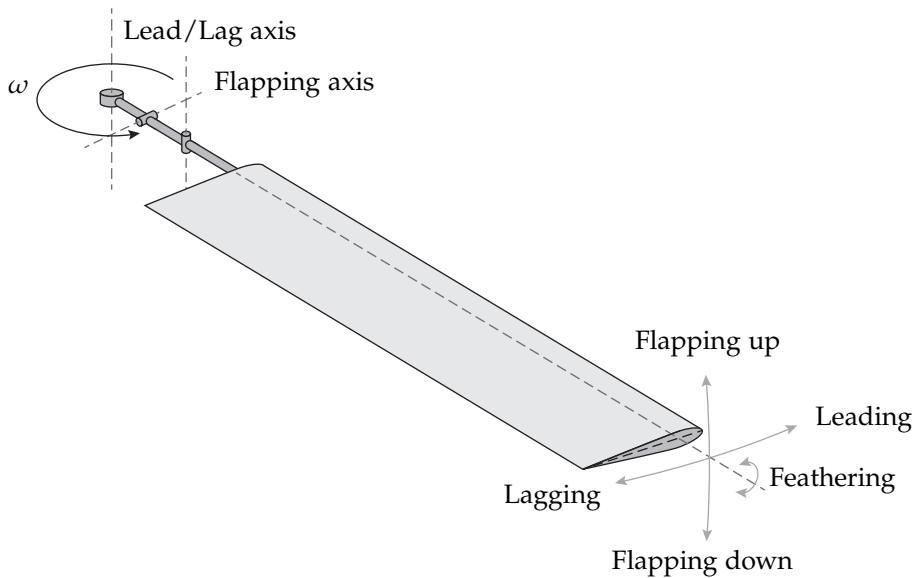


Figure 1.10: Degrees of freedom of a typical rotor blade

In addition to the centrifugal loads, helicopter blades are subjected to large vibrations. In the most common configuration, helicopter blades are attached to the rotor by a joint that allows rotation in three degrees of freedom. The motion of the blade relative to the joint is defined as flapping, lead-lagging and feathering as shown in Figure 1.10. Each is associated with one degree of freedom. While the blade is rotating, the cyclic loads excite each degree of freedom causing vibrations at frequencies that are multiples of the blade rotational frequency [7, 8]. As a consequence, the design and the orientation of mechanical elements like hinges

and friction surfaces must address both the centrifugal and dynamic loads to avoid jamming and premature failure.

1.3.3 Reliability and environmental constraints

Any mechanism built in a commercial aircraft must comply with a set of rules to ensure the reliability of the system after a large number of actuation cycles. Moreover, the system must ensure the safety and the integrity of the aircraft in the event of a failure. Helicopter blades in a general purpose helicopter are designed for 10,000 flight hours [58]. Although composite blade design can handle even more loading cycles, manufacturers specify helicopter blades to be maintained and replaced on a much shorter basis [58, 59]. Actuation mechanisms for the active blade need to have a design life superior to the blade design life and have to maintain performance through their operational life. In aircraft, hydraulic and pneumatic mechanisms are widely used due to these concerns. They are especially utilised for moving control surfaces that must satisfy a reliability requirement of 10^{-9} failure per flight hour and their performance is hardly affected even after a large number of cycles. It is only recently that electrical mechanisms have reached equivalent levels of safety and have been used to drive control-surfaces in aircraft [60].

Table 1.1: Comparison of the lifetime of an 10^9 cycles actuation mechanism in a 250 rpm rotor blade system for various active control concepts. For the active flow control system, the system is in operation only on the retreating side of the helicopter.

Active concept	Actuation frequency	Lifetime
Retreating side actuation	1/rev	66,460 hours
BVI noise	2/rev	33,230 hours
Vibrations	4/rev	16,615 hours
Flow control	2 kHz	278 hours

The reliability of the actuation system also depends on the application type. For alleviating the lift asymmetry on the retreating side, the mechanism performs a cycle once per revolution. This figure is small compared to an actuation system for actively cancelling vibrations that need to operate at 2/rev and 4/rev or even at 5/rev in the case of torsional frequencies [18, 38]. Table 1.1 shows the various expected lifetimes for a mechanism that has been designed for 10^9 cycles in the case of various active blade concepts for a 250 rpm rotor system.

Although the vibration damping case satisfies the 10,000 hours of operating life, a high quality actuation system certified for 10^9 is requested to obtain an operating life close to that of the blade. Therefore, it would be very difficult to qualify an

actuation system for damping vibration at 6/rev. For flow control devices, actuators with a significantly higher quality are required to be certified for active flow control.

Finally, helicopters need to operate under a wide range of environmental conditions. Blades are certified to perform over a large temperature range: from high altitude freezing conditions to high temperatures and with large variations in moisture content. It is therefore very difficult to design a reliable mechanism in these conditions, especially on small helicopters which do not have a de-icing system. Furthermore, specific environments subject helicopter components to very harsh conditions such as sea and desert environments where corrosion and abrasion are important matters.

1.3.4 Failure

In addition to being designed to exceed the lifetime of the blade, the active blade actuation system must also be developed so as not to influence the performance of the helicopter in the event of a failure. For distributed systems like the active-twist, the performance of the blade profile will not be reduced if the patch actuators are not working. On the contrary, systems such as the Gurney flap, the variable droop leading edge and the trailing edge active blade concept will modify the blade profile during the full rotation of the blade in the event of jamming during deployment. Hence, care must be taken to make sure the helicopter is stable and able to be controlled with a modified profile. Furthermore, in the event of a power failure, the mechanism must go back to its initial state. This can be done by prestressing the mechanism, for instance, or by making sure that the aerodynamic loads are sufficient to bring the mechanism back to its inactive state. However, solutions lead to even more constraints on an actuation mechanism.

1.3.5 Power requirement

Power needs to be transferred from the helicopter to the blades to operate an actuator in a rotor blade. Electrical, pneumatic and hydraulic power can be provided to a rotating blade by the use of specialised rotor mounts which add to the complexity of the rotor hub [61]. The type and the amount of power that can be drawn for an actuation system is a serious limitation to some active systems. Large helicopter blades include a de-icing system for high altitude flight. They provide a good estimation of the electrical loads available in a rotor blade. A typical de-icing system draws up to 1 kW of electrical power that is transferred to each blade. This gives a guide for the allowable power consumption of such active systems.

1.4 Research objectives

The scope of this thesis is to investigate the feasibility of piezoelectric actuators for active mechanical systems integrated into rotor blades. In order to achieve this goal it is essential to develop:

- a generic process to differentiate and select piezoelectric actuation technologies
- a multi-domain approach for designing and optimising a smart actuation system
- procedures to validate and test smart actuation systems

The comparison of technologies for smart helicopter blades within the GRC project reveals that the Gurney flap and the camber change are providing the most improvements as shown in Table 1.2. The additional maturity of the Gurney flap solution makes it one of the most suitable solutions to produce a successful smart blade design.

Table 1.2: Smart helicopter blades technologies.

Category	Technology	Lift control	Stall control	Vibration control
Flap	Trailing edge flap	-	-	+
	Gurney flap	+	+	+
Morphing	VDLE	-	+	+
	Camber change	+	+	+
	Active-twist	-	-	+
	Extended trailing edge	+	-	-
Flow control	Synthetic jets	+	+	-

The focus is on designing and manufacturing a demonstrator of a Gurney flap deployment system for a model helicopter blade. However, the methods and the processes developed can be applied to any type of piezoelectric actuation mechanism that needs to be optimised for a highly constrained environment such as a helicopter blade.

1.5 Conclusion

Today's helicopters are the result of collaborative work in mechanical engineering and aeronautics. The first successes came from inventors who could understand the complexity of a rotating lifting surface while designing advanced mechanical

mechanisms. To further improve today's helicopters, research is focussing on active blade systems to adapt the aerodynamic properties of the blade to the local aerodynamic conditions. Two aspects are especially studied: enhancing the lift on the retreating side and alleviating the large vibrations in the rotor. Both these aspects will provide improvements on helicopter performance. Besides the efficiency of the rotor system, the objective is to push the flight envelope of these aircraft and to make them faster, smoother and quieter.

Many active concepts are being studied, but they all face a large number of challenges to be successfully integrated within a helicopter blade. The rotation speed generates critical loads on the blade and any system within it. Because helicopter blades are the components which provide both lift and control in a helicopter, any mechanism influencing their behaviour must be durable, reliable and safe. Actuation of the active system is the most critical component of a smart adaptive blade. Among actuation technologies, piezoelectric actuators have the potential to provide compelling actuation for these systems. They are actively tested for many of these concepts. Their toughness, size and reliability make them suitable candidates for delivering the required mechanical power.

Selecting an actuation technology alone is, however, not sufficient for an integrated system. The investigation of the loads on the system is paramount to designing a system that conditions mechanical work generated by the actuator into useful motion for a smart system. The key aspect of helicopter progress remains in the collaboration between partners from various domains, combining different skills and expertise to answer these challenges and develop tomorrow's aircraft. In order to move from research and laboratory experiments to flying prototypes and commercial products, the Clean Sky Joint Technology Initiative (JTI) coordinates six Integrated Technology Demonstrators (ITD) to bring various research partners together as shown in Figure 1.11. Among them, the Green Rotorcraft ITD manages the evaluation of the Gurney flap technology to improve helicopter performance and noise reduction with both academic and industrial partners [62].

1.6 Thesis outline

This first chapter presents the history and the difficulties of early rotorcraft. Care has been taken to describe various smart blade technologies and their effects on the performance of helicopters while accounting for the various challenges that arise for their integration into helicopter blades.

Chapter 2 introduces the principles of piezoelectricity and the various types of piezoelectric actuators. The performance of different technologies is compared. A selection of potential actuation systems for smart blades is made according to their performance and the multiple constraints found in a helicopter blade. This chapter

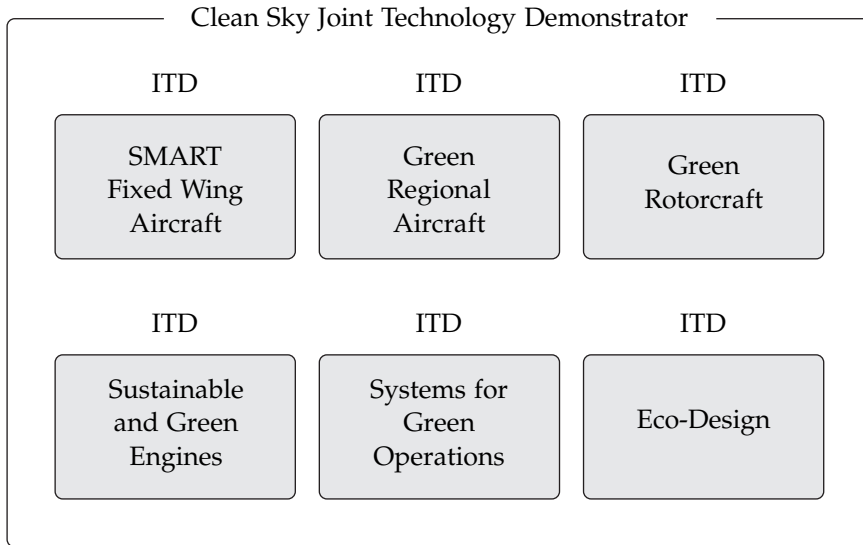


Figure 1.11: Integrated Technology Demonstrators part of Clean Sky JTI.

serves the first research objective by studying the important criteria to establish a selection process for piezoelectric actuators.

Chapter 3 focuses on the performance investigation of available patch piezoelectric actuators. A quasi-static model is presented to evaluate the electro-mechanical coupling of the material according to the deformation recorded on an experimental setup. It is crucial to know in detail the capabilities of actuators to assign them to a suitable application.

Chapter 4 investigates the aerodynamic forces on the Gurney flap. A computational fluid dynamics model is utilised and compared to aerodynamic tables. A Mach-scaling of a full scale blade is considered for the evaluation of the Gurney flap. Such a study is required to design and optimise an actuation mechanism.

Chapter 5 presents the design process for a flexible actuation system for the Gurney flap deployment. It consists of exploring generated designs with an optimisation loop. The mechanical strain developed by the piezoelectric actuator is converted into a relevant displacement and force. Chapter 5 provides the approach to design and optimise, addressing the second research objective.

Chapter 6 extends the optimised design resulting from Chapter 5. The connection between the blade and the Gurney flap is further detailed and relevant

materials are selected. The flap model is refined and choices are made to achieve a suitable motion for rotating the Gurney flap. A transient analysis shows the capabilities of the system without external constraints.

Chapter 7 studies the influence of the dynamics of the model helicopter blade on the motion of the actuation system. A multi-body dynamic model is used to retrieve the motion of the blade while operating at full rotation speed. The corresponding acceleration field on the mechanism is taken into account with the aerodynamic forces calculated in Chapter 4 to show the relevance of such a system for actuation in a model rotor blade. This chapter is part of a validation strategy.

Chapter 8 reports the manufacturing of an actuation system prototype based on the geometries detailed in Chapters 5 and 6. The experimentation shows a behaviour in line with the proposed numerical models. Chapter 8 concludes with recommendations for further testing such a component.

Chapter 9 concludes on the research performed in this thesis and on the actuation system developed for the model blade. Recommendations are given for pursuing the investigation of the z-shaped mechanism.

Performance of piezoelectric actuation systems

2.1 Introduction to piezoelectricity

Piezoelectric materials have the property of converting mechanical energy into electrical energy and conversely of converting mechanical energy into electrical energy. In 1880, Pierre and Jacques Curie discovered the ability of certain crystals to produce an electrical charge of which the magnitude depends on the amount of deformation applied to the material [63]. This effect is called the direct piezoelectric effect. Additionally, when subjected to an electric field, piezoelectric materials deform according to the magnitude of the electric field applied. This effect is the converse piezoelectric effect.

2.1.1 Piezoelectric characteristics

A piezoelectric material is characterised by its piezoelectric strain constant d_{ij} which relates the strain to the electric field. The subscript i indicates the direction of the electric field and the subscript j indicates the direction of the deformation. Prior to being used, a piezoelectric material is poled. Conventionally, the poling direction is along the vertical axis (3-axis) as shown in Figure 2.1. The poling process depends on the piezoelectric material considered and will be further discussed in 2.1.3.

When an electric field is applied in the same direction as the poling direction, the material extends along that direction and contracts along perpendicular directions (1- and 2-axis). Inverting the electric field results in a contraction of the material along the 3-axis with an elongation along 1- and 2-axis. With most piezoelectric materials, the deformation along 1- and 2-axis has the same magnitude, meaning

that the d_{31} and d_{32} coefficients are equal. Therefore, the in-plane deformation is referred to as the d_{31} effect while the deformation in the 3-axis is called the d_{33} effect, as shown in Figure 2.1.

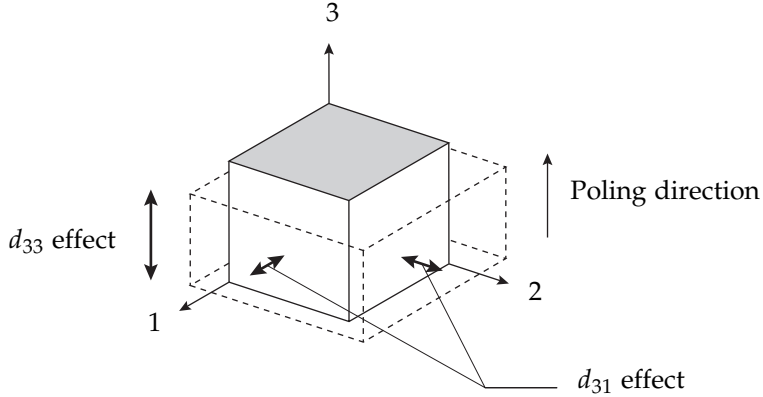


Figure 2.1: Piezoelectric material main deformation modes.

2.1.2 Analytical formulation

The d_{ij} coefficients describe the deformation of the material depending on the orientation of the electric field. The $[d]$ matrix relates to the piezoelectric coefficients in the piezoelectric constitutive equations.

$$\{S\} = [s^{E_v}] \cdot \{T\} + [d]^T \cdot \{E_v\} \quad (2.1)$$

$$\{D\} = [d] \cdot \{T\} + [\epsilon^T] \cdot \{E_v\} \quad (2.2)$$

where $\{S\}$ is the strain vector, $[s^{E_v}]$ is the compliance matrix under constant electric field, $\{T\}$ is the stress vector, $[d]$ is the piezoelectric matrix, $[\epsilon^T]$ is the permittivity matrix under constant stress, $\{D\}$ is the dielectric displacement vector and $\{E_v\}$ is the electric field vector. For most piezoelectric materials, the $[d]$ matrix is defined by only five strain-charge coefficients.

$$[d]^T = \begin{bmatrix} 0 & 0 & d_{31} \\ 0 & 0 & d_{32} \\ 0 & 0 & d_{33} \\ 0 & d_{24} & 0 \\ d_{15} & 0 & 0 \\ 0 & 0 & 0 \end{bmatrix} \quad (2.3)$$

The constitutive equations show the coupling between the mechanical domain and the electrical domain. Equation (2.1) is applied when a piezoelectric material

is used as an actuator while equation (2.2) serves for the formulation of the piezoelectric material as a sensor. The actuator equation relates the mechanical strain in the material to the applied voltage. When no external stress is applied on the piezoelectric component, equation (2.1) becomes:

$$\{S\} = [d]^T \cdot \{E_v\} \quad (2.4)$$

Expanding equation 2.4 gives:

$$\begin{Bmatrix} \varepsilon_1 \\ \varepsilon_2 \\ \varepsilon_3 \\ \gamma_{23} \\ \gamma_{31} \\ \gamma_{12} \end{Bmatrix} = \begin{bmatrix} 0 & 0 & d_{31} \\ 0 & 0 & d_{32} \\ 0 & 0 & d_{33} \\ 0 & d_{24} & 0 \\ d_{15} & 0 & 0 \\ 0 & 0 & 0 \end{bmatrix} \cdot \begin{Bmatrix} E_{v1} \\ E_{v2} \\ E_{v3} \end{Bmatrix} \quad (2.5)$$

where E_{vi} are the components of the electric field, ε_i the normal strain components and γ_{ij} the shear components. In the case of a piezoelectric sensor, when no electric field is applied to the piezoelectric material equation 2.2 becomes:

$$\{D\} = [d] \cdot \{T\} \quad (2.6)$$

Expanding equation 2.6 gives:

$$\begin{Bmatrix} D_1 \\ D_2 \\ D_3 \end{Bmatrix} = \begin{bmatrix} 0 & 0 & 0 & 0 & d_{15} & 0 \\ 0 & 0 & 0 & d_{24} & 0 & 0 \\ d_{31} & d_{32} & d_{33} & 0 & 0 & 0 \end{bmatrix} \cdot \begin{Bmatrix} E_{v1} \\ E_{v2} \\ E_{v3} \end{Bmatrix} \quad (2.7)$$

where D_i are the components of the dielectric displacements. The effectiveness of a piezoelectric material as a sensor or as an actuator is directly related to the piezoelectric coefficients. The value of the piezoelectric coefficients depends significantly on the material considered.

2.1.3 Piezoelectric materials

Besides the crystals and salts first studied by the Curie brothers, materials such as polymers and ceramics can exhibit piezoelectric properties as well. Piezoceramics are nowadays the most widely used piezoelectric material.

Piezoceramics

Piezoceramic materials were extensively developed at the end of the Second World War for use in ultrasonic transducers for sonar applications [64, 65]. Today, piezoceramics are used in numerous applications including alarm buzzers, microphones, fuel injectors and ignition plugs. Lead zirconate titanate (PZT) ceramics constitute the most common piezoceramic material available. This

material possesses a perovskite structure which shows some degrees of symmetry. Consequently, the $[d]$ matrix can be simplified as only three piezoelectric coefficients are required to describe the piezoelectric effect ($d_{32} = d_{31}$ and $d_{24} = d_{15}$).

$$[d_{\text{PZT}}]^T = \begin{bmatrix} 0 & 0 & d_{31} \\ 0 & 0 & d_{31} \\ 0 & 0 & d_{33} \\ 0 & d_{15} & 0 \\ d_{15} & 0 & 0 \\ 0 & 0 & 0 \end{bmatrix} \quad (2.8)$$

These ceramics consist of many polycrystalline cells, each with a distinct polarisation direction. The material does not show any global polarisation because of the random distribution of the polarisation direction for each crystalline cell. Above the Curie temperature (T_c), the lattice of the unit cell of the material is cubic, symmetric and does not possess a dielectric moment as shown in Figure 2.2. When the temperature falls below the Curie temperature the unit cell deforms in a tetragonal lattice. This breaks the symmetry and creates a dipole responsible for the polarisation of the unit cell and the crystalline cell [66, 67].

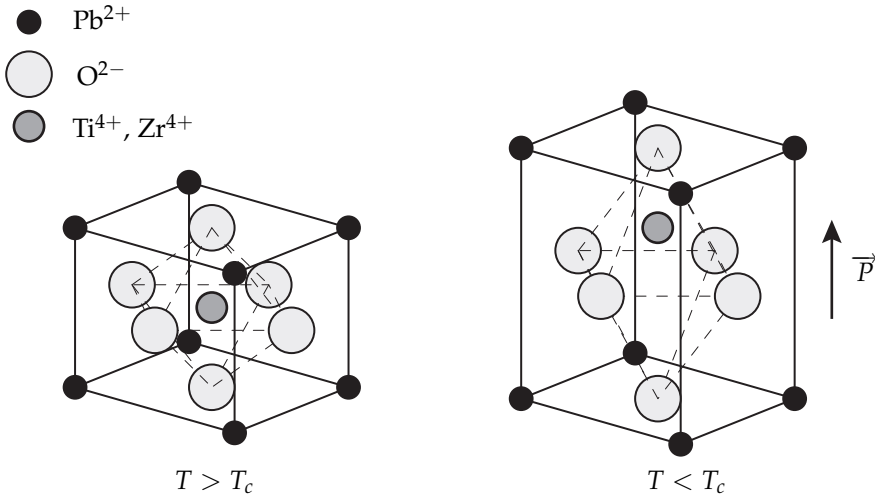


Figure 2.2: Crystal lattice of the PZT unit cell below and above the Curie temperature. The material possesses a dielectric moment (\vec{P}) when the temperature is below the Curie temperature (T_c).

In order to gain piezoelectric properties, the contribution of each polycrystalline cell needs to add up to show a global polarisation. Piezoceramics are heated above their Curie temperature and cooled down while a large electric field is

applied. The electric field orients the unit cell deformation which polarises the material in the electric field direction. Once the temperature falls below the Curie temperature, the deformations of the crystalline cells are locked and thus the polarisation. This step constitutes the poling process for piezoceramics. The polarisation is removed if the ceramic is heated above its Curie temperature. As shown in table 2.1 many references of piezoelectric ceramic materials are available. Their large piezoelectric coefficients make them a component of choice for actuation applications.

Table 2.1: Properties of commercial piezoceramics. PZT-SP4 and PZT-5A1 are from Smart Material Company [68]. PZT-5H is taken from [15]. PZT-PSt-HD and PZT-PSt-HPSt are from Piezomechanik Company [69]. Finally, PZT-PIC-255 and PZT-PIC -151 are from Physic Instrumente Company [70].

Name	d_{31} (m/V)	d_{33} (m/V)	e_{33}	T_c (°C)	ρ (kg/m ³)	S_{33} (m ² /N)
PZT-SP4	-1.23e-10	3.1e-10	1300	325	7500	1.81e-11
PZT-5A1	-1.85e-10	4.4e-10	1850	335	7500	2.07e-11
PZT-5H	-2.74e-10	5.93e-10	3400	193	7500	2.083e-11
PZT-PSt-HD	-1.9e-10	4.5e-10	1900	345	7500	2.1e-11
PZT-PSt-HPSt	-2.9e-10	6.4e-10	5400	155	8000	1.8e-11
PZT-PIC-255	-1.8e-10	4.0e-10	1750	350	7800	2.07e-11
PZT-PIC-151	-2.1e-10	5.0e-10	2400	250	7800	1.9e-11

Piezopolymers

PolyVinylidene Fluoride (PVDF) is the main organic material that exhibits a significant piezoelectric effect as shown in Figure 2.3 [71]. Like any piezoceramic material, the constants d_{33} , d_{32} and d_{31} characterise the electromechanical properties of the material. Unlike piezoceramics, piezopolymers do not possess shear electromechanical coupling ($d_{15} = d_{24} = 0$) and have distinct d_{31} and d_{32} as shown in Table 2.2. The poling process for the polymer consists of a combination of tensile constraints and large electric fields at elevated temperatures. Stretching the polymer aligns the carbon chains and arranges the existing dipoles in a direction normal to the applied stress. The polymer is then subjected to heat and a large electric field to complete the polarisation process [71, 72].

At room temperature the amorphous part of the PVDF polymer is above its glass transition temperature (around -35°C) [73]. The polymer is therefore flexible at room temperature and can easily be manufactured into films for sensing applications. This large flexibility of the polymer film ensures that the sensor is not affecting the mechanical behaviour of the component it is bonded to. PVDF also has a failure strain larger than resistive strain gages [71], providing an interesting alternative for the measurement of large deformations. Unfortunately, the overall

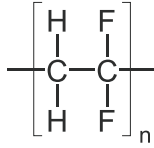


Figure 2.3: Poly(vinylene fluoride) structure.

performance of the polymer is far behind typical piezoceramic materials as shown in Table 2.2. The force and the displacement generated are lower for the same applied voltage, making piezoelectric polymers not a realistic option for actuators.

Table 2.2: Comparison of the piezoelectric coefficients of PZT-5H piezoceramic and PVDF piezopolymer [15].

Name	d_{31} (m/V)	d_{32} (m/V)	d_{33} (m/V)	d_{15} (m/V)
PZT-5H	-274e-12	-274e-12	593e-12	741e-12
PVDF	20e-12	3e-12	-33e-12	0

2.2 Piezoelectric actuators

Many types of piezoelectric actuators are classified in this section. Their classification depends on the piezoelectric effect used to generate motion. The material considered is PZT piezoceramics which constitutes the best materials for actuation applications. The performance of a piezoelectric actuator is typically measured in the displacement without constraints (*free displacement*) and in the maximum output force when the actuator is clamped in its displacement direction (*block force*) [15, 74, 75].

2.2.1 d_{31} effect actuators

Piezoceramics using the d_{31} effect are using the fact that a through-thickness electric field will contract the material's width and length. To take advantage of this principle, thin sheets of piezoelectric material are manufactured and sandwiched between two sheets of conductive material as shown in Figure 2.4. These laminates are the most simple piezoelectric actuators. They are referred to as patch or laminar piezoelectric actuators. Patch actuators can be easily bonded to or embedded inside a structure.

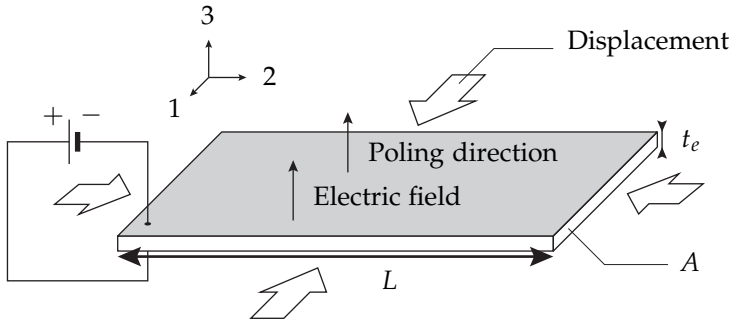


Figure 2.4: In-plane deformation of a piezoelectric patch actuator in a positive electrical field.

The free displacement Δ_{free} of the actuator in the direction of axis 1 is obtained by deriving the reduced actuator equation (2.5) and using the relation between the electrical field and the voltage:

$$\Delta_{\text{free}} = -d_{31} \cdot L \cdot \frac{V}{t_e} \quad (2.9)$$

where L is the length of the patch actuator, V the applied voltage and t_e the thickness of the piezoelectric sheet. The block force F_{bl} in the direction of axis 1 is obtained from the constitutive equation (2.1):

$$F_{\text{bl}} = -\frac{d_{31} \cdot V \cdot A}{s_{11}^E \cdot t_e} \quad (2.10)$$

where A is the cross-sectional area of the patch along axis 1, and s_{11}^E is the 1,1 component of the compliance matrix s^E . Equations 2.10 and 2.9 show that the free displacement of the actuator is related to its length while the block force is related to its width.

2.2.2 d_{33} effect actuators

The d_{33} effect corresponds to the deformation along the direction of the polarisation direction. In piezoceramics, the d_{33} coefficient is always larger than the d_{31} coefficient. Consequently, there are many types of actuators that try to take advantage of the larger d_{33} coefficient using various geometries.

Stack actuators

Stack actuators consist of multiple layers of piezoceramic material separated by electrodes as shown in Figure 2.5. This configuration allows large elements to be

made while keeping the operating voltage small. The direct relation between the height of the component and the free displacement (equation 2.11) provides a means to easily tune the material to a displacement requirement for an application.

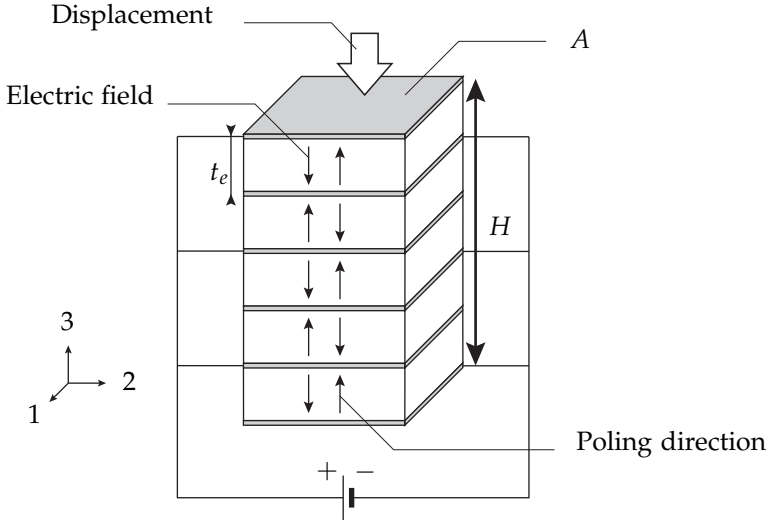


Figure 2.5: Contraction of a piezoelectric stack actuator, in a negative electrical field.

The free displacement and the block force of a stack actuator are obtained from the constitutive equation (2.1). The derivation is performed along axis 3 in a similar way as for the piezoelectric patch actuator (equations (2.9) and (2.10)), leading to:

$$\Delta_{\text{free}} = -d_{33} \cdot H \cdot \frac{V}{t_e} \quad (2.11)$$

$$F_{\text{bl}} = -\frac{d_{33} \cdot V \cdot A}{s_{33}^E \cdot t_e} \quad (2.12)$$

where H is the height of the component, A its cross section perpendicular to axis 3 and t_e the layer thickness. As shown in equations (2.11) and (2.12), the performance of the actuator is related to the distance between two layers. This defines the input of the electric field from the applied voltage. As the maximum electric field depends on the material, the thickness of the layers defines the voltage required for the actuator. Typically, a thickness of $250 \mu\text{m}$ translates into an applied voltage of 1000 V , thus thin layers are a requirement for low-voltage applications.

AFC-MFC actuators

Thick piezoceramic components have better displacement capabilities but are not as convenient as patch actuators for integration. Active Fibre Composites (AFC) and Macro Fibre Composites (MFC) consist of piezoceramic fibres embedded inside a protective polymer substrate as shown in Figure 2.6. The poling direction follows the fibre direction to benefit from the large d_{33} coefficient while such a geometry provides the flexibility of a patch actuator. The electric field is applied through the fibres through interdigitated electrodes bonded on the top and the bottom of the component. AFCs have fibres with a circular cross section while MFC fibres possess a square cross section which improves contact with the electrodes.

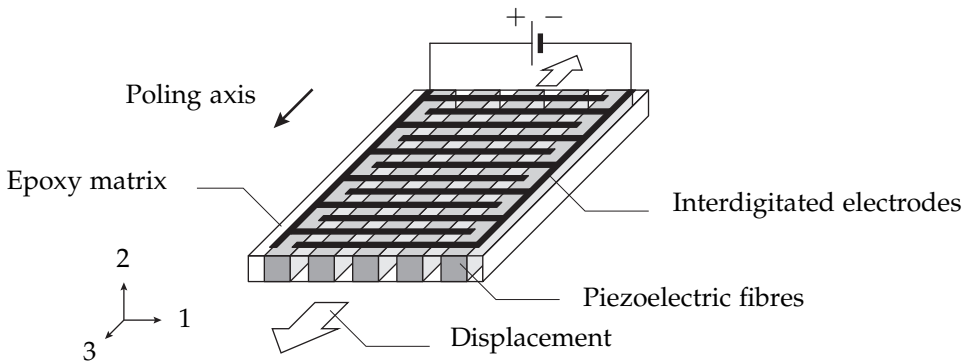


Figure 2.6: Sketch of a Macro Fibre Composite actuator.

The block force and free displacement of MFC and AFC is complex to calculate because the substrate plays an important role in the material mechanical behaviour. Furthermore, the electric fields are not homogeneous through the material because of the electrode pattern. Such a system is typically solved using homogenisation techniques that focus on a unit cell of the fibre. First, the electric field path through a fibre is computed along with its deformation for the electric field pattern and deformation. The results are then applied to derive the macroscopic behaviour of the component [74, 76].

d_{33} patch actuator

To provide a more efficient utilisation of the material upon MFCs, Physik Intrumente is developing a new laminar actuator taking advantage of the d_{33} effect in the same way as stack actuators. Such a component is made by cutting a thin slice of a stack actuator and protecting it inside a polymer substrate as shown in Figure 2.7. The resulting component is as efficient as a d_{33} stack actuator. The voltage required for actuation is low while the packaging provides a way to easily bond the component to a structure.

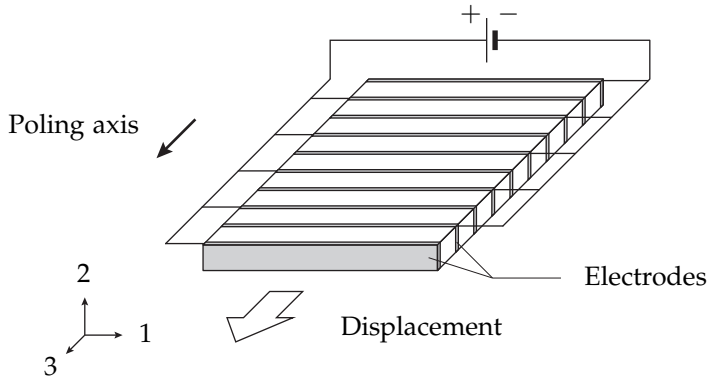


Figure 2.7: Sketch of a d_{33} patch actuator.

2.2.3 d_{15} effect actuators

The d_{15} effect is the shear coupling with an electric field applied along axis 1 or axis 2 as shown in Figure 2.8. This effect can be used to provide very accurate lateral displacements. Research has been conducted on manufacturing a twisting actuator that utilises shear actuators assembled in a circle [77, 78]. Such an actuator can directly provide rotation and torque.

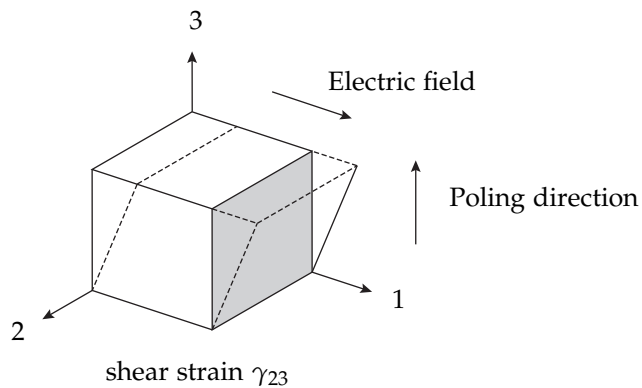


Figure 2.8: Piezoelectric shear deformation mode.

2.3 Performance of piezoelectric actuators

In the previous section, many types of piezoelectric actuators were detailed. They all share characteristics that affect the development of a piezoelectric system for any application. Performance is characterised by a combination of force, displacement and actuation speed.

2.3.1 Piezoelectric actuation characteristics

Asymmetric actuation

Asymmetric actuation is one of the characteristics of piezoceramic based actuators. The material tensile strength is significantly lower than its compressive strength [79, 80]. As a result, the actuation needs to be asymmetric to use the material to its full capabilities. A solution consists of pre-stressing the component in compression to have a symmetric actuation profile. For patch actuators, carefully chosen layers can compress the material during a heating cycle using different coefficients of thermal expansion [81]. In the case of piezoelectric stack actuators, the piezoelectric layers are placed inside a casing with a compressive spring.

Hysteresis

During an actuation cycle, the displacement recorded when loading the actuator does not coincide with the displacement recorded during unloading. This hysteresis effect is due to relaxation phenomena happening during the deformation of the crystalline lattice [82]. In practice, this effect is balanced with a controller which adapts the voltage applied to the piezoelectric actuator as a function of the effective displacement [83, 84].

Heat

The heat generated by a piezoelectric actuator during operation is due to a combination of electrical and mechanical effects: mechanical damping, dielectric loss and hysteresis. The increase in temperature depends on the quality of the piezoelectric actuator and the frequency at which it is actuated [85, 86]. The temperature increase is not likely to cause a depolarisation of the piezoelectric material. Nevertheless, it affects the electromechanical properties of the material [87]. In order to maintain an accurate displacement, a close-loop control is implemented that takes care of both the hysteresis and temperature effect during actuation [70].

Displacement and force

The displacement in a piezoelectric material comes from small geometrical changes in the crystalline lattice of the material. The deformations are small and

the maximum strains achieved by piezoceramic actuators are around 0.1%. Therefore, even with high stack actuators or long patch actuators, the overall displacements observed are small. For instance, a 1 m long actuator is capable of displacements in the mm range. Nevertheless, the deformations are very accurate, which explains the interest in piezoelectric actuators for nano-positioning applications. Contrary to their displacement performance, piezoelectric actuators exhibit large forces. The force depends on the cross section of the material in the direction of the displacement. A typical actuator with a cross-sectional area of 1 cm^2 can deliver forces of a few kN [69, 70].

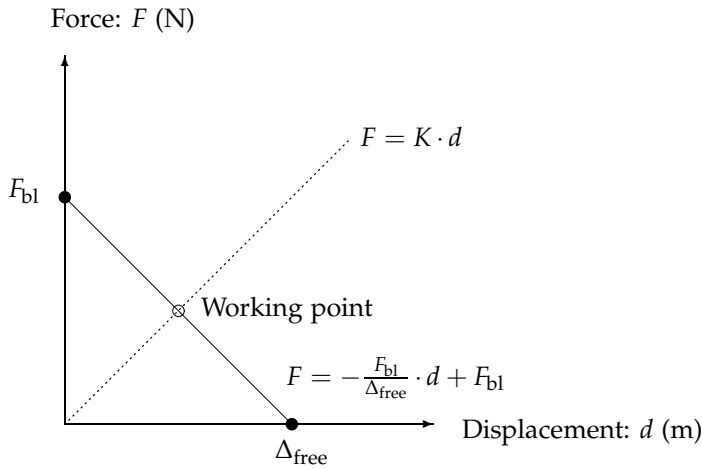


Figure 2.9: Characteristic curve of a piezoelectric actuator and its working point. K refers to the structure stiffness in the direction of the motion.

Figure 2.9 represents the linear relation between the block force and the free displacement for a given applied voltage. This plot is the characteristic curve of a piezoelectric actuator. The working point of a piezoelectric actuator is defined by the intersection of the characteristic curve with the line corresponding to the stiffness of a component set in motion by the actuator as shown in Figure 2.9.

When suiting a piezoelectric actuator to an application, care must be taken to derive the actuator operational range using the characteristic curve. The actual displacement of the actuator will be lower than its free displacement because of the stiffness of the components connected to the actuator. This is also true for the force which is reduced compared to the block force.

2.3.2 Amplification

Mechanical amplification systems can be added to a piezoelectric actuator to enhance its displacement capabilities. Such a system acts as a lever by increasing the displacement at a force cost. Cedrat Technologies has developed actuator systems, that include a stack actuator within an elliptical shell, that triple the piezoelectric displacement as shown in Figure 2.10 [88, 89, 90]. Although the applications remain the same as piezoelectric actuators, these systems provide more flexibility for piezoelectric based solutions.

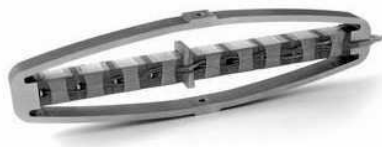


Figure 2.10: Picture of an amplified piezoelectric actuator from Cedrat Technologies. This actuator is 125 mm long and has been studied for trailing edge flap applications.

2.3.3 Linear piezoelectric actuators

Linear piezoelectric actuators utilise multiple piezoelectric components that apply motion to a linear system to compensate for the disadvantages of plain piezoelectric actuators. The main characteristics of such actuators are large displacements, a block force while no voltage is driving the component and a symmetric output force. They all use contact and friction to transmit motion to a moving shaft. Figure 2.11 shows the working principle of a stick-slip linear piezoelectric actuator.

Inchworm actuators

The most basic piezoelectric linear actuator consists of piezoelectric elements to clamp the moving shaft while others provide a forward motion. The clamping is operated in sequence with the elements responsible for the actual motion as shown in Figure 2.12. The result is a stepping motion that is very precise while keeping the moving part in place when not in operation. Moreover, these actuators are capable of providing significant forces over a large distance compared to a conventional piezoelectric actuator. Such an actuator is widely used for nano-positioning [91]. Modern versions of the inchworm actuator include shearing elements to achieve a smoother and more effective motion [70, 92].

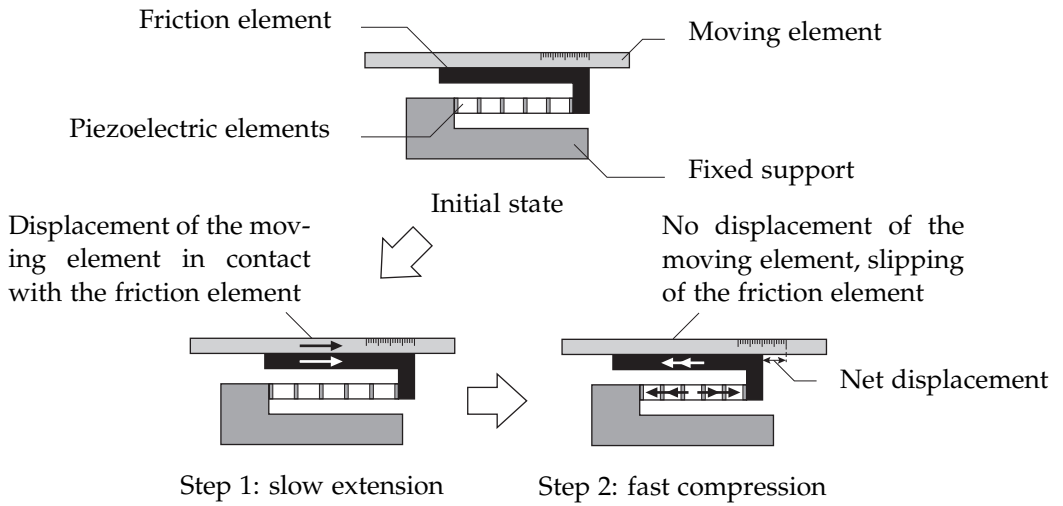


Figure 2.11: Sketch of the working principle of a stick-slip linear piezoelectric actuator.

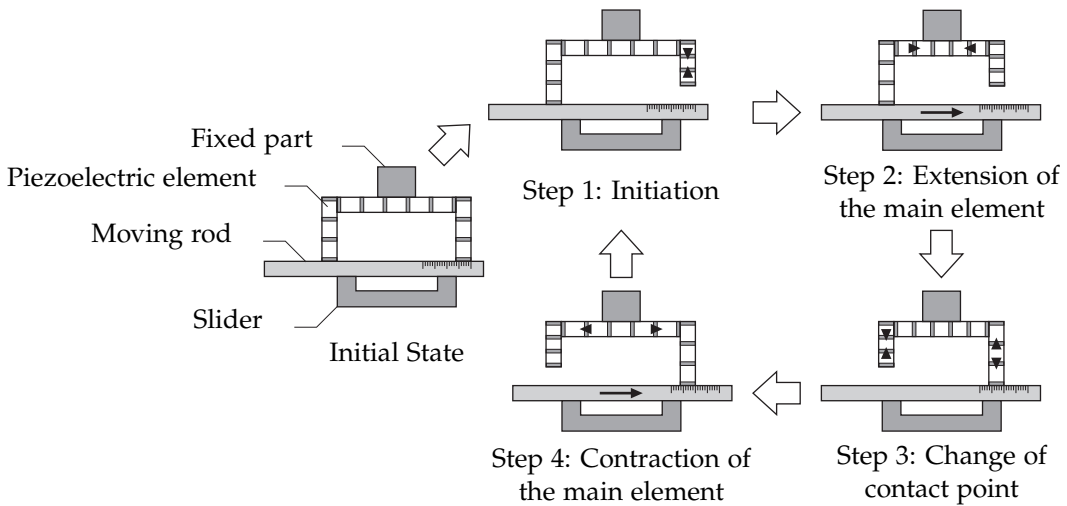


Figure 2.12: Sketch of the working principle of an inchworm or stepped linear piezoelectric actuator. The two vertical piezoelectric elements act like clutches that alternately make contact with the rod.

Ultrasonic actuators

Ultrasonic actuators use deformation waves to transfer motion to a mobile shaft through friction coupling. Standing wave actuators can be distinguished from

travelling wave actuators. In a standing wave actuator, two orthogonal vibration modes are excited to create a standing wave (axial and bending vibration modes for instance) [54]. Depending on the modes excited, the surface of the piezoelectric part is in contact with the shaft at precise locations as shown in Figure 2.13.a. In a travelling wave actuator, multiple modes are excited at the same time to create a travelling wave by modal superposition [54, 93]. Here all the surface points get in contact with the piezoelectric element, increasing the force and efficiency of the actuator as shown in Figure 2.13.b. Furthermore, the wear of the component is averaged over the whole contact surface. These actuators are very common in applications where the space constraints and speed are critical: circular ultrasonic actuators serve as rotational actuators in the auto focus system of many camera lenses [94].

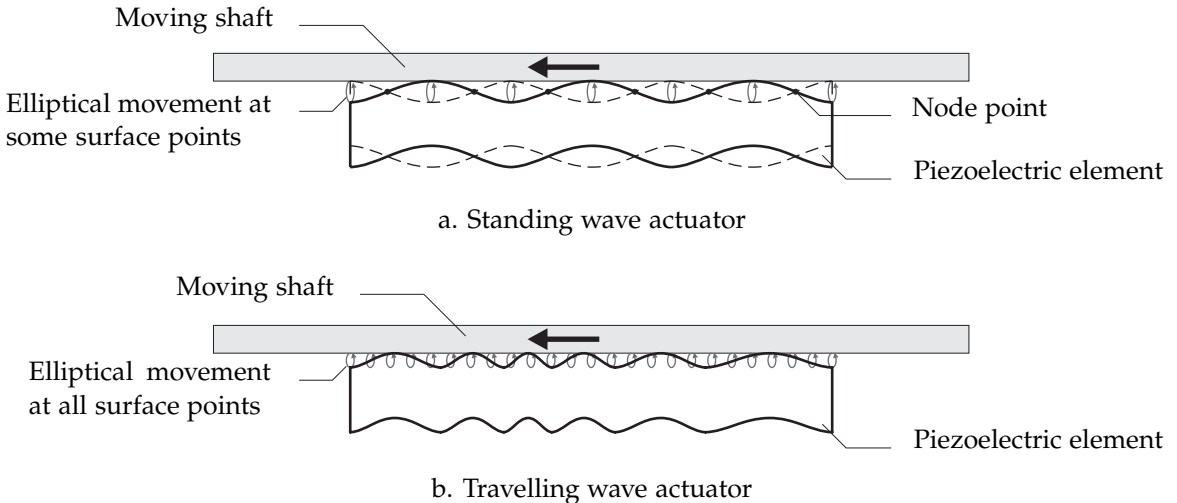


Figure 2.13: Difference between a standing wave actuator and a travelling wave actuator.

Lead-screw actuator

The lead-screw actuator consists of a cylindrical component in which bending vibration modes are excited through a piezoelectric actuator. The orbital motion produced forces a threaded shaft to exhibit a rotational and linear motion. This principle is used by New Scale Technology to make a compact actuator for micro applications as shown in Figure 2.14 [55]. The threaded shaft can be used to deliver both translation and rotational displacement.

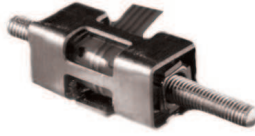


Figure 2.14: Picture of a Squiggle actuator from New Scale Technologies. The actuator is only 6 mm long which makes it the smallest linear drive.

2.3.4 Bandwidth

The performance of piezoelectric actuators is usually associated with their ability to reach a large range of frequencies. They are often chosen for applications that require large accelerations and velocities and small actuation time. The first widespread use of piezoelectric actuators was for manufacturing acoustic sources for sonar because of their large actuation frequency bandwidth. Cedrat Technologies manufactures actuators with a response time below 1 ms [88, 90, 95]. Moreover, the typical resonance frequency for piezoelectric actuators is in the kHz range, leaving a very comforting margin for structural applications [96].

2.3.5 Power consumption and voltage

The power consumption of piezoelectric actuators depends on the type of actuation. Integrated inside an electrical circuit, a piezoelectric actuator behaves like a capacitor. Under harmonic actuation, the energy required to charge the piezoelectric actuator can be recuperated in the system for the next charge. When fast positioning is required, the electrical components which drive the piezoelectric actuator must be able to provide large currents. For the discharge, the circuit and its components must be able to dissipate quickly the energy stored in the piezoelectric. Therefore, active systems using harmonic actuation only need around 100 W in operation, while a fast actuation system requires close to 1000 W of power depending on the actuation profile. Therefore, the main problem is not the amount of electrical power required but the time during which the power is required.

The difference of power consumption between two piezoelectric actuators is a function of the voltage level and the capacitance of the actuator. The average power consumed by a piezoelectric actuator of capacitance C under a harmonic voltage is:

$$P_{\text{avg}} = 2 f C U_{\text{pp}}^2 \quad (2.13)$$

where U_{pp} is the peak-to-peak voltage and f the frequency of the input voltage signal. If two piezoelectric actuators made of the same material are compared, their difference in geometry results in a difference in capacitance and thus in the power required for the same amount of deformation.

2.3.6 Reliability and operational environment

Piezoelectric actuators are very reliable and can perform a large number of cycles under good operating conditions. For instance, piezoelectric stack actuators manufactured by Physik Instrumente feature 10^9 cycles [70]. Cedrat technologies is developing high end actuators with 10^{10} cycles before failure [88]. Furthermore, piezoelectric actuators can operate in very harsh environments. Physik Instrumente provides piezoelectric stack actuators capable of operating in cryogenic environments [70]. Moreover, piezoelectric actuators can operate at high temperatures as long as the Curie temperature is not reached. The Curie temperature is the temperature at which the piezoelectric material loses its electro-mechanical coupling and this temperature is usually higher than $200\text{ }^\circ\text{C}$ as shown in Table 2.1.

2.4 Selection of an actuator technology

In order to appropriately select an actuator technology for an application, a classification needs to be made with figures relevant for all types of actuators. This section defines a set of figures to compare piezoelectric-based actuators.

2.4.1 Mechanical work per weight

Actuators categorised as piezoelectric-based include a variety of technologies. The performance of these technologies is difficult to compare due to their means of utilising the piezoelectric effect to produce displacement and force. Figure 2.15 shows the spread of displacements and forces for various technologies discussed in this chapter.

The specific mechanical work is calculated to account for actuators as different as stack actuators and ultrasonic actuators. It gives the amount of mechanical energy developed divided by the weight of the actuator, weight being a major bottleneck for smart-blade systems. This figure provides an indication of the efficiency of an actuation solution regardless of the stroke or force capability. The mechanical work is easily obtained for linear piezoelectric actuators because they deliver a constant force over their full stroke. For standard piezoelectric actuators, the maximum displacement corresponds to the minimal output force and vice versa. In order to obtain an estimation of the mechanical work for piezoelectric actuators, the characteristic curve is plotted. The working point and the work path taken by a moving mechanism depend on the load case and cannot be determined by the actuator only. A reasonable estimation of the work is done by taking a working point corresponding to half the free displacement and half the block force. The mechanical work W delivered by a piezoelectric actuator is therefore:

$$W = \frac{F_{bl}}{2} \cdot \frac{\Delta_{free}}{2} \quad (2.14)$$

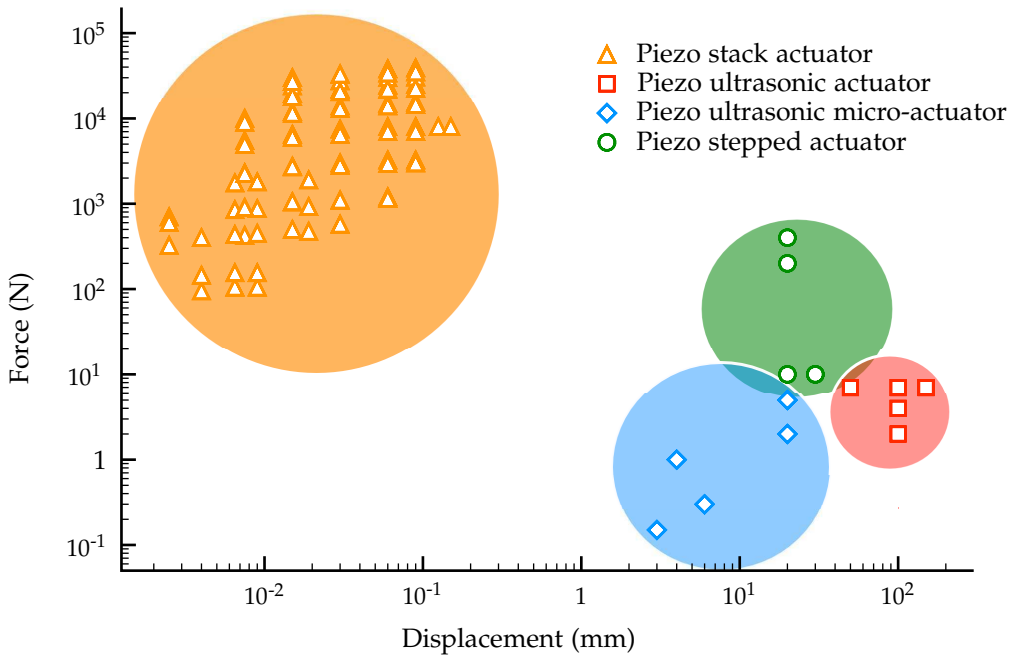


Figure 2.15: Range of free displacements and block forces for various piezoelectric-based actuator technologies.

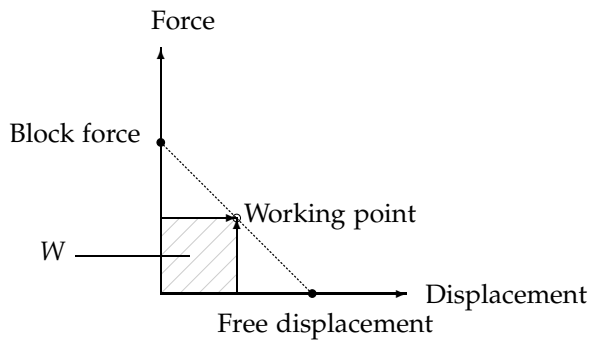


Figure 2.16: Work paths to achieve constant force over a displacement and vice versa.

2.4.2 Time to complete one actuation cycle

The various technologies available present large differences in time to achieve their full stroke and to therefore develop their maximum work. Time is critical for high frequency applications such as vibration damping or helicopter control surfaces. The developed work, plotted versus the time to achieve one cycle, appears a relevant parameter as shown in Figure 2.17. Moreover, it is possible to define the mechanical work developed by an actuator in the case of an incomplete cycle, allowing the comparison over the full actuation range of a system.

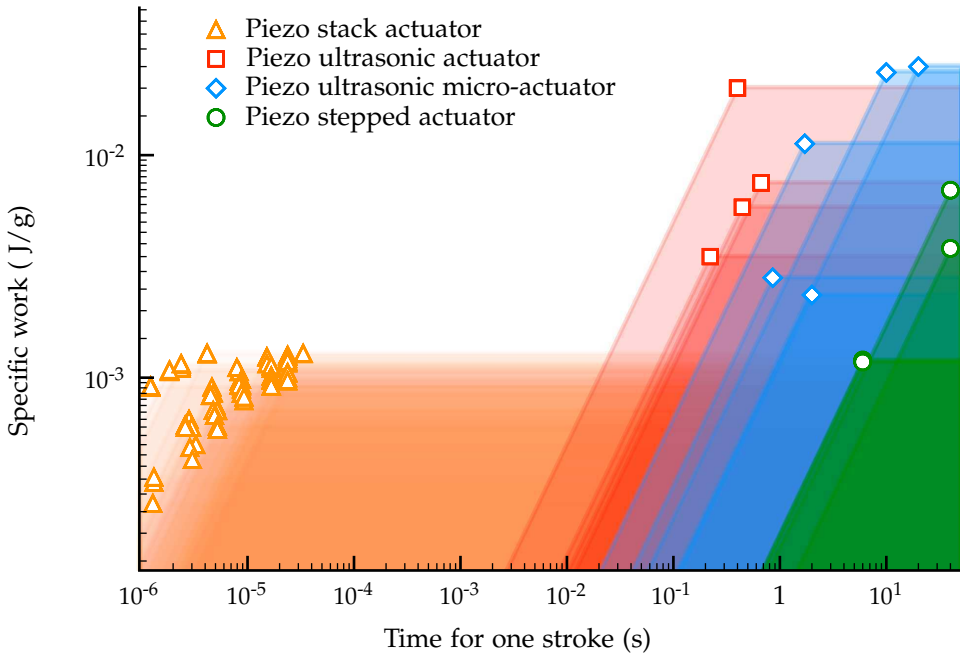


Figure 2.17: Graph of the specific work of an actuator versus the time to achieve a full stroke. The lines shows the decrease in mechanical work capability of the actuator as the time to achieve a cycle is reduced.

A slow actuation technology like stepped actuators can deliver large mechanical work. However, such a technology cannot deliver its full stroke within the specified time in the case of high frequency actuation cycles. Therefore, the work available is reduced as shown in Figure 2.17. Faster actuation technologies like piezoelectric stacks have a lower specific work but they are capable of delivering it in much shorter cycles. Therefore, it is important to consider the duration of an actuation cycle when selecting a technology.

2.4.3 Number of actuators required

The number of actuators needed is also an important factor given that many solutions are for micro-systems and are very efficient. However, they do not represent a realistic solution when hundreds of them are necessary for providing enough mechanical work on a larger scale.

2.4.4 Toughness, fatigue and environmental conditions

The components' toughness and their fatigue characteristics need to ensure a service life that is as long as specified by the application. Section 1.3.3 showed a large difference in lifetime depending on the actuation frequency of the application. Finally, the component must be able to operate within the operating conditions specified by the application.

2.4.5 Power consumption and integration

The last selection parameter is the power required to achieve the amount of mechanical work specified by the application. As detailed in section 1.3.5, the power available for a mechanical system is limited in helicopter blades. Moreover, large power requirements involve additional equipment to transmit electricity to the component as well as more complex security requirements.

2.5 Conclusion

In this part, the principles of piezoelectricity were detailed as well as various piezoelectric actuator technologies. Piezoelectric actuators provide, in general, a relevant solution to many of the challenges encountered for the integration of actuation systems in rotor blades. In order to select the most efficient one for an application, a selection process is established, which utilises the parameters discussed in the previous sections as shown in Figure 2.18.

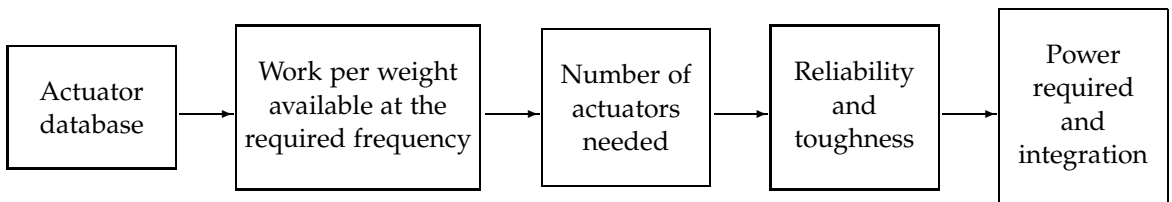


Figure 2.18: Actuator selection diagram.

Prior to applying the selection diagram for the application considered, two actuators of interest are studied in detail in Chapter 3. The loads required to deploy the Gurney flap are investigated in Chapter 4. The selection process will then be applied in Chapter 5 assuming three control strategies for the active Gurney flap.

Performance investigation of d_{33} patch actuators

3.1 Introduction

Among the actuators defined in the previous chapter, the Macro Fibre Composite (MFC) from Smart-Materials and the d_{33} patch actuator from Physik Instrumente are of interest. The MFC was the first patch actuator to take advantage of the superior d_{33} piezoelectric coefficient for actuation. Their differences in design leads to important consequences in operating voltage and efficiency. The objective is to determine which technology is better suited for integration inside a helicopter blade for the deployment of an active Gurney flap.

MFCs consist of piezoelectric fibres embedded inside a piezoelectric matrix. The electrical field is applied by the use of interdigitated electrodes on the top and bottom surface of the actuator as detailed in section 2.2.2. As a consequence, the electrical field is not homogeneous and the electrode distance influences the electrical path [97] as shown in Figure 3.1. On the contrary, Physik Instrumente's novel d_{33} patch actuator employs the same geometry as a stack actuator, but the electrical field goes straight through the material as shown in Figure 3.2. This chapter investigates and compares the performance of these two piezoelectric actuator technologies in terms of generated strain per volt through experimental testing.

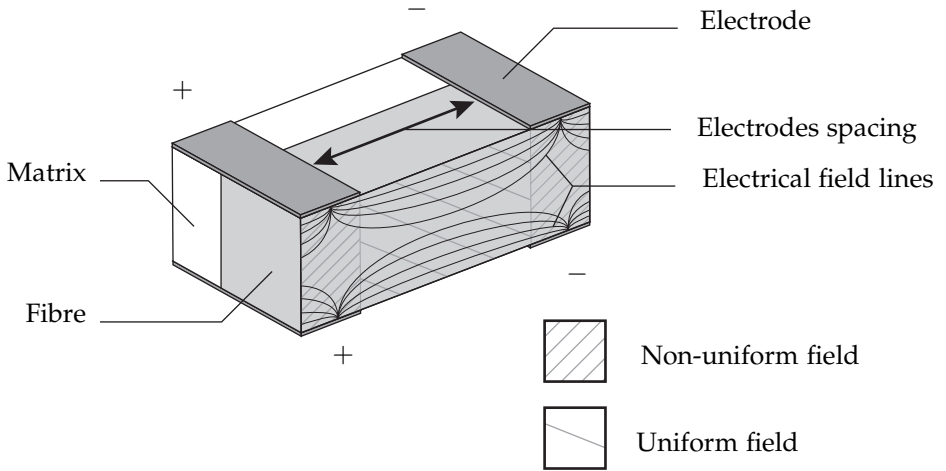


Figure 3.1: Schematic representation of electrical paths taken by the electric field between two electrodes in a MFC [98].

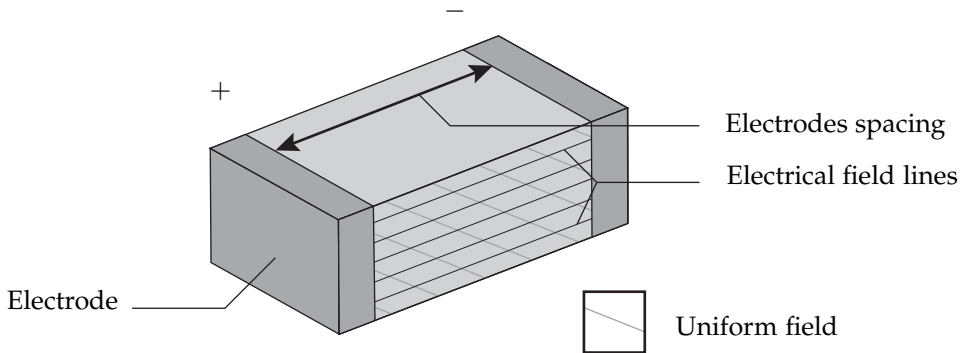


Figure 3.2: Schematic representation of electrical paths taken by the electric field between two electrodes in a d_{33} patch actuator.

3.2 Materials and experimental setup

3.2.1 Specimen manufacturing

In-depth characterisation of patch actuators is realised by bonding the patch actuator on a substrate and monitoring the strain over various levels of voltages [98, 99]. Here, composite beams are chosen as a substrate for both actuators. A composite panel was manufactured from a PEI-AS4 pre-impregnated fabric

produced by Ten Cate Advanced Composites. The product reference is CETEX thermo-Lite [100], its characteristics are listed in Table 3.1. A 250 mm long square panel was produced with a $[0,90]_s$ layup. The quality of the panel of typical thickness 0.603 mm was validated by checking that the deviation of the thickness is not exceeding 1%.

Table 3.1: Specifications of the composite layer used for manufacturing the beam.

Property	Value	Unit
Longitudinal tensile modulus	18.8	GPa
Transverse tensile modulus	1.3	GPa
Thickness per ply	0.16	mm
Poisson's ratio	0.32	–
In-plane shear modulus	3.5	GPa

The actuator samples from Physik Instrumente are made from PICMA piezo-electric stack actuators and are very different in size and maximum operational voltage compared to the MFCs from Smart-Material. The main characteristics of both actuators are listed in Table 3.2. The large difference in operational voltage is a direct consequence of the electrode technology to apply an electrical field inside the material. The electrical field paths put a limit on the minimum distance between electrodes for MFC d_{33} actuators [97]. Therefore the voltage applied to MFCs needs to be much larger than the voltage applied for d_{33} actuators to achieve the same electrical field. This is the main advantage of Physik Instrumente actuators.

Table 3.2: Characteristics of MFC 4010-P1 and PI d_{33} patch actuators.

Properties	MFC 4010-P1	PI d_{33} actuator
Active length (mm)	40	15.5
Active width (mm)	10	4.6
Active thickness (mm)	0.3	0.3
Length (mm)	54	36
Width (mm)	22	8
Maximum voltage (V)	1500	130
Electrode/Layer spacing (μm)	500	55
PZT d_{33} coefficient pC/N	460	400
Capacitance (nF)	1	100
Free strain per volt ($\mu\text{strain}/\text{V}$)	0.93	7.27

The composite panel is cut into strips where the width is similar to the full width of each actuator type. The actuators are then bonded onto the corresponding composite strips using a 3M structural epoxy glue. Consolidation is performed under vacuum for 12 hours. Three specimens are made with the d_{33} actuator and one sample is made using a MFC actuator.

3.2.2 Experimental setup

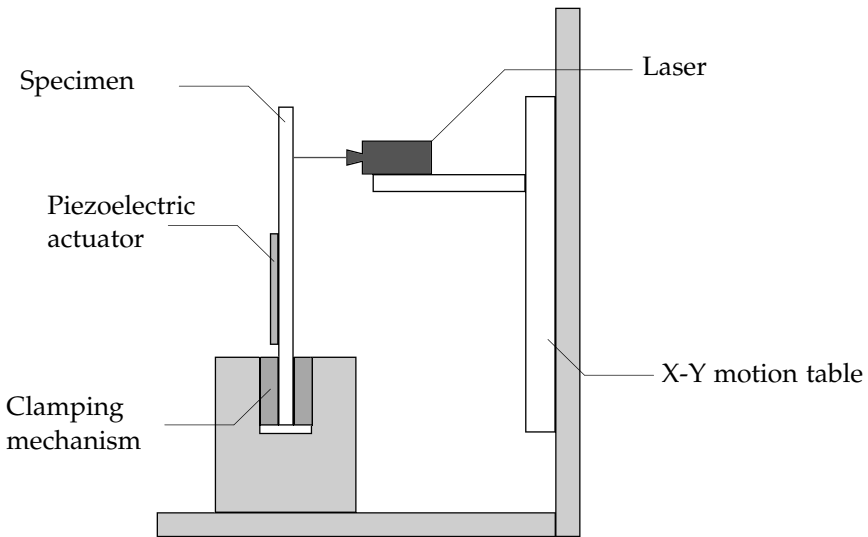


Figure 3.3: Sketch of the experimental setup to evaluate the displacement of the specimen manufactured.

The composite strips are clamped vertically in front of an X-Y motion table onto which a laser distance sensor is mounted as shown in Figure 3.3. The distance between the laser and the back of each specimen is measured at 50 points before and after applying a voltage. A voltage of 1000 V is applied to the actuator from Smart-Material while a voltage of 100 V is applied to the actuator from Physik Instrumente. These voltages have been chosen to provide approximately the same electrical field inside both actuators. Upon applying the voltage, all specimens showed a significant deflection which is captured by the experimental setup. The effect of misalignment of the laser compared to the plane of the specimen is removed by subtracting the measurements taken with and without applying a voltage, respectively. The data for the experiment need to be compared with a numerical model of the full component to extract the performance of the piezoelectric actuator.

3.2.3 Determination of the actuator performance

The specimen deformation is related to the strain induced by the actuator. An equivalent d_{33} value of the actuator can be derived combining the experimental results with a model description. A gradient based search method and a least-mean square approach matches the observed displacement with a Finite Element Model to obtain the strain per volt coefficient of each actuator.

Finite Element Model

A FEM model is made for each specimen. The model uses the dimensions measured on each sample after bonding the actuator and the composite substrate together. It is a 3-dimensional Finite Element Model using multilayer solid elements for the composite substrate and thermal elements for the active element. Typically, shell elements are used for modelling the behaviour of composite beams. Due to the 3-dimensional strains developed by the piezoelectric component, solid elements with thermo-mechanical are used. The modelling approach is validated using analytical solutions from the Classical Laminate Theory. The model considers only the active area of the actuator as shown in Figure 3.4. The assumptions are that the effects of the bondline and the epoxy material on the side of the actuators are small compared to the strains generated by the active part of the component and that the substrate used has consistent mechanical properties between specimens.

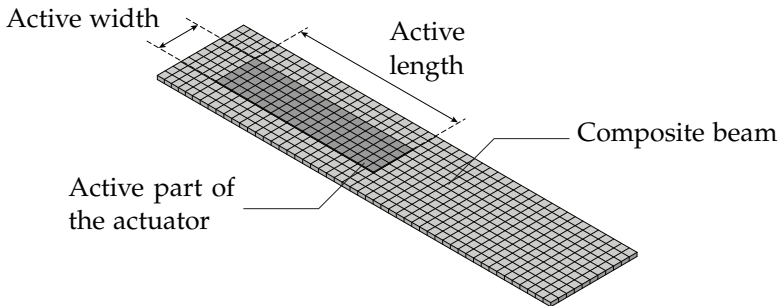


Figure 3.4: 3D rendering of the Finite Element Model showing the model geometry and mesh for the MFC actuator.

The thermal analogy between the reduced piezoelectric equation (2.9) is used. Applying a voltage on the actuator corresponds to an increase in the temperature for the model. Finally, only the coefficient of thermal expansion in the direction of the actuator length is considered because MFC actuators can be approximated as a pure d_{33} actuator [76]. The same assumption can be made on the d_{33} patch actuator: due to the conditioning of the stack slice, the actuator is not expected to show any significant strain in the directions orthogonal to the length of the actuator.

Gradient based search

The FEM model is implemented inside a gradient based search algorithm. The objective of the algorithm is to minimise the deviation between the displacements measured to the displacements derived from the FEM analysis. The parameter that is modified is the coefficient of thermal expansion used to model the piezoelectric effect. The algorithm stops when the minimum is reached. This means that the piezoelectric properties represented by the coefficient of thermal expansion in the model corresponds to the value of the piezoelectric properties of the specimen tested.

3.3 Results and discussion

3.3.1 Comparison with manufacturer specifications

The experiments resulted in a displacement map for each specimen tested. The displacement along the centre of the specimen is extracted and the standard deviation over the width is calculated. Figure 3.5 shows the deflection of each specimen tested and the deflection obtained by the numerical model after optimisation of the piezoelectric actuator strain charge coefficient. The properties of each actuator are derived from the strain charge component optimised by the gradient based search using the piezoelectric equations laid down in Chapter 2. The comparison with data from the manufacturer reveals that the MFC specimen performs close to the expected performance as shown in Table 3.3. A larger deviation is observed for PI d_{33} specimens. They show better performance than expected from the material properties. Typically, the availability of material properties is limited and data is given with an uncertainty of $\pm 20\%$ [70].

Table 3.3: Experimental measurements for the MFC sample and the average of the three d_{33} actuator specimens. Comparison is made with the reference data presented in Table 3.2.

Sample reference	Free strain per volt ($\mu\text{strain}/\text{V}$)	Reference ($\mu\text{strain}/\text{V}$)	Deviation
MFC-4010 P1	0.87	0.93	-6.5%
PI d_{33} Specimens	8.2	7.27	+13%

3.3.2 Comparison of the two actuator technologies

The actuators manufactured by Physik Intrumente and Smart-Material are significantly different which makes the side-by-side comparison of both technologies non-standard. Therefore, only parameters that do not depend on the size can be

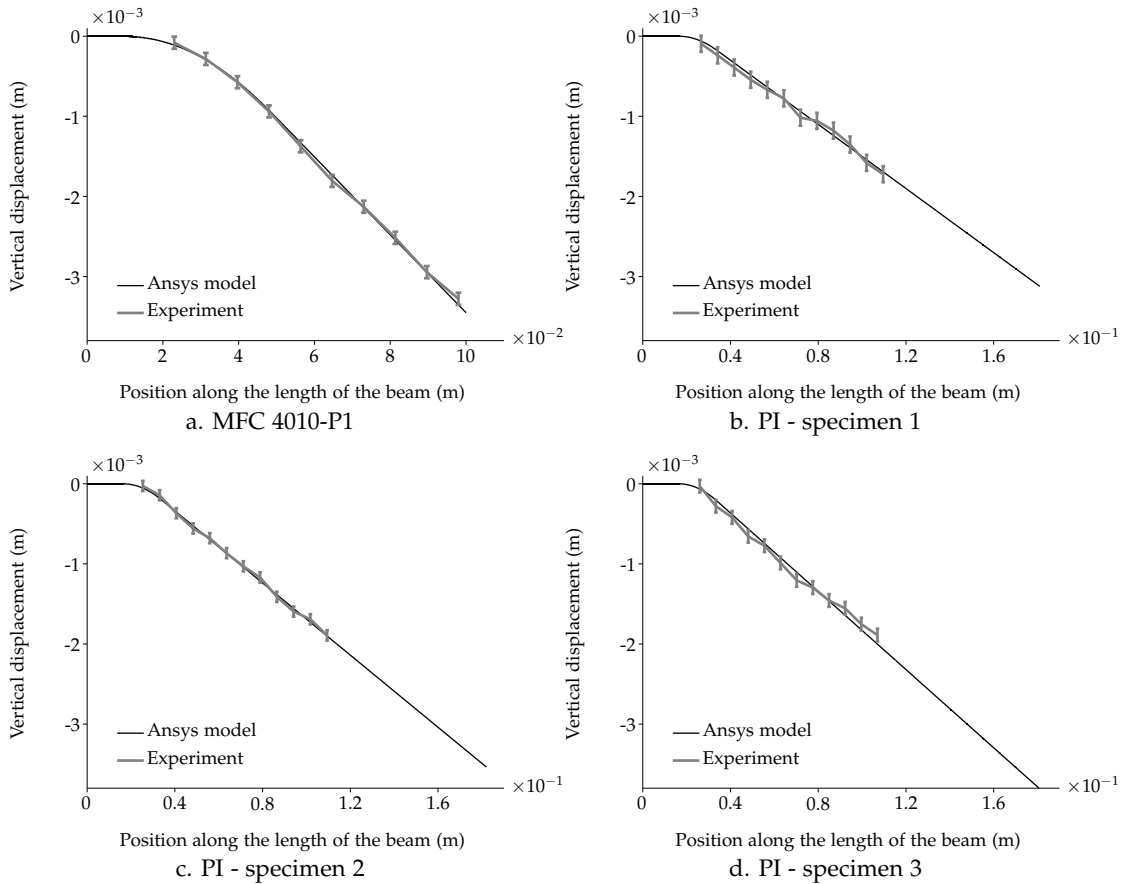


Figure 3.5: Comparison of the measurements with the FEM analysis for each sample tested. The error bars represent the standard deviation derived for each test performed.

compared. Three parameters are chosen: the strain per volt, the maximum free strain and the equivalent d_{33} coefficient of the actuator.

Strain per volt

In terms of strain per volt, there is an order of magnitude difference between the two types of actuator. The d_{33} actuator from Physik Instrumente requires a 10 times lower voltage than the Smart-Material actuator to achieve the same strain. This is a direct consequence of the small spacing between the electrodes of Physik

Instrumente actuator. Equation 2.4 applied to these actuators leads to:

$$\varepsilon_3 = d_{33} \frac{V}{l_e} \quad (3.1)$$

where V is the applied voltage and l_e is the spacing between two electrodes. Rearranging equation (3.1) gives the voltage as a function of the strain in the length of the actuator.

$$V = \frac{\varepsilon_3 l_e}{d_{33}} \quad (3.2)$$

Therefore, a smaller electrode spacing results in a smaller voltage required for the same output strain ε_3 as shown in Table 3.3.

Equivalent d_{33} coefficient

The piezoelectric coefficients of the actuators relate directly to the properties of the piezoelectric materials with a simple geometry like a plain sheet of piezoelectric material. The two actuation technologies have a complex geometry and their performance depends on the ability of the electrode to provide an appropriate electrical field inside the piezoelectric material. Calculating the value of the piezoelectric constant as if these actuators were made of a plain sheet of piezoelectric material provides an indication of the efficiency of these solutions.

Table 3.4: Comparison of the performances of the d_{33} patch actuator and the MFC actuator. The deviation is defined as the difference between the two actuators relative to the MFC (used as a reference).

Properties	MFC 4010-P1	PI- d_{33} actuator	Units	Deviation
PZT d_{33} coefficient	460	400	pC/N	-13%
Equivalent d_{33} coefficient	440	450	pC/N	+2%
Electrode spacing	500	55	μm	-89%
Max operating voltage	1500	130	V	-91%
Max operating electrical field	3.0e+6	2.4e+6	V/m	-20%
Max free strain	1300	1100	μstrain	-18%

The equivalent d_{33} coefficient is slightly higher for the Physik Instrumente actuator than for the Smart-Material actuator despite the lower material properties as shown in Table 3.4. This result tends to show the superior design of the d_{33} patch actuator, which manages to take significantly better advantage of the material properties despite lower material properties and lower electrical field. The design of the MFC actuator and its pattern of interdigitated electrode cannot efficiently apply an electrical field within the piezoelectric fibres [76, 101]. The geometry requires the electrical paths to go through the length of the fibres as shown in

Figure 3.1. Nevertheless, it remains unclear whether the PI actuators' larger efficiency comes from a slightly better piezoelectric material than expected by the specifications. A study using the same material properties for the two actuator geometries would allow to affirm with more conviction the superior efficiency of the d_{33} patch actuator over the MFC. This task is especially challenging given the typical uncertainty around the material properties given by the manufacturers.

Maximum free strain

The free strain of an actuator is defined by the amount of deformation when no mechanical load is applied on the actuator. The maximum free strain defines the operational limit of a piezoelectric actuator. It is the largest deformation observed under the maximum operational voltage.

$$\epsilon_{3 \max}^{\text{free}} = d_{33} \frac{V_{\max}}{l_e} \quad (3.3)$$

where $\epsilon_{3 \max}^{\text{free}}$ is the maximum free strain and V_{\max} is the maximum operating voltage. The MFC maximum free strain is larger by 18% as shown in Table 3.4, thanks to the superior maximum operating electrical field in a MFC.

3.4 Conclusion

Physik Instrumente d_{33} patch actuators deliver a performance close to the level of MFC actuators while reducing the voltage by almost an order of magnitude to achieve the same strain. This is due to the thin spacing between the electrodes, as the structure is manufactured from a conventional piezoelectric stack actuator. The result is a better use of the piezoelectric capabilities of the material compared to MFCs as the electrical field is applied directly through the material length. The only disadvantage of this actuator is the reduced maximum operational electrical field which lead to a lower free strain at the maximum operational voltage.

The assessment of each actuator technology according to the selection process laid down in the previous chapter determines the most suitable actuator for a specific application. The two actuation technologies compared in this chapter are well suited for the high performance required for actuation in a helicopter rotor blade. PI actuators are especially relevant for integrating an actuation technology inside a rotor blade where transmitting large voltages through the rotor hub is not practical. The following chapter investigates the aerodynamic loads on the Gurney flap to perform the actuator selection and start the design of the actuation system.

The Gurney flap: aerodynamic forces

4.1 Introduction

The active Gurney flap system aims to improve the lift of a rotor blade for certain azimuthal positions during its revolution. Wind tunnel tests are necessary to validate the Gurney flap as a relevant technology for helicopters. The objective of this chapter is to investigate the aerodynamic forces applied on the Gurney flap for a Mach-scaled blade. The knowledge of the mechanical constraints on the Gurney flap will provide the requirements for selecting an actuation technology and designing an actuation mechanism in the following chapters. Two-dimensional Computational Fluid Dynamics (CFD) simulations are used to derive the value of the force experienced by the Gurney flap. The CFD model utilised is detailed and validated against a reference blade. The addition of the Gurney flap is then compared against reference in the literature showing the relevance of this model for the Gurney flap. This chapter concludes with the total mechanical work required to fold the Gurney flap in the case of a reverse deployment mechanism.

4.1.1 Baseline blade definition

The blade profile and specifications were defined for all the partners of the Green Rotorcraft Consortium to provide a common ground for the investigation of the Gurney flap technology [102]. As part of the definition of the blade, aerodynamic tables were provided by Agusta Westland for a NACA 23012 profile with a 0.65 m chord length. This profile was considered in the earliest phases of the programme to investigate the active technologies available. The NACA 0012 profile replaced

the NACA 23012 for subsequent studies once the Gurney flap technology was selected. The aerodynamic tables give the section lift and drag coefficient of the aerofoil over a wide range of angles of attack and airflow speeds. The section lift and drag coefficients are dimensionless numbers defined for all sections of the blade. They show how much lift and drag are generated by a profile geometry. The simulation is validated with the aerodynamic tables of the NACA 23012 profile. The NACA 0012 profile is taken for the simulation of the profile with the Gurney flap and the calculation of the mechanical constraints. The section lift coefficient (c_l) is defined by:

$$c_l = \frac{f_l}{\frac{1}{2}\rho v^2 c} \quad (4.1)$$

where f_l is the component of the force normal to the incoming flow generated by the section profile per metre of wingspan, ρ is the air density, v the airflow speed and c the chord length as shown in Figure 4.1. The section drag coefficient (c_d) is defined by:

$$c_d = \frac{f_d}{\frac{1}{2}\rho v^2 c} \quad (4.2)$$

where f_d is the component of the force in the direction of the incoming flow generated by the section profile per metre of wingspan.

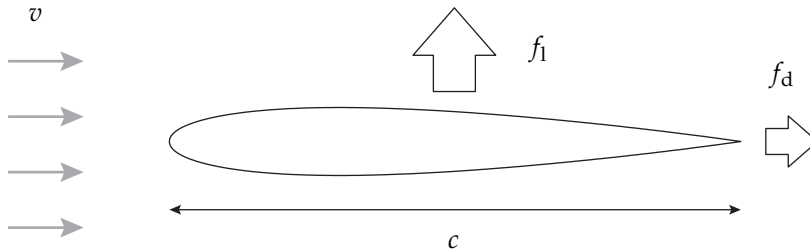


Figure 4.1: Sketch of a NACA 0012 blade with the parameters used for the calculation of the section lift and drag coefficients.

4.1.2 Mach-scaled rotor blade

To validate the active Gurney flap, a Mach-scaled model blade is considered. The motivation for a Mach-scaled blade is the scaling of compressibility effects. This scaling is typically used for wind tunnel testing [12, 15, 99, 103, 104]. The aim is to verify the aerodynamic behaviour of the Gurney flap during the rotation of the blade. The Mach number (Ma) characterises the compressibility effects in the flow

around an aerofoil. The Mach number is the ratio between the speed of sound in the air (c_{air}) and the velocity of the airflow (v):

$$Ma = \frac{v}{c_{\text{air}}} \quad (4.3)$$

The speed of sound in the air varies with temperature. For the calculation of the Mach number, the speed of sound used is $c_{\text{air}} = 343\text{m/s}$ which corresponds to the speed of sound at 20°C . When the Mach number is small (i.e $Ma < 0.3$), the flow can be considered as incompressible [105]. For larger Mach numbers, compressibility effects arise, creating phenomena like shock waves and expansion waves. The flow velocity experienced by a helicopter blade depends on the position along the blade. To keep identical Mach numbers along the length of both blades, the tip speed of the model blade is kept identical to the tip speed of the full-scale blade. Therefore, the Mach number and the compressibility effects vary along the blade for both the full-scale and the scaled model blade as shown in Figure 4.2.

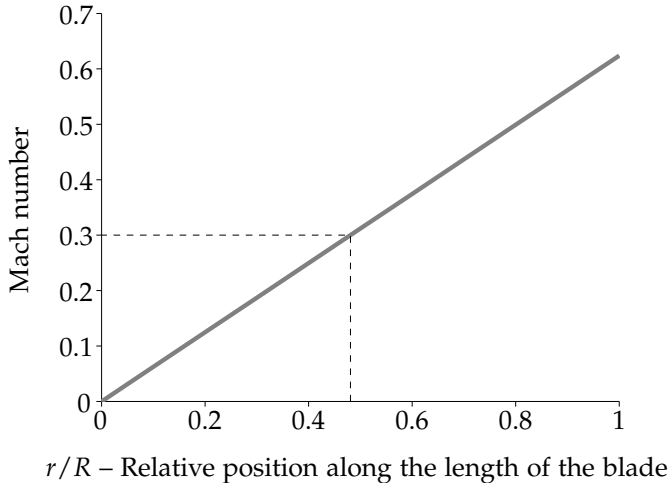


Figure 4.2: Range of Mach numbers for a rotor blade with a tip speed of 214 m/s. The dotted line represents the compressible flow regime threshold of Mach 0.3.

In the scope of this project, a model blade with a length of 1 m model is chosen. Therefore all the dimensions are reduced by a factor of 8 as shown in Table 4.1, whereas the rotation speed is increased by a factor of 8.

4.2 Computational Fluid Dynamics

To investigate the pressure around the rotor blade profile, a CFD model is created in Comsol Multiphysics software [106]. Comsol implements the Navier-Stokes

Table 4.1: Comparison of the dimensions of the full-scale blade defined in the baseline blade definition and an eighth-scale Mach-scaled model blade.

Properties	Full-scale	Model blade
Blade length	8.15 m	1.02 m
Chord length	65 cm	81 mm
Rotation speed	26.26 rad/s	210 rad/s
Tip speed	214 m/s	214 m/s

equations in a Finite Element environment. The equations are briefly outlined in the following section.

4.2.1 Theory

The Navier-Stokes equations relate the airflow speed to the pressure for a small volume element of flow within an Eulerian reference frame. The Navier-Stokes equations are derived from the continuity and the conservation of momentum equations [107, 108]. The tensor notation is utilised for convenience, in contrast to Chapter 3 where the matrix notation was used. The general formulation of the Navier-Stokes equations is:

$$\frac{\partial \rho}{\partial t} + \nabla \cdot (\rho \mathbf{v}) = 0 \quad (4.4)$$

$$\rho \left(\frac{\partial \mathbf{v}}{\partial t} + \mathbf{v} \cdot \nabla \mathbf{v} \right) = -\nabla p + \nabla \cdot \mathbf{T} + \mathbf{f} \quad (4.5)$$

where ρ is the fluid density, \mathbf{v} the flow velocity, p the pressure, \mathbf{T} the viscous stress tensor and \mathbf{f} the external forces per unit volume. For low Mach numbers, the flow is assumed to be incompressible and the fluid Newtonian: the viscosity and the density of the fluid are constant everywhere in the fluid domain [105]. Under these conditions, the Navier-Stokes equations become:

$$\rho \nabla \cdot \mathbf{v} = 0 \quad (4.6)$$

$$\rho \left(\frac{\partial \mathbf{v}}{\partial t} + \mathbf{v} \cdot \nabla \mathbf{v} \right) = -\nabla p + \mu \nabla^2 \mathbf{v} + \mathbf{f} \quad (4.7)$$

where μ is the dynamic viscosity of the fluid. The expression of the stress tensor for this case is detailed in [107]. Given the previous assumptions, the above form of the Navier-Stokes equations model the flow accurately for low Mach numbers [105].

The nature of the flow around a helicopter is complex due to the significant change of conditions between the root and the tip of the blade. The Reynolds number provides a measure of the ratio between the inertia and viscous force and

therefore gives an indication about the nature of the flow. The Reynolds number Re definition is:

$$Re = \frac{vc\rho}{\mu} \quad (4.8)$$

A flow along an external surface is most likely laminar for a Reynolds number smaller than 5×10^5 , for larger Reynolds numbers the flow is most likely turbulent [109, 110]. Due to the difference in chord length between the full-scale blade and the model blade, the Reynolds number is different for these two cases as shown in Figure 4.3.

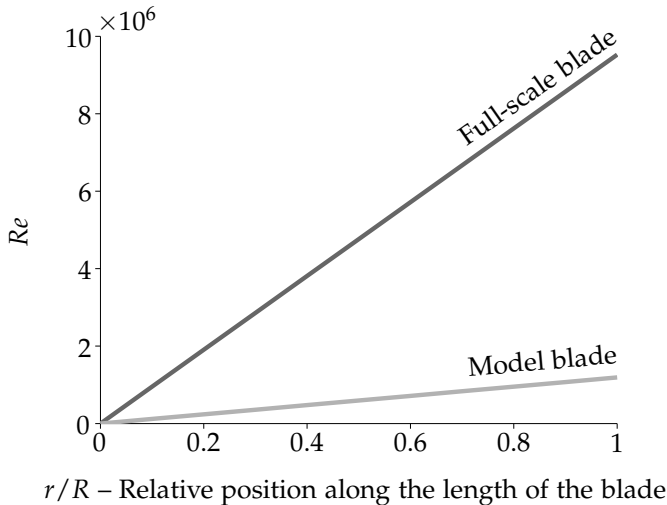


Figure 4.3: Reynolds number for the full-scale (—) and the model blade (—) along the length of the rotor blade.

Comsol Multiphysics provides various turbulence models to take into account the flow transition from laminar to turbulent. The model chosen here is the k - ϵ turbulence model implemented within Reynolds-Averaged-Navier-Stokes equations (RANS). RANS equations decompose the fluid flow into an averaged part and a fluctuating part. The effects of the velocity fluctuations on the mean flow are calculated using a turbulence model while the averaged part corresponds to the mean flow. The k - ϵ turbulence model provides transport equations for the turbulence kinetic energy k and the dissipation rate of turbulence energy ϵ [111]. This approach provides an efficient way of formulating flow problems for numerical computations [112, 113, 114].

4.2.2 Finite Element Model

The flow around a helicopter blade is highly complex due to its 3D characteristics. Nevertheless, the assumption is made that the force on the Gurney flap is not dependent on the flow along the blade is taken, such that the flow problem can be solved with a 2D analysis. This section will discuss the spatial discretization of the model which is paramount for the numerical solver to converge and correctly solve the aerodynamic equations.

Boundary layer

The boundary layer is the thin region of fluid adjacent to the surface of the profile. The viscous effects are the most significant in this layer. The laminar flow in the boundary layer transitions into a turbulent flow at the transition point, changing the thickness of the boundary layer and the velocity profile [105, 108, 109]. To correctly model the boundary layer, very small elements are required close to the profile surface in order to accurately capture the flow velocity distribution as shown in Figure 4.4.

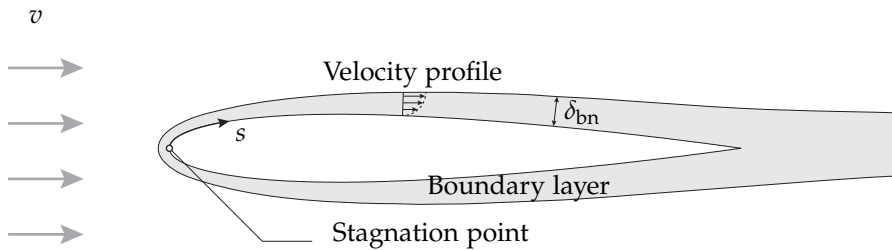


Figure 4.4: Sketch of the boundary layer. Its thickness is emphasised for clarity.

The boundary layer thickness in the case of a laminar flow (δ_{bn}^{lam}) can be obtained from laminar boundary layer theory [105]:

$$\delta_{bn}^{\text{lam}} = \frac{5.2s}{\sqrt{Re_s}} \quad (4.9)$$

where s is the surface coordinate along the aerofoil contour, starting at the stagnation point and Re_s is the local Reynolds number defined as:

$$Re_s = \frac{vs\rho}{\mu} \quad (4.10)$$

Unlike the case for a laminar boundary layer, the thickness of a turbulent boundary layer (δ_{bn}^{tur}) cannot be derived from theory [105]. The following approxi-

mate formula obtained from experimental work is commonly used in the case of a turbulent flow [105]:

$$\delta_{bn}^{\text{tur}} = \frac{0.37s}{Re_s^{0.2}} \quad (4.11)$$

In order to accurately capture the velocity profile in the boundary layer close to the surface of the profile, the spatial discretization must be sufficiently fine in the vicinity of the aerofoil boundary. Therefore, the thickness of the first element must be much smaller than the thickness of a turbulent or laminar boundary layer regardless of both the chordwise and spanwise position along the blade and the nature of the boundary layer. The boundary layer can be evaluated from equations (4.9) and (4.11). The transition between the laminar and turbulent nature of the boundary layer can be assumed to happen when the local Reynolds number reaches the critical value of 5×10^5 . The thickness of the first element (e_{bn}) is linked to the Reynolds number with the following rule of thumb (used by Agusta Westland):

$$e_{bn} = \frac{10c}{Re} = \frac{10\mu}{v\rho} \quad (4.12)$$

This rule ensures that the first element is at least an order of magnitude smaller than the thickness of the laminar boundary layer as shown in Figure 4.5. The element size criterion is independent of the chord length as shown in equation (4.12), this rule is therefore valid for any profile scale. No assumption is made on the flow transition in the boundary layer, which is shown as a sharp increase of the boundary thickness in Figure 4.5. In reality, the transition occurs gradually.

Domain size

For Computational Fluid Dynamic (CFD) simulations, a large domain size is required relative to the profile chord length (c) to avoid effects from the domain boundaries [115]. The size of the domain depends on the complexity of the flow and the number of dimensions considered [116, 117, 118, 119]. Recommendations are followed for this model that combines large angles of attack and a Gurney flap. The dimensions taken are $30 c$ in front, above and below the profile and $40 c$ behind the profile as shown in Figure 4.6. Choosing the chord length as a parameter of the domain size ensures that a suitable domain is created for a profile of arbitrary size. The shape of the domain corresponds to the C-grid meshing used and will be detailed in the following section.

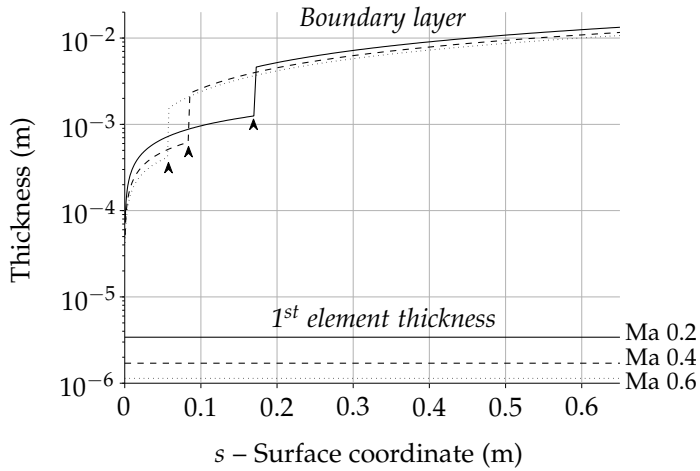


Figure 4.5: Boundary layer thickness and thickness of the first element for various speed conditions in the case of the full-scale NACA 23012 blade profile for Ma 0.2 (—) Ma 0.4 (---) and Ma 0.6 (.....). The arrows indicate the location of the flow transition for each condition.

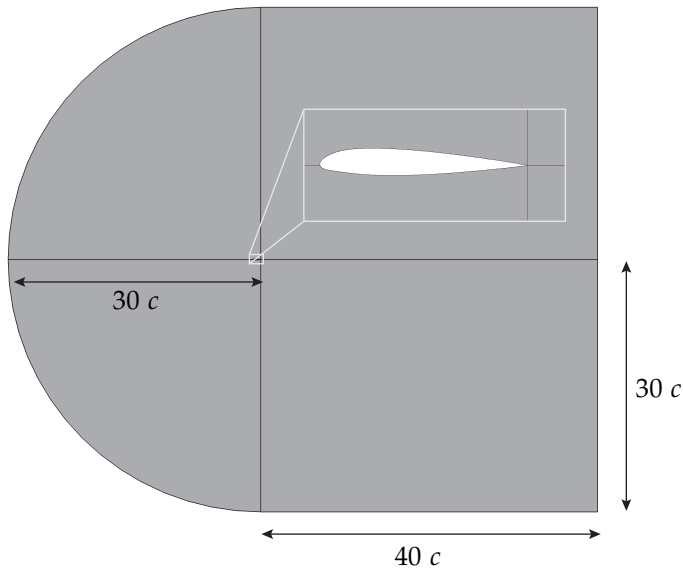


Figure 4.6: Size of the domain used for blade CFD simulations.

Mesh

Many meshing strategies are available for aerofoils [119, 120, 121, 122, 123]. Quadrilateral elements inside a C-grid mesh are chosen for their performance.

Unstructured triangular meshes are less desired because they will generally lead, for the same number of grid points, to less accurate results [119]. Moreover, they do not provide the same level of control for creating meshes suitable for CFD simulations with very thin elements across the boundary layer. The C-grid mesh consists of curved elements wrapped around the front of the profile and rectangular elements behind it as shown in Figure 4.7. Such a mesh creates long and thin elements close to the profile boundary. This is desired for a flow simulation to accurately capture the flow velocity profile close to the profile boundary [109].

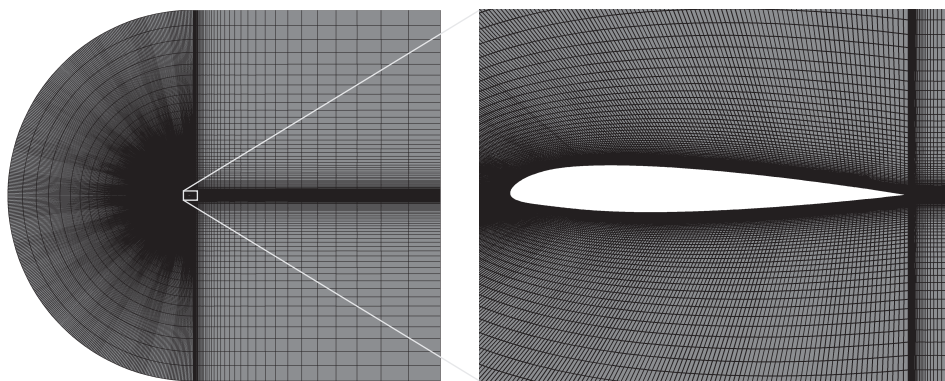


Figure 4.7: C-grid mesh used for modelling NACA 23012 aerofoil.

The size of the elements can be large on the domain boundaries but elements on the aerofoil boundary need to have a very small thickness. The thickness of the boundary layer has been discussed in the section on the boundary layer to provide a simple rule for the size for the first element (equation 4.12). A geometric sequence is implemented to gradually increase the element thickness from the aerofoil to the limits of the domain. The coefficients of the geometric sequence are set to have 150 elements from the profile to the front, top and bottom boundaries and 100 elements behind the profile. The rotor blade profile is described with 400 points to guarantee a smooth discretization. The resulting mesh is displayed in Figure 4.7 and consists of approximately 93,000 elements. These numbers are chosen based on considerations detailed in Appendix A.

4.2.3 Comparison with aerodynamic data

Simulations of the NACA 23012 profile are performed for velocities ranging from Mach 0.3 to Mach 0.6 and angles of attack from -10 to +10 degrees. The velocity range chosen corresponds to the typical velocity range and angles of attack that a blade section will encounter during a flight. Although the velocity at the tip of the blade will exceed Mach 0.6 during a forward flight, such velocities will

not be reached in the main lifting part of the blade. The range of angles of attack corresponds to the linear aerodynamic response of the blade in which the blade is typically operating. The pressure distribution and the velocity over the entire domain are retrieved from the simulation results. The obtained pressures are integrated over the profile surface to get the corresponding force in the vertical and horizontal directions. The section lift and drag coefficients are then calculated using equations 4.1 and 4.2. This data is compared to the NACA 23012 aerodynamic data from the table provided in the Baseline Blade Definition [102].

Lift coefficient

The lift coefficients obtained from the RANS method with $k-\epsilon$ turbulence model are corrected using Prandtl-Glauert rule to account for the first order compressibility effects [124]. The section lift coefficients corrected compare very well to the reference data over the -10 $+10$ angle of attack range as shown in Figure 4.9.

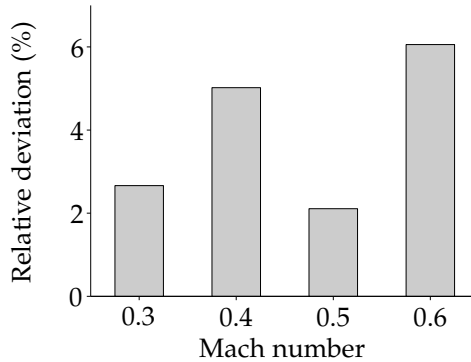


Figure 4.8: Deviation of the slope of the computed section lift coefficient curve relative to the reference NACA 23012 data for the Mach numbers considered.

The deviation between the reference lift and the lift from the simulation increases with the Mach number. The slope of both curves is derived in order to calculate the deviation of the simulation relative to the reference as shown in Figure 4.8. The $k-\epsilon$ model is capable of predicting the section lift coefficient in the linear range of the blade aerodynamic response. The relative deviation of the lift slope compared to reference data does not exceed 6.1% over the range of airflow speeds experienced by a rotor blade.

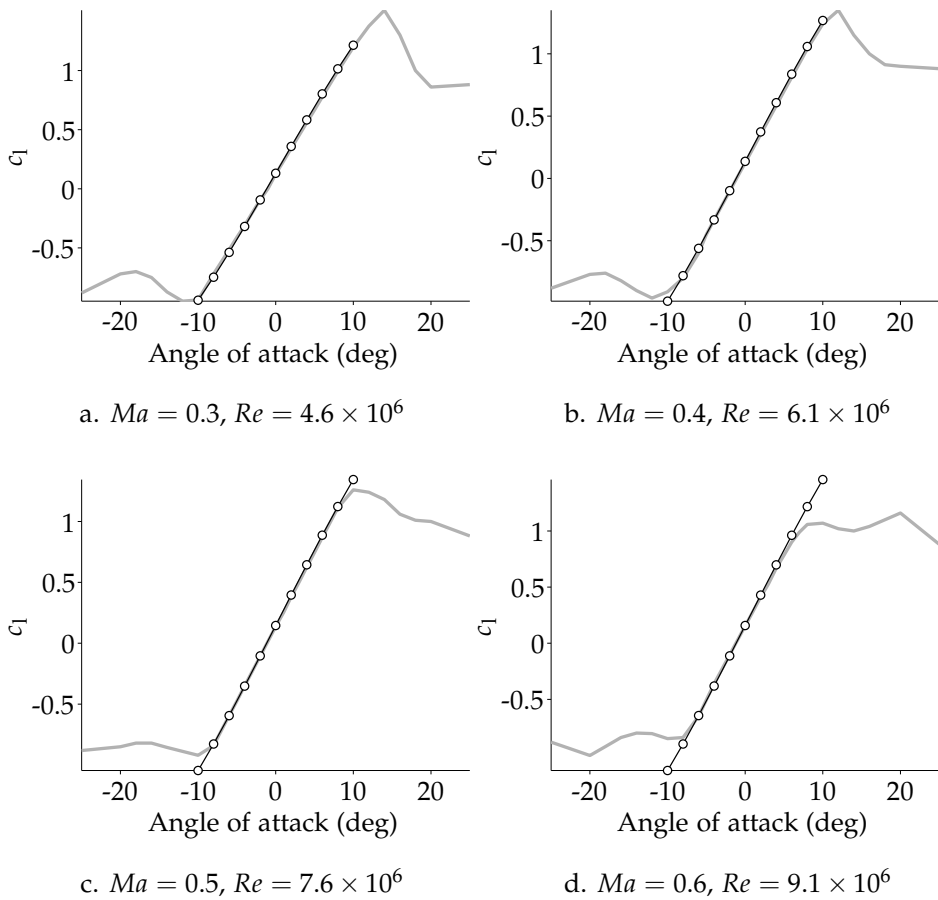


Figure 4.9: Comparison of the section lift coefficient from the $k-\epsilon$ turbulence flow simulation (\circ —) and the reference data (—), for the NACA 23012 blade profile for various Mach numbers.

Drag coefficient

The drag curves obtained from the simulation display a large difference with the drag curves in the reference data as shown in Figure 4.10. The calculated drag is always lower than the reference drag. The drag of a body is actually a combination of pressure drag and skin friction drag [109]. Pressure drag is due to flow separation which creates large pressure differences between the leading edge and trailing edge of an aerofoil. The skin friction drag is caused by the viscous shear stress at the aerofoil wall. For a low Reynolds number flow, the skin friction drag is dominant because there is no flow separation [124]. To estimate the drag accurately, complex

models are required to predict the viscous effects in the boundary layer and thus the skin friction drag [125]. The $k-\varepsilon$ turbulence model used here is not capable of predicting the skin friction drag correctly [109].

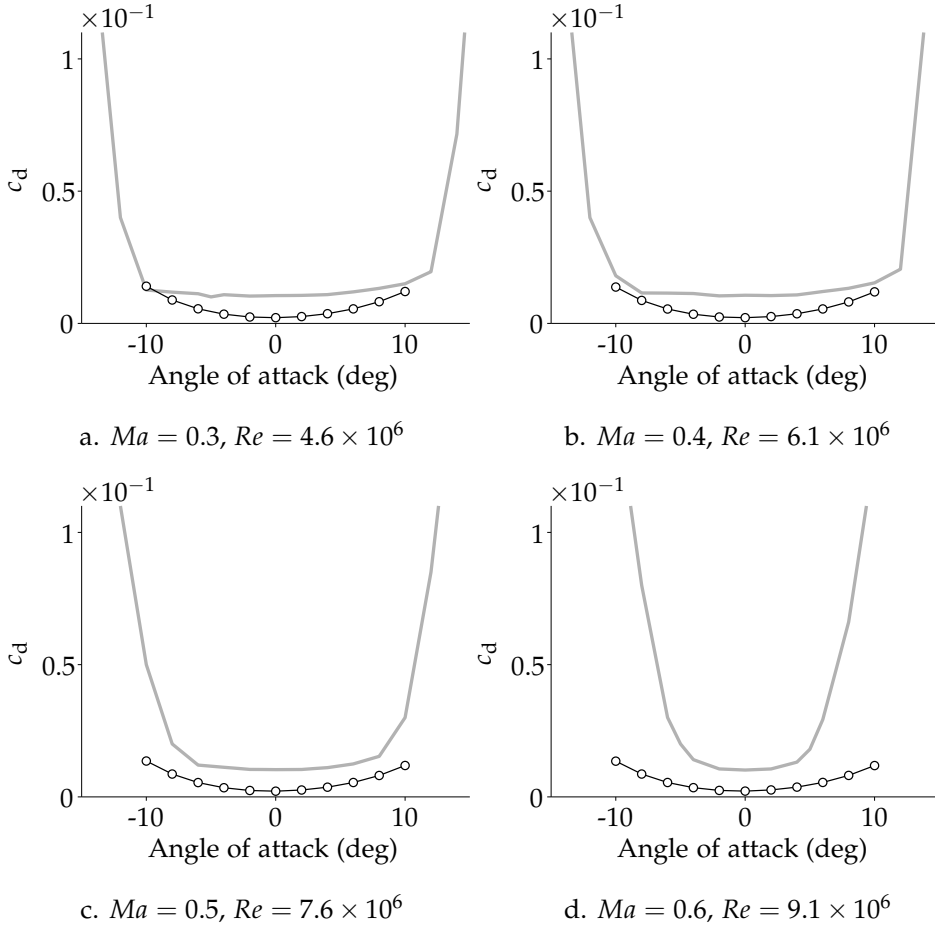


Figure 4.10: Comparison of the section drag coefficient predicted by the $k-\varepsilon$ turbulence simulation ($\circ-\circ$) and the reference data ($—$) for various Mach numbers for the NACA 23012 blade profile.

Although the $k-\varepsilon$ model falls short in estimating the section drag coefficient, it provides an accurate calculation of the section lift coefficient. The inaccuracy in the skin friction drag observed with this model does not significantly affect the calculation of the force on the Gurney flap because the relevant force is normal to the Gurney flap surface and not along its length. The skin friction drag has therefore a negligible effect on the calculation of the aerodynamic constraints for the Gurney

flap [126]. The following section presents simulations of a model scale NACA 0012 profile with a Gurney flap.

4.3 The Gurney flap

The Gurney flap was chosen as a technology to improve the lift of an aerofoil without significantly increasing the drag [127]. The Gurney flap efficiency depends on its size and placement. The optimal performance is achieved by a Gurney flap placed at the trailing edge of the aerofoil [22, 128]. A typical length for the Gurney flap is 2% of the profile chord length [22, 24, 25, 56, 128]. Studies currently show that the additional lift due to larger Gurney flaps is outweighed by the additional drag [22, 24, 128]. The profile considered in the following section is the NACA 0012 aerofoil which replaced the NACA 23012 as the reference aerofoil for the blade.

4.3.1 Meshing strategies with the Gurney flap

The meshing around the Gurney flap is paramount to ensure convergence of the numerical solution process. A procedure is set up to automate the generation of the mesh for the variety of angles of attack and deployment angles of the Gurney flap used in the design. To achieve that, the domain is divided into additional blocks to avoid the need of unstructured mesh elements as shown in Figure 4.11.a. A refinement at the tip of the Gurney flap is included by a modification of the geometric series that controls the element thickness at a specific distance from the aerofoil contour as shown in Figure 4.11.b.

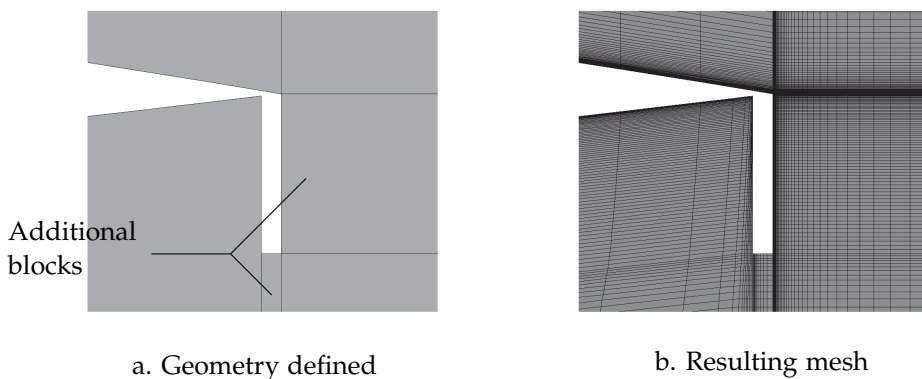


Figure 4.11: Refined geometry containing additional blocks for the meshing of the domain when the profile has a deployed Gurney flap.

The additional geometry blocks depends on key points on the profile geometry and therefore can be used for all the angles of attack considered and a large range of the Gurney flap deployment angles. The quality of the meshed elements decreases with lower deployment angles and especially below 45° . The elements are sheared to accommodate the deployment angle of the Gurney flap as shown in Figure 4.12.a. The skew angle is defined as the angle between the side of a quadrilateral element and the axis normal to the base of the element. It is a good measure of shape distortion for quadrilateral element. The objective is to adapt the procedure to avoid distorted elements due to the folding of the flap. The domain blocks behind the Gurney flap are modified to avoid distortion and to maintain a stable convergence towards the solution.

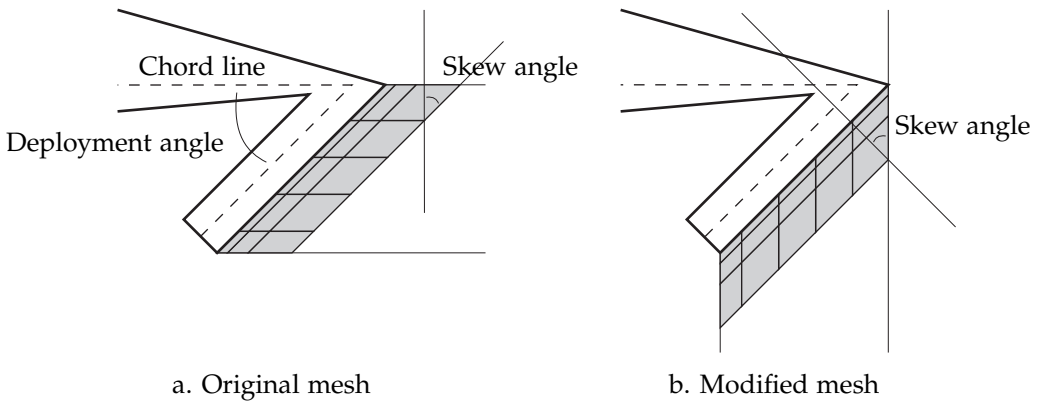


Figure 4.12: Sketch of the mesh modification.

To avoid larger skew angles and therefore more distorted elements, the additional blocks are modified for deployment angles smaller than 45° as shown in Figure 4.13. The skew angle is still 45° for the same deployment angle, but it is reduced for elements below the Gurney flap as the Gurney flap folds further, avoiding extreme deformations of elements as shown in Figure 4.12.b. For the elements between the Gurney flap and the aerofoil surface, no special refinement is performed as the element density increases with smaller angles of deployment. A fixed number of elements is set for meshing along the length of the Gurney flap. Therefore, reducing the space available between the Gurney flap and the aerofoil surface decreases the size of the elements ensuring stability of the solution algorithm and accuracy of the solution.

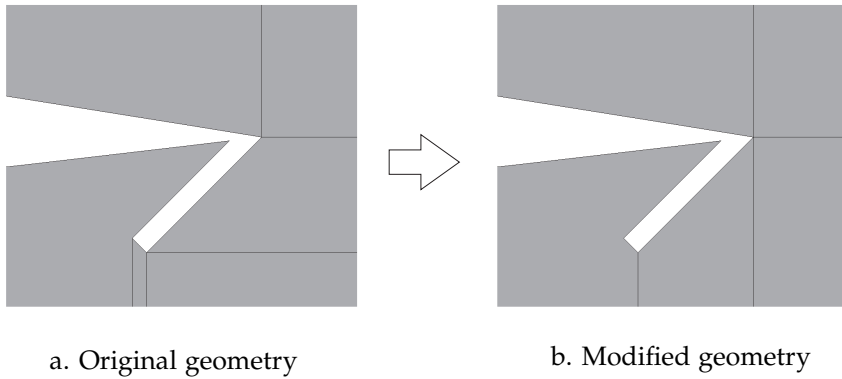


Figure 4.13: Modification of the geometry when the deployment angle falls below 45° of deployment.

The modification of the mesh is investigated to ensure the continuity of the results by comparing two simulations at 45° deployment angle. The consequence of the mesh modification on the pressure coefficient is negligible as shown in Figure 4.14. The deviation of the results on the modified mesh relative to the results on the original mesh is not exceeding 0.8% for the lift contribution of the Gurney flap.

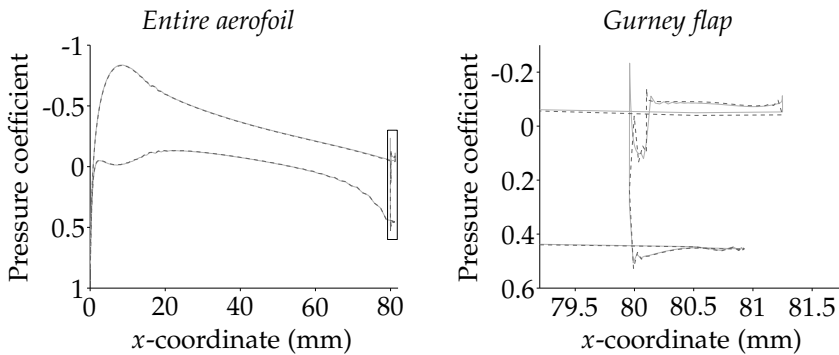


Figure 4.14: Pressure coefficient around the profile of the Mach-scaled NACA 0012 aerofoil with a Gurney flap deployed at 45° for the original mesh (—) and the modified mesh (- - -) at Mach 0.4. The angle of attack is 0° and $Re = 7.6 \times 10^5$. The graph on the right is a zoomed-in version of the left graph for the region around the Gurney flap.

4.3.2 The Gurney flap principle

Effects of the Gurney flap on the flow

The Gurney flap affects the flow by creating a low pressure zone behind the aerofoil trailing edge. As a consequence, the upper surface separation point is brought closer to the trailing edge. The separation point is the location where flow separation occurs on an aerofoil. Laminar flow is therefore present on a larger portion of the profile compared to an aerofoil without Gurney flap providing an increase in lift [24, 25, 129, 130, 131]. The flow around the Gurney flap presents some peculiar characteristics. Re-circulation zones are visible behind the aerofoil trailing edge [132, 133, 134, 135]. The results of the numerical simulation displays a similar pressure distribution and flow structure as shown in Figure 4.16.

Improvements due to the Gurney flap

The flow modified by the Gurney flap affects the overall lift and drag of an aerofoil. The lift is improved over the full range of angles of attack considered, as shown in Figure 4.15. The increase in lift comes at a drag cost [22, 24, 128]. However, it has been reported that the lift over drag ratio of the aerofoil is larger for the profile with the Gurney flap, showing that the aerofoil with the Gurney flap is more efficient. The drag penalty increases with the Gurney flap length. In the scope of the GRC project a Gurney flap with a length of 2% the aerofoil chord has been chosen to have significant lift improvement without an excess of drag for this present application [127].

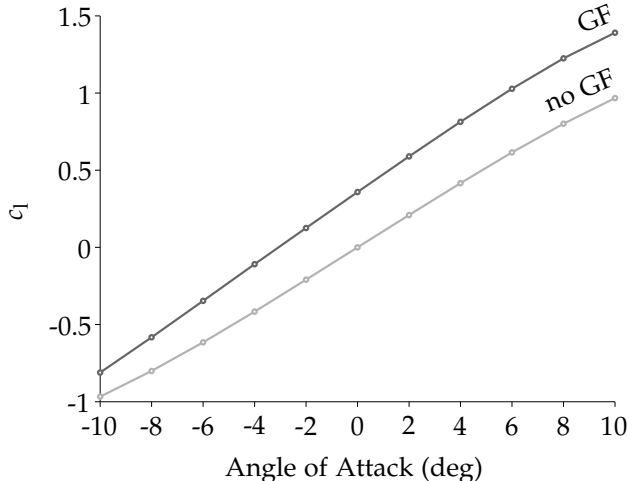


Figure 4.15: Lift curves for a 81 mm NACA 0012 aerofoil with a 2% chord Gurney flap (—○—) compared to an aerofoil without (—○—) for Mach 0.1, $Re = 1.9 \times 10^5$.

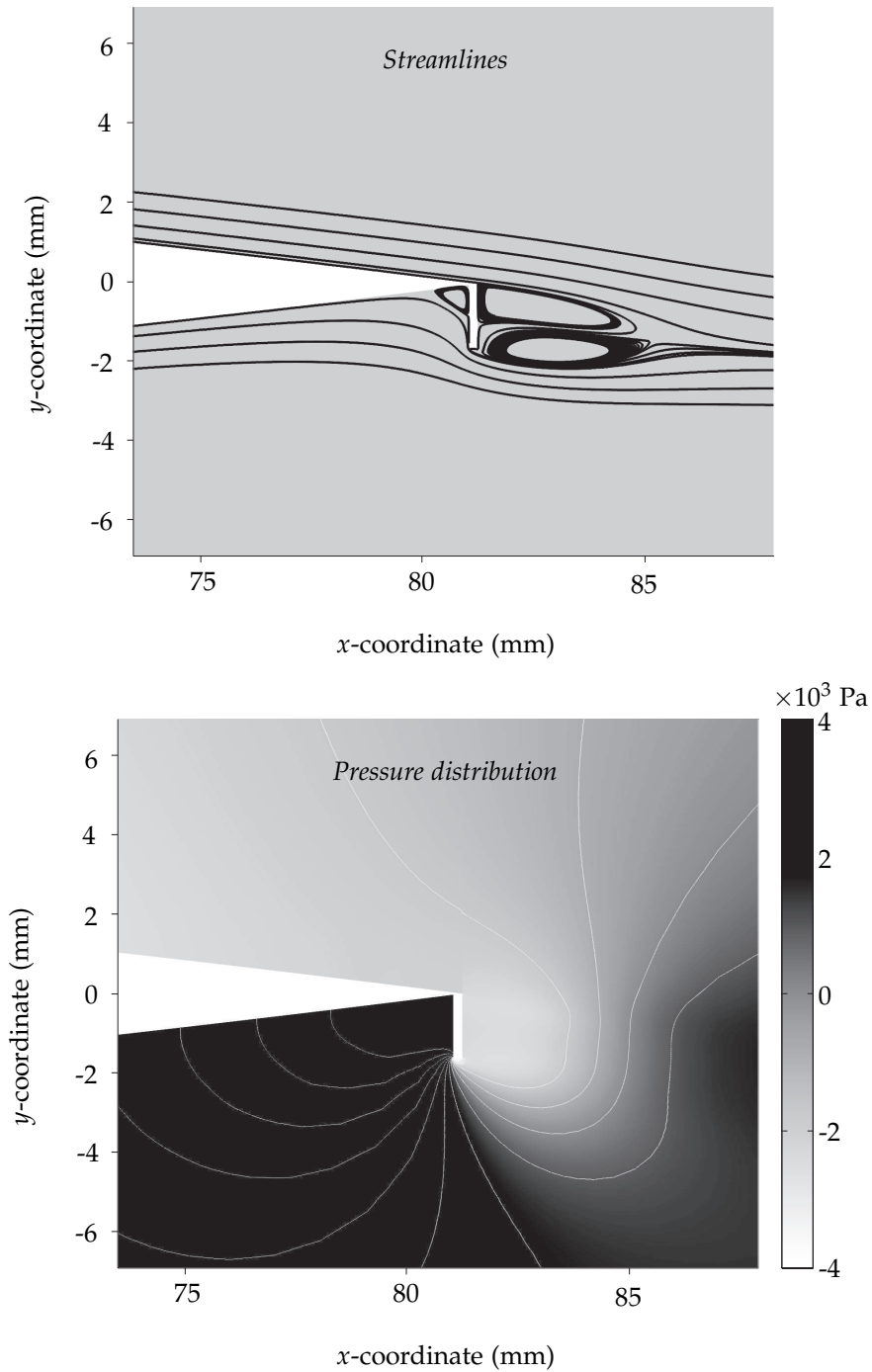


Figure 4.16: Streamlines and pressure distribution for a 81 mm NACA 0012 aerofoil with a 2% Gurney flap. The angle of attack is 0° , the velocity of the airflow is Mach 0.4 and $Re = 7.6 \times 10^5$.

4.3.3 Aerofoil section and Gurney flap for the Mach-scaled blade

NACA 0012 is the aerofoil considered for the investigation of the Gurney flap as mentioned in the introduction. The RANS method with the $k-\varepsilon$ turbulence model is used for numerically simulating the flow around this profile within a range of $\pm 10^\circ$ of angle of attack. This is the range where the simulations showed a good agreement with the section lift coefficient curve for the NACA 23012 profile, as shown in section 4.2.3. The Gurney flap performance depends on its size, therefore the Mach-scaled model blade needs to provide a relevant comparison to the full-scale helicopter blade. Regardless of the size of the profile, the Gurney flap length should be sufficient to extend beyond the boundary layer of the flow. This explains the inefficiency of a Gurney flap smaller than 1% of a profile chord length [22, 24, 128]. A comparison of the section lift is performed at low speed (Mach 0.1) to have a low Reynolds number and therefore a thick boundary layer as shown in Figure 4.5. The result reveals that a 2% Gurney flap affects the performance of both profiles with similar magnitudes as shown in Figure 4.17. The difference between the performance of the full-scale blade and the model blade is not exceeding 4%. The section lift coefficient of the model aerofoil is slightly lower than the section lift coefficient of the full-scale aerofoil because of the differences in boundary layer thicknesses. It is assumed that the difference in lift coefficient of the profile sizes is negligible. The calculation of the force on the Gurney flap is therefore performed on a 2% Gurney flap for the model aerofoil.

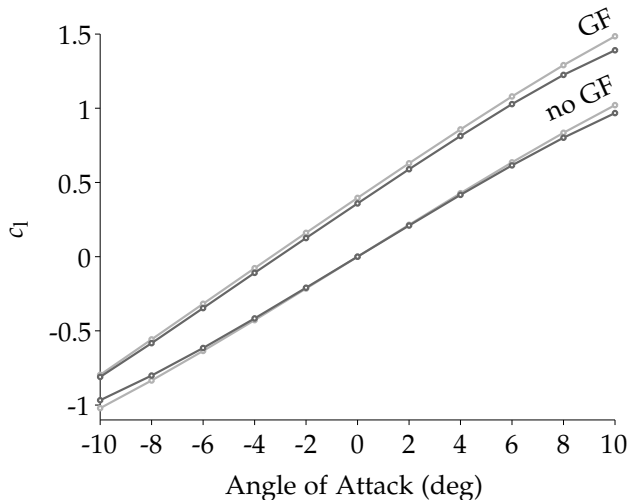


Figure 4.17: Comparison of the section lift coefficient between the full-scale ($-\circ-$) and the Mach-scaled ($-o-$) chord length for a NACA 0012 aerofoil at Mach 0.1 with and without a 2% Gurney flap. $Re_{\text{full-scale}} = 1.5 \times 10^6$, $Re_{\text{model-scale}} = 1.9 \times 10^5$.

4.4 Aerodynamic constraints on the Gurney flap

The RANS method with $k-\epsilon$ turbulence model predicts the lift on a profile, the flow patterns created by the Gurney flap and the pressure distribution around it. The aim of this chapter is to calculate the force the airflow exerts on the Gurney flap within a large range of angles of attack, airflow speeds and deployment angles as shown in Figure 4.18.

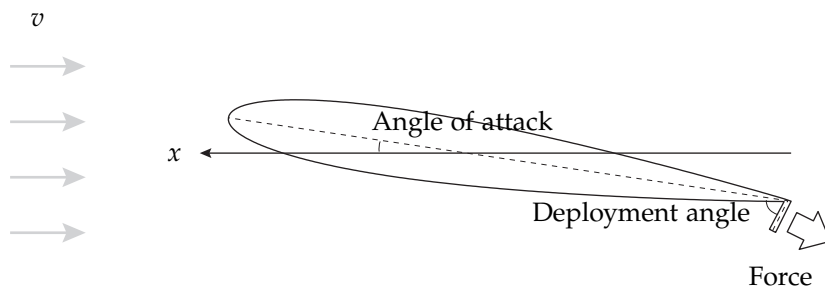


Figure 4.18: Sketch of the NACA 0012 aerofoil employed in the calculation of the force normal to the Gurney flap.

4.4.1 Force on the Gurney flap

The force on the Gurney flap is an integration of the pressure along the Gurney flap. Figure 4.19 displays the distribution of the force normal to the Gurney flap surface for a NACA 0012 model blade for angles of attack between $\pm 10^\circ$ for airflow speeds between Mach 0.1 and Mach 0.6 and for various deployment angles of the Gurney flap. The force peaks at 30 N/m. This level is reached at the tip of the blade when the Gurney flap is fully deployed and the blade is at 10° of angle of attack. This value gives the maximum load that the Gurney flap needs to sustain in operation while the loads for the deployment and the folding will be reduced because of the location of the Gurney flap, further away from the tip of the blade.

4.4.2 Maximum mechanical work required to fold the Gurney flap

For the reverse deployment mechanism chosen, the difficult transition is folding the Gurney flap back into the blade. In order to estimate the mechanical work required to fold the Gurney flap back in the blade, the moment at the root of the Gurney flap is calculated for the range of Gurney flap deployment angles. The worst combination of airflow velocity, angle of attack and deployment angle is used to obtain an upper bound for the mechanism selection. These conditions occur at the tip of the blade at the maximal angle of attack of 10° .

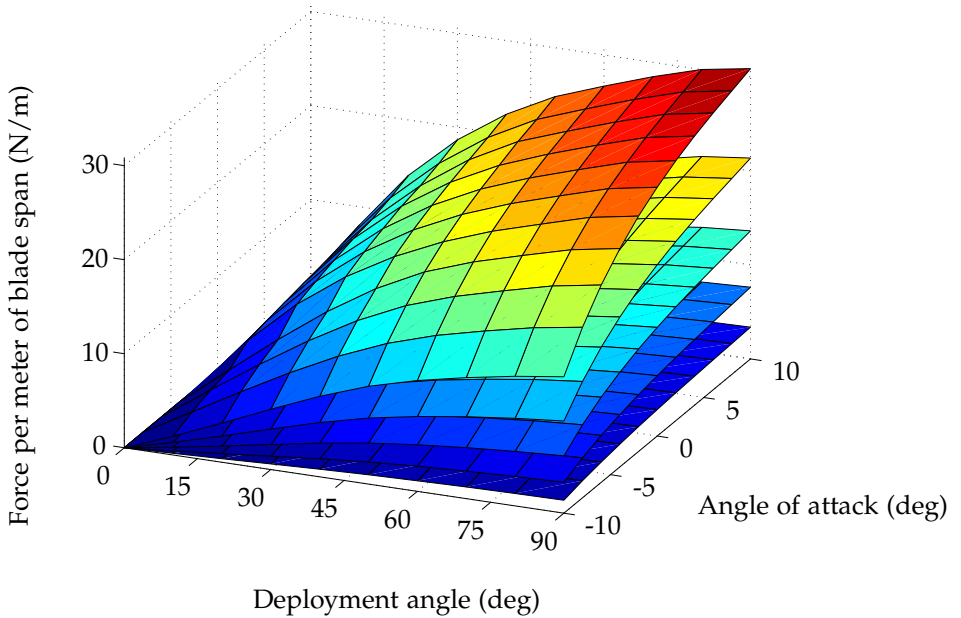


Figure 4.19: Normal force on a 2% Gurney flap for the NACA 0012 aerofoil of the model blade for various conditions. Layers from top to bottom: Ma 0.6, $Re = 11.4 \times 10^5$; Ma 0.5, $Re = 9.5 \times 10^5$; Ma 0.4, $Re = 7.6 \times 10^5$; Ma 0.3, $Re = 5.7 \times 10^5$; Ma 0.2, $Re = 3.8 \times 10^5$.

$$W_{GF} = \int_{-\frac{\pi}{2}}^0 M_{GF}(\beta) d\beta \quad (4.13)$$

where M_{GF} is the spanwise moment exerted by the flow at the root of the Gurney flap as shown in Figure 4.20. The angle β corresponds to the deployment angle of the Gurney flap. The result gives 30 mJ per metre of blade span. This value is a maximum value that will ensure that the mechanism will provide sufficient mechanical work for the operation of the Gurney flap whatever the state of the blade and the Gurney flap.

4.5 Conclusion

The results of the CFD simulation presented in this chapter focus on the determination of the force on the Gurney flap rather than on the performance of the aerofoil for the blade. The model detailed in this chapter captures the effects of the Gurney flap on the flow good enough to enable to accurately assess the surface pressure applied by the flow on the Gurney flap. The normal force and

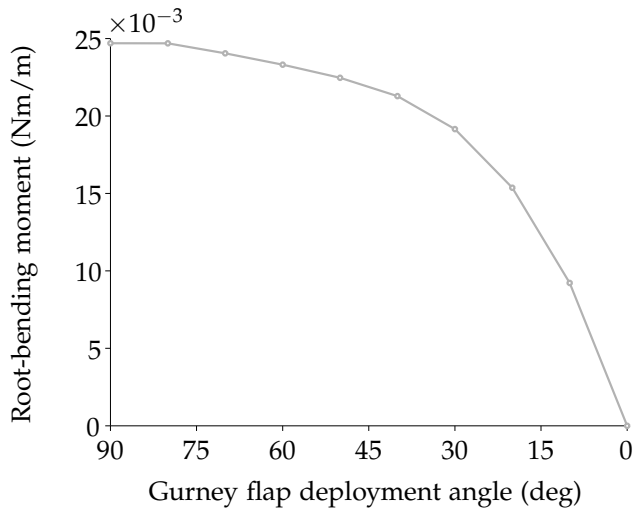


Figure 4.20: Root-bending moment of the Gurney flap for the aerofoil at 10° of angle of attack at Mach 0.6, $Re = 1.14 \times 10^6$.

the moment at the Gurney flap root have been determined for the case of a reverse deployment configuration. The data obtained is utilised to determine the mechanical work required for a mechanism to move the Gurney flap from the deployed to the folded position. The simulations performed in this chapter provide indispensable data for the investigation of actuation mechanisms for the deployment and folding of the Gurney flap in the following chapters.

Assessing the external forces is a requirement for designing an actuation system. It constitutes a necessary milestone to the actuator selection presented in Chapter 2. In the following chapter, the actuator resulting from the selection process is integrated inside a design procedure to amplify its motion into a displacement at the location of the Gurney flap.

Actuation mechanism: design and optimisation

5.1 Introduction

The force applied by the airflow on a Gurney flap has been determined in the previous chapter. The next step is to select an actuation technology and mechanism to bring the required mechanical work for the motion of the Gurney flap (section 4.4.2) at the trailing edge. This chapter investigates the deployment strategies with the Gurney flap and their difference in requirement for an actuation technology. A suitable actuation technology is matched to each deployment strategy using the selection process laid out in Chapter 2. An amplification mechanism is then required to amplify the actuation and bring motion close to the trailing edge of the profile. Designing an amplification structure is a complex process and many approaches can be used [136, 137, 138, 139]. In order to obtain a high quality, high performance amplification mechanism, a two-step design process is proposed. The first step studies the rotor blade profile to establish bounds for a simplified topology. Designs are then generated based on these considerations and selected according to their performance. This first step determines a suitable topology for the amplification mechanism. The second step consists of optimising the geometrical parameters of the selected topology within a set of bounds close to the case studied here: an 81 mm NACA 0012 profile.

This staggered approach is following the recommendations from Pahl et al. [138] to efficiently conduct a design optimisation. The limitation of the approach chosen is the amount of geometrical parameters that can be considered for the optimisation. The objective is to obtain an adequate geometry that will be refined in subsequent

chapters. Therefore, considerations such as hinges or the exact motion required for deploying and folding the Gurney flap are not taken into account here, but in the next step of the design process as reported in the following chapter.

5.2 Actuation selection and principle

5.2.1 Control strategies

Various control strategies are envisioned for the Gurney flap to improve the flight performance of helicopters as mentioned in Chapter 1. Three control strategies are considered with a specific actuation profile to enhance specific characteristics of a rotorcraft in flight. A slow actuation of the Gurney flap boosts the lift of the overall blade, a fast actuation on the retreating side increases the flight envelope and a harmonic actuation can damp undesired vibrations and noise if properly tuned.

Dual-speed blade

The flap can be deployed to provide a significant lift increase in specific flight phases during a rotorcraft mission such as take-off, landing or hovering. During these critical flight phases, the blade is providing more lift with a deployed Gurney flap which allows a reduction of the rotor speed. This brings the additional benefit of reducing the noise of the helicopter and its burden in urban environments. This control strategy does not require a fast actuation to be performed and the deployment can take many rotations to be completed as shown in Figure 5.1.

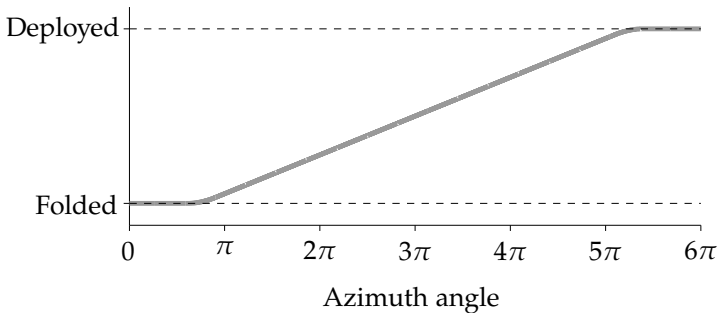


Figure 5.1: Indicative actuation profile for a dual-speed blade.

Active lift control

In this control scheme, the Gurney flap is used as a way of improving the lift and the stall behaviour on the retreating side of the helicopter. The Gurney flap increases the maximum lift and the maximum angle of attack the blade profile can achieve,

enhancing the efficiency of the helicopter and its maximum speed as detailed in section 1.1. To achieve this control strategy, the Gurney flap needs to be deployed within approximately 10° to 20° of blade rotation on the retreating side. Such a control strategy is very demanding for an actuation system because the deployment has to be completed within a short time. The actuation profile is close to a step input as shown in Figure 5.2.

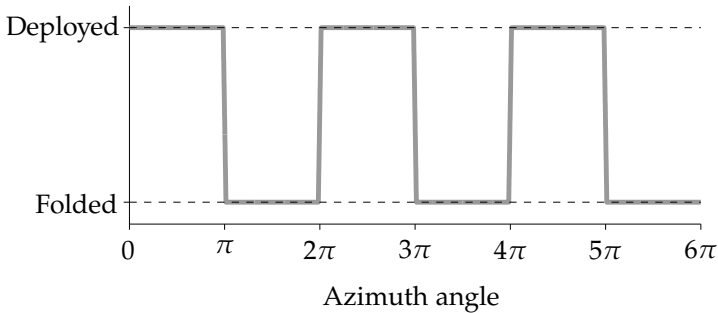


Figure 5.2: Indicative actuation profile for active lift control.

Active vibration control

As revealed in the introductory chapter, harmonic deployment of the Gurney flap can actively damp undesired vibrations of the helicopter rotor system. Typically, the Gurney flap is deployed 4 times per blade revolution, following a harmonic profile as shown in Figure 5.3. Here the constraints on the mechanism are less pronounced due to the smooth deployment profile. Nevertheless, the amount of cycles required requires a very reliable mechanism with a very low failure rate as mentioned in section 1.3.3.

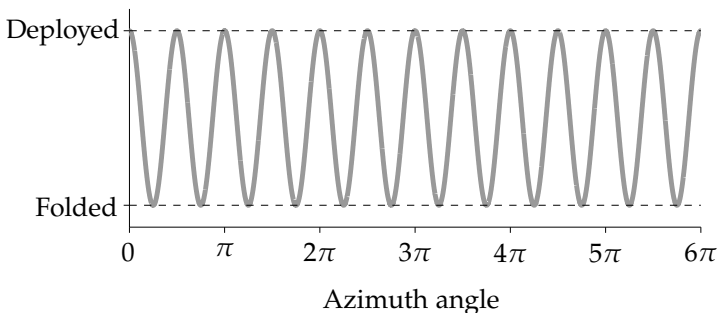


Figure 5.3: Indicative actuation profile for active vibration control.

5.2.2 Deployment duration

The main constraint for choosing an actuation technology for the Gurney flap is the duration of the deployment. The actuator database presented in section 2.5 allows choosing the most efficient actuator technology depending on the deployment time. Table 5.1 shows the deployment duration requirement for the Mach-scaled model blade and the most efficient actuator technology.

Table 5.1: Deployment duration requirement for the Gurney flap on the Mach-scaled model blade for the control strategies considered.

Control strategy	Deployment duration	Actuation technology
Dual speed	~ 1 s	Ultrasonic actuator
Lift control	1 ms	d_{33} actuators
Vibration control (4/rev)	4 ms	d_{33} actuators


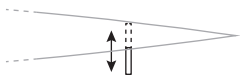


The active lift control requires the smallest deployment duration because of the deployment constraint to happen within 10° of sweeping angle. Active lift control has been chosen by the European CleanSky – GRC joint technology initiative for its potential improvement in rotorcraft efficiency and maximum speed [127]. An actuation system for the model blade should therefore be able to deploy within 1 ms to provide a relevant comparison with the full-scale blade. This is the most difficult condition to meet. A suitable deployment solution for lift control therefore satisfies the deployment requirement for the two other control strategies mentioned.

5.2.3 Gurney flap deployment

Many deployment strategies can be imagined to deploy the Gurney flap as closely as possible to the trailing edge or to avoid moving the flap against the flow. The most common deployment strategy is a vertical deployment as close as possible to the trailing edge [56, 140, 141, 142]. Although this deployment mechanism limits the constraints from the flow, the deployment cannot be achieved at the trailing edge because of the small space available in the profile. Four deployment configurations are considered: deployment like a conventional flap, vertical deployment, sliding deployment and reverse deployment. Their advantages and disadvantages are listed in Table 5.2.

The sliding deployment and reverse deployment configurations are the most favourable deployment concepts. A sliding deployment mechanism requires railings to guide the flap along a path that combines translation and rotation motions. Such a system is feasible for large scale structures but is undesirable at the model blade scale because of the additional complexity of designing such a railing system. Therefore, the reverse deployment configuration is selected because of its optimal placement and the simplicity of the flap motion.

Table 5.2: Main deployment configurations for the Gurney flap.

Configuration	Advantages	Disadvantages
 <p><i>Flap deployment</i></p>	Flap at the trailing edge Folding with the flow	Chord length modification Deployment against the flow
 <p><i>Vertical deployment</i></p>	Limited flow constraints Simple motion	Not at the trailing edge Length limited
 <p><i>Sliding deployment</i></p>	Flap at the trailing edge Limited flow constraints	Complex motion
 <p><i>Reverse deployment</i></p>	Flap at the trailing edge Deployment with the flow	Folding against the flow

5.2.4 Actuation technologies

Piezoelectric stack and patch actuators are the two main types of geometries available for d_{33} actuators as shown in section 2.2.2. The stack actuator provides a concentrated load while the patch actuator delivers a distributed strain. This difference makes the patch actuator more desirable when integration is a key factor. Bonding the patch actuator to a flexible beam provides a straightforward solution to transfer the load generated and convert it to the desired motion. Such a structure is typically called a "unimorph" actuator if one active layer is on the top of the structural layer and a "bimorph" actuator if the structural part is between two active layers [143, 144, 145]. On the contrary, stack actuators require a large deformable structure as mentioned in Chapter 2 or have to be linked to a lever arm for amplification [146, 147, 148, 149].

5.3 Geometrical investigation

The first step taken for the design of a flexible beam-based amplification mechanism is a design study using generated solutions from a computer script. For such a

method to work, the design complexity is kept to a minimum and the script is limited by many rules [137]. The solutions are selected based on the structure deformation when a load is applied.

5.3.1 Structural and spatial considerations

The entire actuation system that comprises of patch actuators and an amplification structure is considered as a two-dimensional structure in the plane of the profile section. Such a geometry has a very large stiffness in the direction of the blade span, ensuring that the centrifugal loads do not affect the motion of the mechanism in the profile section plane.

A typical rotor blade is shown in Figure 5.4. The D-spar at the front of the profile provides the blade with enough strength to sustain the centrifugal loads. The back of the profile is filled with honeycomb core to provide rigidity to the blade.

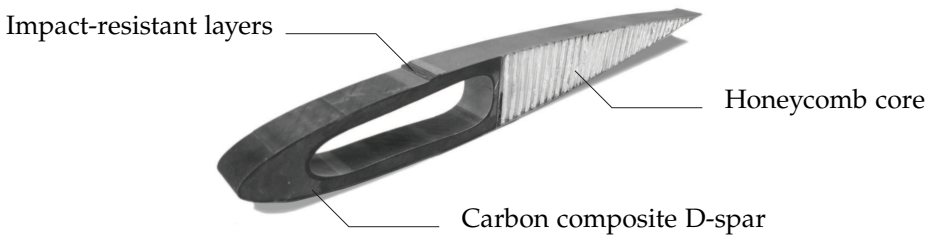


Figure 5.4: Picture of a typical helicopter blade section [150].

A suitable amplification mechanism must bring mechanical work close to the trailing edge while minimising its impact on the existing structure of the rotor blade. The solution chosen is to enclose the mechanism behind the D-spar in place of the honeycomb core which does not contribute to the strength of the rotor blade. The D-spar is utilised as a fixed component to attach the flexible beam mechanism to. Although being crucial parameters, the weight of the structure and its distribution are not taken into account because the choice of patch actuators and flexible beams is much lighter than conventional actuation systems. The weight of the final mechanism has a negligible impact on the blade and is documented in Chapter 6.

5.3.2 Computer generated truss designs

The generation of designs is the first step of the staggered approach considered. A study of the domain boundaries is necessary in order to come up with relevant

designs. This generic approach is appropriate for the complexity of the problem and provides a good starting point for the second part of the process.

Domain bounds and performance criterion

The design domain set for the generation of structures is a rectangle with a fixed boundary corresponding to a D-spar attachment. Considering the space available at the end of the model blade profile as shown in Figures 5.5 and 5.6, a horizontal displacement is selected as a performance criterion for the amplification mechanism. Moving in the direction of the profile chord allows providing larger displacement at the trailing edge and therefore potentially larger mechanical work.

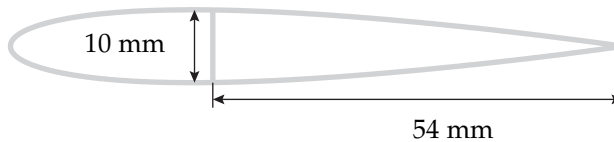


Figure 5.5: Sketch of the NACA 0012 profile at scale.

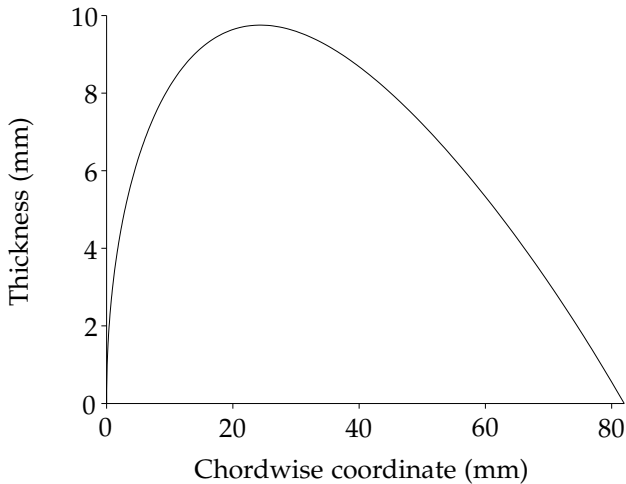


Figure 5.6: Thickness of the NACA 0012 profile for the model blade.

The choice of a horizontal displacement is compatible with the reverse deployment configuration selected. Applying a horizontal motion to a connection along the flap length results in a rotation of the flap as displayed in Figure 5.7.

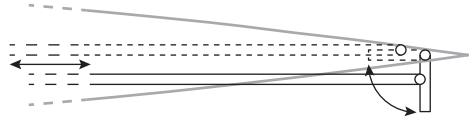


Figure 5.7: Conceptual design of the connection between a mechanism developing a motion in the chord direction to the Gurney flap for the reverse deployment configuration.

Design generation and evaluation

A computer program generates potential structures based on the bounds selected previously. The structures consist of nodes arranged in a square array connected by truss elements as shown in Figure 5.8. The main constraint is that the two nodes representing the D-spar are fixed. The aim is to find a flexible structure connecting the D-spar with the lower right node. A horizontal load is applied on the lower right node and the horizontal displacement of the structure is calculated through a linear system of equations [151]. For a design space consisting of 8 nodes, 9202 unique structures are generated and analysed. Each structure corresponds to a random set of connections between nodes that satisfy the constraints. The best structure configuration is displayed in Figure 5.8.

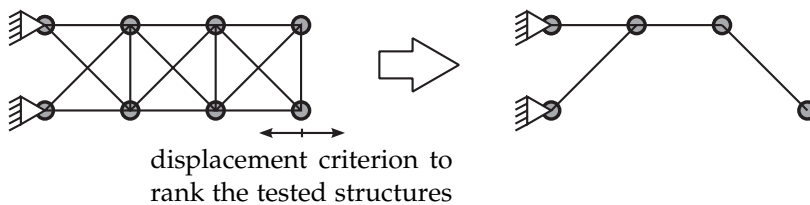


Figure 5.8: Domain considered for generating designs and resulting structure design.

Increasing the number of nodes was considered and led to similar geometries. It appeared that 8 nodes were sufficient to provide enough variety in the topology of the generated structures. The structure selected is a good starting point for the optimisation because of its simple topology. Therefore, only a limited number of geometrical parameters are required to optimise this structure.

5.4 Geometry optimisation

The structure obtained can be used directly to provide amplification to a piezoelectric patch. However, the structure would not provide an optimal performance in this problem because the exact dimensions of the blade profile have not been applied and the truss model is too simple to model the strain of a patch actuator. The topology of the structure obtained serves as the basis for a parametrized structure. In addition, spatial constraints on the structure are added to get closer to a mechanism that can fit inside the model rotor blade profile. Three geometrical parameters are selected for optimisation to find the structure that delivers the best performances within the model blade profile.

5.4.1 Parametrized FEM analysis

The truss structure is scaled to fit inside the constrained space of the NACA 0012 model blade as shown in Figure 5.9. The nodes connected to the D-spar geometry correspond to a clamping boundary condition for the root of the upper arm. An active piezoelectric element is added on the upper part of the geometry and modelled using fully coupled piezoelectric elements within the Comsol Multiphysics Finite Element package. A sliding boundary condition is applied to the bottom arm to simulate the contact with the bottom surface of the profile. The geometry is fully parametrized using polynomial functions to follow the curvature inside the profile and to use as much space as possible. The number of variables to generate a geometry is limited to three as shown in Figure 5.9:

- the length of the top arm (a),
- the length of the bottom arm (b),
- the curvature of the middle arm (c).

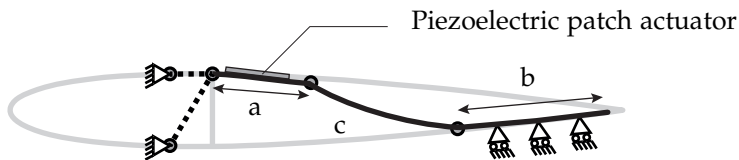


Figure 5.9: Parametrized structure with the three variables chosen for the optimisation.

Controlling the length of both the top and bottom arms enables the generation of many configurations with a large variety of angles for the middle part. The curvature variable (c) controls the load transfer between the top and bottom

arms. The length of the piezoelectric element depends on the length of the supporting arm. The Comsol multiphysics piezoelectric module is used to model the piezoelectric component. The piezoelectric properties are set to the d_{33} patch actuator from PI as determined in Chapter 3. For the structure, the Young's modulus, Poisson's ratio and density of the carbon/PPS composite tested in Chapter 3 are used. The model uses a plane-strain approximation because of the extension of the actuation system along the blade axis. The meshing of the structure and the piezoelectric layer follows a size parameter defined by the thickness of the piezoelectric layer to ensure that a fine mesh is produced for any combination of parameters. Triangular quadratic elements are used to capture the strains transferred by the piezoelectric patch to the structure correctly.

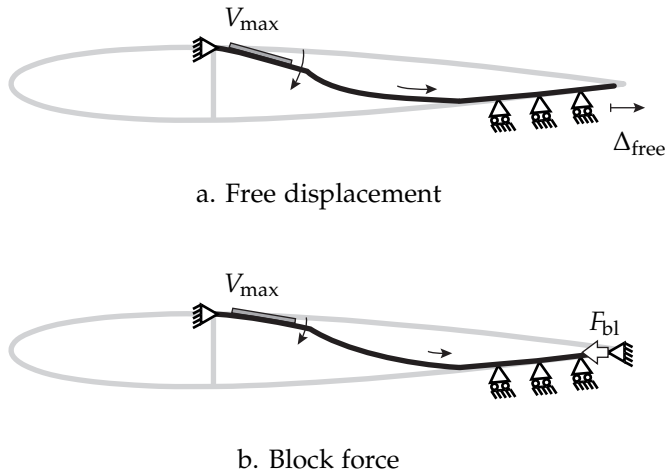


Figure 5.10: Characteristics extracted from the flexible actuation system.

The displacement at the end on the bottom arm is retrieved when the maximum voltage ($V_{\max} = 130 \text{ V}$) is applied on the piezoelectric patch actuator as shown in Figure 5.10.a. This value is the free displacement of the full actuation mechanism because the lower arm of the structure is free to move in the motion direction. The block force of the system is extracted by clamping the lower arm end and calculating the resulting reaction force as shown in Figure 5.10.b.

5.4.2 Surrogate optimisation

An optimisation procedure is set up to select the best combination of geometrical parameters for maximising the performance of the actuation system. This constitutes the second step of the design approach followed in this chapter.

The optimisation procedure

The parametrized FEM is embedded inside a surrogate optimisation scheme as shown in Figure 5.11. The surrogate optimisation was chosen for its flexibility and the small number of simulations it requires to approach the optimum [152, 153]. It consists of the determination of a surrogate function, which is used to estimate the objective function maximum over the design space. A number of simulations need to be computed prior to the optimisation itself to provide the first surrogate function. Once the surrogate function is calculated, the optimum of the estimated objective is determined using a combination of global and local search algorithms. A simulation is performed at the location of the optimum to verify that the surrogate represents the system response correctly. The error is defined as the relative difference of the objective estimation compared to the system response at the location of the optimum. In order to refine the estimation of the objective and thus the determination of the optimum, the simulation used for the error calculation is added to the set of simulations done to calculate a new surrogate function. The optimum of the updated function is determined and a new simulation is performed to retrieve the error. The loop described is performed until the error is below a threshold, meaning the optimum of the surrogate is the optimum of the system.

The objective function

The performance of the actuation system is a combination of both displacement and force. Amplifying the displacement of a patch actuator leads to a decrease in the block force. The aim of the optimisation is to maximise the free displacement while keeping the block force as large as possible. The objective function takes into account both characteristics of the system and scales them according to the performance of the piezoelectric patch without the structure:

$$y = \sqrt{\left(\frac{\Delta_{\text{free}}}{\Delta_{\text{free}}^{\text{pzt}}}\right)^2 + \left(\frac{F_{\text{bl}}}{F_{\text{bl}}^{\text{pzt}}}\right)^2} \quad (5.1)$$

where Δ_{free} and $\Delta_{\text{free}}^{\text{pzt}}$ are the free displacement of the actuation mechanism and the free displacement of the patch actuator respectively and F_{bl} and $F_{\text{bl}}^{\text{pzt}}$ are the block force of the actuation mechanism and the block force of the piezoelectric actuator respectively. The objective function is, in this case, a dimensionless number corresponding to a normalised amplification of the actuation mechanism in both force and displacement. It gives an indication of the amount of work that can be delivered. The displacement and the force are in fact two competing sub-objectives. This shows the need for an optimisation to find a suitable balance. An improvement of the objective function means one characteristic is increasing faster than the other one is decreasing, making the improved mechanism more efficient.

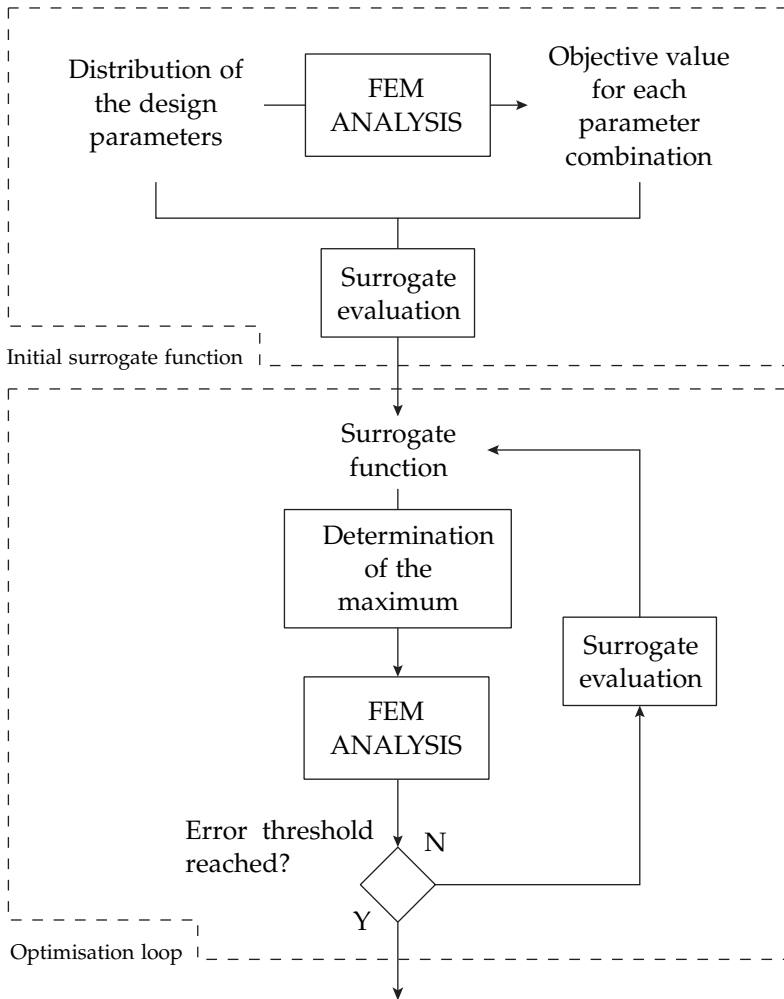


Figure 5.11: Flow chart detailing the optimisation scheme.

The surrogate function

An ordinary Kriging model provides an accurate estimation of a function over a distributed sample of points [154, 155, 156]. It is used as the surrogate function to estimate the objective. A Kriging model consists of a base function which represents the global trend of the data with a stochastic function that approaches the data at the sampling points:

$$\hat{y}(x) = \eta + \zeta(x) \quad (5.2)$$

$$x = \begin{pmatrix} a \\ b \\ c \end{pmatrix} \quad (5.3)$$

where $\hat{y}(x)$ is the estimation of the surrogate function for a vector of parameters x , η is a constant value corresponding to the base function of the ordinary Kriging model and $\zeta(x)$ is the function which estimates data modelled at the sampling points. The surrogate function evaluates the objective value for a set of design parameters. More details concerning the Kriging function are presented in Appendix B.

Evaluating the surrogate function

In order to determine the surrogate function before searching for its maximum, a first set of simulations is required to sample the design space. Thirty initial simulations are performed with a distribution of the design variables. A Latin hypercube distribution is chosen to cover the design space. Such a distribution ensures that variables are sampled evenly in a space of arbitrary dimension [157, 158].

Extremum search and exit criterion

Two approaches are used to find the maximum of the surrogate function. First a genetic algorithm searches the design space for a global maximum which is then refined by a gradient-based search. The use of both techniques improves the chances that a global extremum is found for the surrogate function. The simulation is looped until the error of the estimation of the objective function by the surrogate at the maximum relative to the value obtained by a simulation at the evaluated maximum falls below 0.05%.

5.5 Optimisation results & discussion

Once the surrogate function has been evaluated, the optimisation reaches the exit criterion within 13 iterations as shown in Figure 5.12. The use of a genetic algorithm explains the large jump in the convergence curve at the 7th iteration. A genetic algorithm allows the exploration of the domain and can escape a local extremum found previously by the system.

5.5.1 Optimised geometry

The resulting mechanism presents the flexible arms arranged in a z-shaped configuration as shown in Figure 5.13. The top arm, onto which the piezoelectric

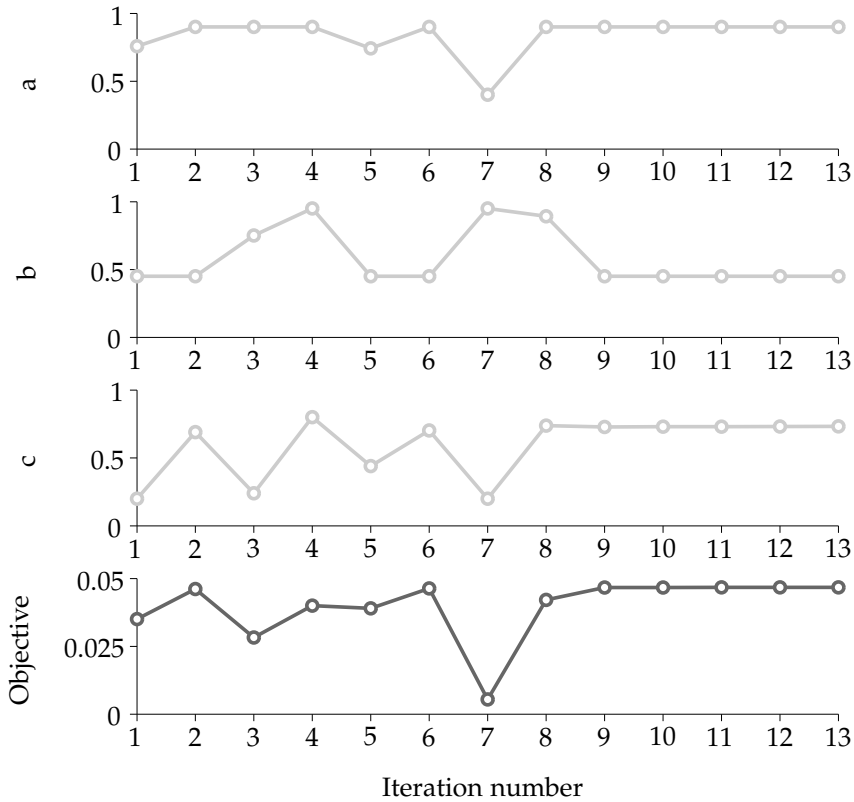


Figure 5.12: Convergence of the optimisation loop for the design parameter and the value of the objective function. *a*, *b* and *c* are expressed as dimensionless numbers.

actuator is bonded, bends when a voltage is applied. The resulting motion at the tip of the top arm is converted into a horizontal motion by the middle arm as shown in Figure 5.14. The direction of the motion of the optimised structure is in the opposite direction to the trailing edge, contrary to the structure displayed in Figure 5.9. The inversion of the motion direction is possible because the objective function detailed in equation 5.1 is based on the absolute value of the displacement and not its direction. The optimisation shows that larger displacements are available when the displacement is towards the leading edge. Setting the constraints of the geometry generation process closer to the geometry of the blade directly results in a geometry with an inversion. Moreover, adding more nodes provides more freedom for generating a potential structure closer to the optimised geometry, but at great expense of computing time. Computer generated geometries cannot directly provide an optimum performance and

should be regarded as a tool for providing an initial design. A fine model and a much more complex procedure are required to end up with an optimised structure such as the z-shaped geometry.



Figure 5.13: Resulting mechanism after the surrogate optimisation.

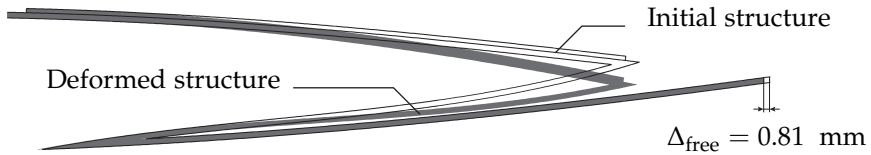


Figure 5.14: Deformation of the structure during actuation.

5.5.2 Performance of the optimised mechanism

The performance of the optimised profile is characterised by a free displacement of 0.81 mm and a block force of 185 N per metre of wingspan. These values correspond to the maximum capabilities of the system. Its characteristic curve is needed to obtain the equilibrium points during operation. The characteristic curve of the actuation system represents all combinations of displacements and forces that can be reached by the mechanism as detailed in Chapter 2. It is obtained by adding an extra load component in the direction of the motion and retrieving displacements and forces. Similar to the actuators presented in Chapter 2, the actuation system exhibits a linear relation between force and displacement as shown in Figure 5.15.

The area under the characteristic curve represents the total mechanical energy that can be delivered by the system. In practice, the mechanical work delivered depends on the load path taken by the actuation system attached to the Gurney flap. The mechanical work required to fold the Gurney flap has been estimated to be 30 mJ/m in Chapter 4. The area under the characteristic curve gives 75 mJ/m. Therefore the amplification mechanism should be capable of folding the Gurney flap under aerodynamic loading if a feasible load path is followed.

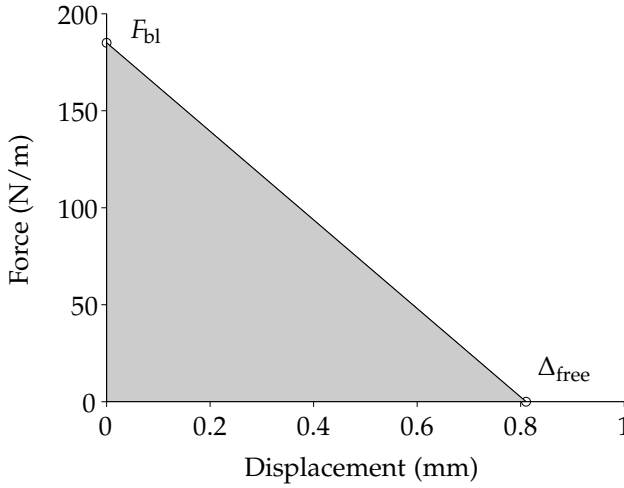


Figure 5.15: Characteristic curve of the actuation system.

5.5.3 Load path

The load path depends on the lever arm between the connection to the Gurney flap and the hinge at the Gurney flap root. If the connection is close to the root of the flap, a small horizontal displacement is required from the mechanism for folding the Gurney flap while a large force is needed as shown in Figure 5.16. On the contrary, having the connection further away from the root of the flap requires more displacement but less force.

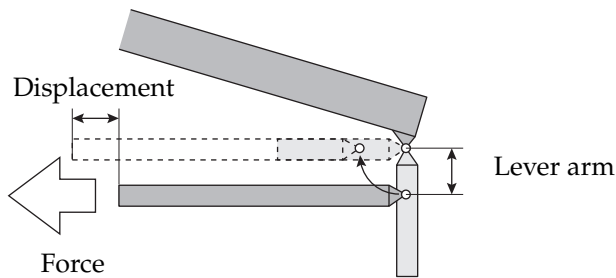


Figure 5.16: Sketch of a direct connection between the actuation mechanism and the Gurney flap.

A load path can be calculated for each lever arm length, resulting in a range of possible arm lengths for connecting the actuation system to the Gurney flap as shown in Figure 5.17. It is to be noted that the area under each work path is

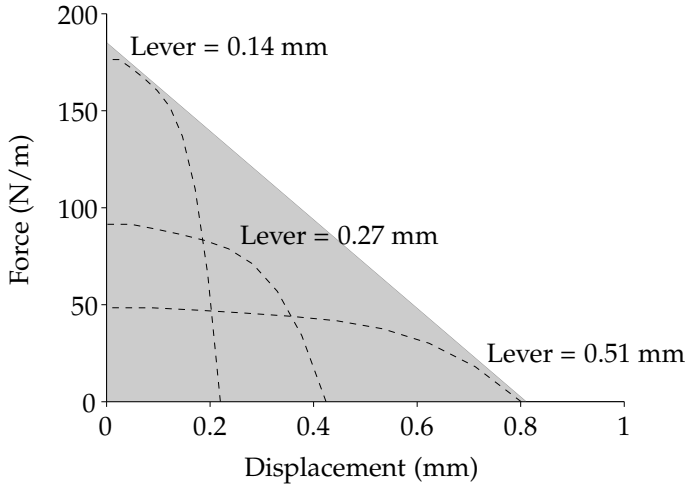


Figure 5.17: Work path for various lengths of lever arm. If the work path gets outside of the area delimited by the characteristic curve, the motion is not feasible by the mechanism.

30 mJ/m because the total work to fold the Gurney flap is not modified by the path taken. The range of possible lever arm lengths is investigated by searching for the intersection of the work path with the characteristic curve. The result gives a lever arm dimension between 0.14 mm and 0.51 mm.

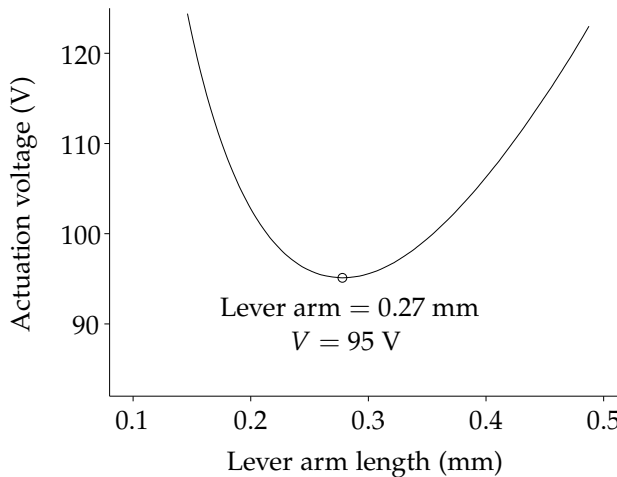


Figure 5.18: Graph of the actuation voltage required for deploying the Gurney flap as a function of the lever arm length.

A good choice for the lever arm is to take the dimension that allows the motion to be completed with the smallest actuation voltage possible. Figure 5.18 shows that the actuation voltage to fold the Gurney flap goes through a minimum corresponding to a lever arm length of 0.27 mm. Lowering the actuation voltage decreases the free displacement and block force and thus the capabilities of the actuation system as shown in Figure 5.19. However, it ensures that the actuation system is capable of delivering extra force and displacement in the event of unexpected constraints.

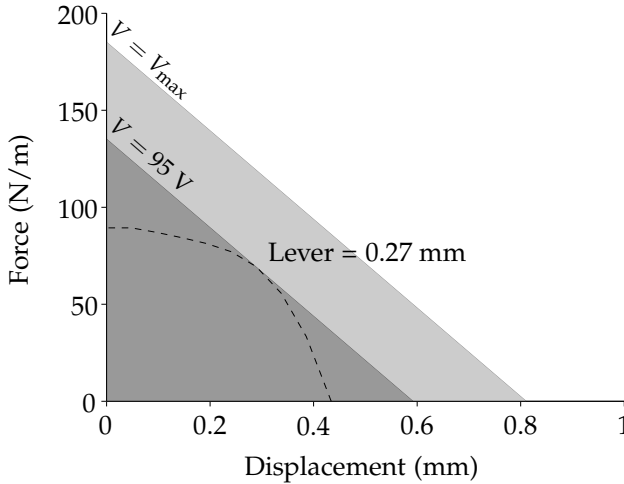


Figure 5.19: Characteristic curves for $V = V_{\max} = 130 \text{ V}$, $V = 95 \text{ V}$ and load path corresponding to a lever arm length of 0.27 mm.

5.6 Conclusion

The design process proposed in this chapter involves the determination of a simplified structure and its optimisation using a surrogate optimisation scheme. The approach of generating designs to give a starting point for a complex optimisation can be applied to any design under tight and conflicting constraints. The key is setting the right objectives and constraints at each stage of the process. The resulting structure offers an original geometry to amplify the piezoelectric constraints with an inversion that appeared during the optimisation process. The quasi-static analysis of the structure showed suitable performance when connecting the Gurney flap to the actuation mechanism. The reverse deployment configuration for the Gurney flap is especially suited to the actuation of the mechanism in that direction. Large forces are available from the actuation system when the Gurney flap is deployed to counteract the aerodynamic force. During the

folding motion, the aerodynamic constraints are decreasing along with the force available by the actuation mechanism while providing the displacement necessary to fully fold the flap.

Designing an integrated actuation system is a complex process because of the many coupled decisions to take: actuator selection, means of amplification, structural components and load transfer. Selecting an actuator is the critical part that allows design processes to be put in place in order to move forward. The following chapter focusses on refining aspects of the geometry that could not reasonably be considered in the geometric optimisation.

Refinement of the deployment mechanism

6.1 Introduction

Designing an efficient product is a lengthy and complex process. Optimisation routines and computer generated designs serve as tools in the course of that process. In the previous chapter a conceptual design of the flexible mechanism and its connection with the Gurney flap was presented. The aim of this chapter is to build upon the conceptual design and present a realistic mechanism considering details that are too complex to be included in an optimisation scheme. The material deformation is investigated to refine the connections between the components and flexible hinges are proposed to make the z-shaped design feasible. The FEM model used to investigate the design is also made more accurate. Finally, the folding motion of the Gurney flap is studied to achieve the desired rotation.

Flexible hinges consist of one piece of material that is made thinner at one location to be used as a flexural hinge as shown in Figure 6.1 [159, 160, 161]. The advantage of such a construction over a conventional hinge is the absence of discrete mechanical components such as ball bearings, rods and connections, meaning there is neither friction nor play. The resulting component can be durable, reliable and possesses a large transverse stiffness. Moreover, flexible hinges allow the force on the hinges to be distributed along the full length of the hinge. The rotational angle of this component depends on the yield strength and the fatigue limit of the material considered. The material specifications determine the thickness of the joint and rotational amplitude for a safe operation over a large number of cycles. Typically, polymers and metals are used to make flexible

joints [161, 162, 163, 164]. Polymer flexible hinges are widely used in consumer products for making plastic boxes with a lid integrated in one piece [162]. For such a product, the rotational angles are very large. Plastic flexible hinges are also available for making the hinge of control surfaces for model airplanes as shown in Figure 6.2. Metallic flexible hinges are used in precision engineering for small displacement mechanisms [163, 165, 166]. In these applications, the rotational amplitude of the hinges is typically small.

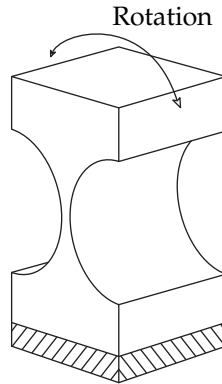
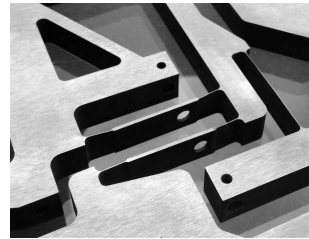


Figure 6.1: Sketch of a circular flexible hinge.



a. Plastic hinges used in radio-controlled model airplanes [167].



b. Metal hinges as flexible parts of a micro-mechanical mechanism (courtesy of the Automation and Control chair at the University of Twente).

Figure 6.2: Examples of flexible hinges.

The refinement of the hinges for the mechanism is carried out on the optimised structure from Chapter 5. Using flexible hinges to replace connections between beams changes the mechanism flexibility and modifies the amount of displacement

and block force available. Verification is therefore done to check if the modifications are not reducing the mechanism performance below requirements. Flexible hinges are also investigated for the reverse deployment configuration of the Gurney flap. However, much smaller hinges need to be considered due to the larger rotational angles.

6.2 Refinement of the flexible mechanism

Two important refinements are presented: the implementation of flexible hinges in the mechanism and the addition of a contact model to take into account the top part of the blade profile skin. Both refinements are important to accurately reflect reality.

6.2.1 Flexible hinges for the bending arms

Flexible joints are implemented in the design by removing material around the connection of the beams, where stress concentrations are predicted as shown in Figure 6.3.

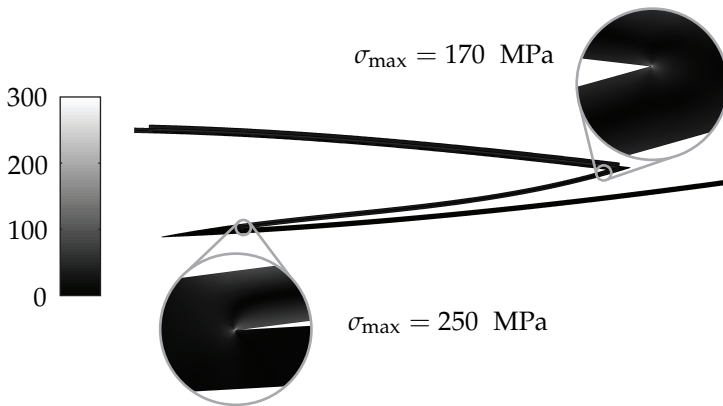


Figure 6.3: Stress state in the optimised z-shaped mechanism. The location of the stress concentrations are highlighted.

As mentioned in the previous section, steel or polymer materials are typically used to manufacture flexible joints. The stresses in the material determine the thickness of the joint. A joint with a thick section leads to larger stress compared to a joint with a thinner section for the same rotation angle. The maximum stresses of circular joints made of steel and polypropylene are investigated with a Finite Element Model for the deformations observed in the z-shaped structure. Figure 6.4

shows the peak stress in the material for a circular flexible hinge of thickness h under a rotation of 5° , corresponding to the maximum rotational angle between the arms of the z-shaped mechanism. Typical properties for polypropylene and steel are shown in Table 6.1.

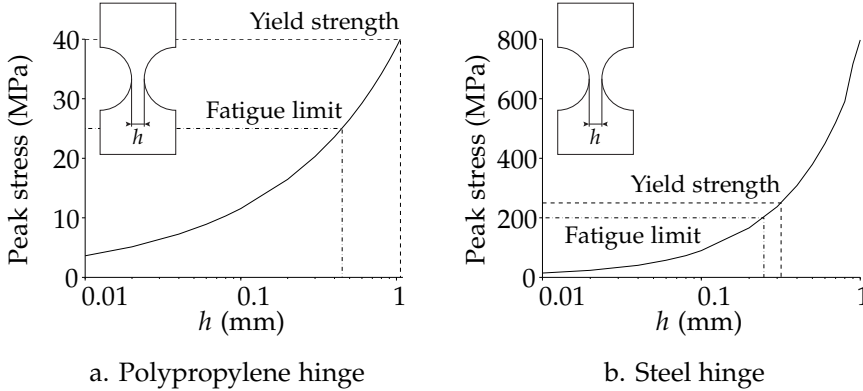


Figure 6.4: Maximum longitudinal stress in a circular flexible hinge under a 5° rotation for various values of the hinge thickness (h). The dashed line (---) and the dash-dot line (-.-) respectively mark the yield strength and the fatigue limit of each material.

Table 6.1: Properties of A36 Steel and polypropylene produced by injection molding [168]. The fatigue limit corresponds to 10^5 cycles and is an average value typically found in the literature at room temperature [169, 170, 171].

Property	A36 Steel	Polypropylene
Young's modulus	200 GPa	1.5 GPa
Ultimate strength	400 MPa	80 MPa
Yield strength	250 MPa	40 MPa
Fatigue limit	200 MPa	25 MPa

The ratio of yield strength over Young's modulus for polypropylene allows thicker joints to be made compared to steel as shown in Figure 6.4. The beams of the z-shaped mechanism are connected with flexible joints made of polypropylene. Considering the deformation of the joints and the analysis performed, the thickness chosen is 0.08 mm. This corresponds to a peak stress of 10 MPa, thus smaller than half the fatigue limit of material. The main issue with a polymeric joint is the temperature range. Polypropylene properties will vary significantly with the temperature [164]. This is a concern for a full-scale mechanism. However, the effect of the temperature will be limited for a model blade tested in a controlled

environment. The connection between the beams of the z-shaped geometry is modified to include flexure joints as shown in Figure 6.5.

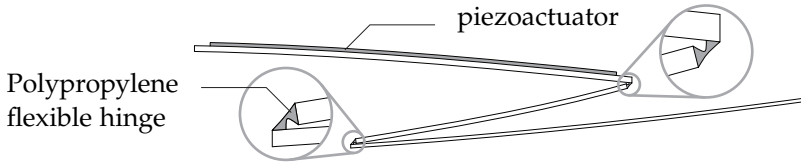


Figure 6.5: Geometry of the z-shaped structure including flexible hinges at the beam connections.

The manufacturing of polypropylene flexure joints is typically done by injection molding the polypropylene and then by quickly folding the hinge back and forth while the material temperature is still above the glass transition temperature [161, 164]. This aligns the polymer chains across the hinge providing a large strength and excellent fatigue properties [161, 164]. Figure 6.6 shows a possible manufacturing setup for the hinge. The two beams are manufactured with a notch to ensure a strong connection between the beams and the hinge. A mold encases the two beams and provides the shape for the flexure joint. The melted polypropylene flows inside the remaining space, filling the notch of each beam. Adhesion between polypropylene and the composite beams can be improved by using layers of polypropylene composite in the layup for manufacturing the beams. The hinges are subjected to a complex combination of axial and shear loads, thus additional analyses are needed for the exact implementation.

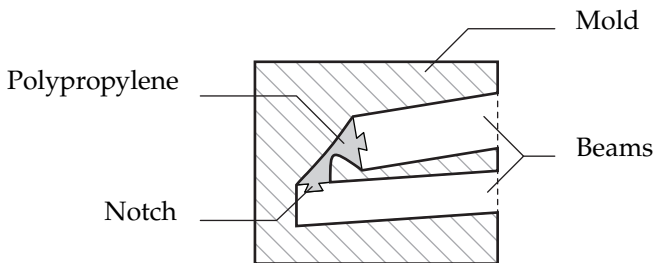


Figure 6.6: Sketch of a setup for manufacturing a flexure hinge connecting two beams for the z-shaped mechanism.

6.2.2 Modelling the contact on the profile skin

The z-shaped mechanism is evaluated with the FEM model detailed in Chapter 5. In order to have relevant results from the simulation, the model must remain accurate.

During the actuation of the mechanism, the mechanism comes into contact with the inner surface of the blade profile. However, the contact between the top arm and the profile depends on the load case: when the loads are small, the top part bends down and does not make contact with the profile; for large loads, the top part curves and pushes against the profile. The top profile skin is added to the model by a fixed beam and a penalty contact model is employed. The friction does not need to be taken into account because the two surfaces do not move relative to each other when in contact.

When the top part is in contact with the profile skin, the mechanism displacement is null. The end arm of the mechanism cannot move towards the trailing edge because of this contact. The geometry acts as a stop and prevents the Gurney flap from exceeding its maximum deployment angle. Including the contact also improves the mechanism block force which is detailed in the following section.

The sliding boundary condition set in the previous chapter for the bottom arm and the bottom skin of the profile is maintained because the loads on the mechanism keep these two surfaces in contact. Friction is neglected to simplify the analysis and solutions such as surface treatments and coatings can minimise this problem eventually.

6.2.3 Performance improvements

The refinement of the optimised geometry provides improvements in both the free displacement and the block force. Table 6.2 shows the successive performance improvements on the mechanism after each design iteration. The addition of flexible hinges does not decrease the structural performance. Finally, a significant performance increase is seen by considering a contact model to the upper part of the profile skin.

Table 6.2: Performance improvements of the successive actuation models.

Model	Free displacement	Block force	Max work
Base geometry	0.81 mm	185 N/m	75 mJ/m
Geometry + hinges	0.81 mm	190 N/m	77 mJ/m
Geometry + hinges + contact	0.81 mm	334 N/m	103 mJ/m

In the simulation including the contact model, there is no longer a linear relationship between the displacement and the force. The block force is much larger because the top bending arm pushes against the top of the profile skin. The profile skin provides additional support for the flexible structure over a large range of displacements (beside the block force). This increases the overall force delivered and therefore the work available as shown in Figure 6.7.

Plotting the load path calculated in the previous chapter reveals that a large range of forces and displacements are available to achieve the rotation of the Gurney

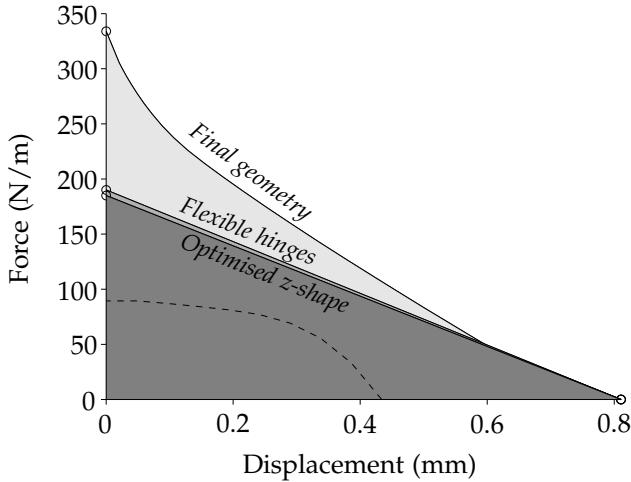


Figure 6.7: Characteristic curve of the flexible mechanism for the successive refinements: the z-shaped base geometry, the z-shaped geometry with flexible hinges and the final geometry with the contact model. The load path determined in Chapter 5 is plotted (— —).

flap. The following section details the design of the connection to the Gurney flap to achieve a full rotation.

6.3 Deploying and folding the Gurney flap

The z-shaped mechanism performs mechanical work at the trailing edge of the profile. The connection to the Gurney flap must convert this motion into a rotation. The conceptual sketches presented in section 5.5.3 cannot allow the Gurney flap to fully fold because the motion of the bottom arm is a translation following the profile bottom skin. In this section, the geometry is adjusted to increase the rotation of the flap while a second actuator is added to provide a circular motion of the bottom arm of the actuation mechanism as shown in Figure 6.8.

6.3.1 Final design of the Gurney flap deployment system

The lever arm length determined in Chapter 5 is used as the dimension between the rotation axis connected to the profile and the rotation axis connected to the arm of the z-shaped mechanism. The geometry of the flap is modified to take advantage of more horizontal mechanical displacement as shown in Figure 6.8.

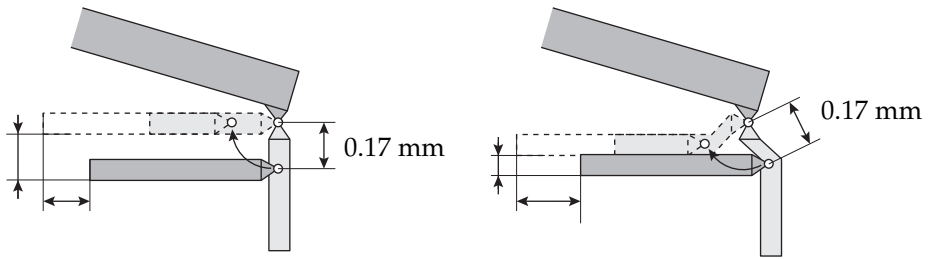


Figure 6.8: The modification of the geometry allows taking advantage of the horizontal motion delivered by the mechanism.

Flexible joints

Flexible joints are also considered for the Gurney flap connection to the profile and the mechanism instead of rotating mechanisms. The rotation angle of the Gurney flap is 90° . However, the angle considered for the flexible hinges is 45° because the joints can be made at an angle and therefore require only $\pm 45^\circ$ of amplitude. Polypropylene is a superior material for making flexible joints as shown earlier in this chapter. A study is performed considering a polypropylene joint under 45° of rotation. The peak stress in this load case is too large to make a realistic joint without exceeding the yield strength or the fatigue limit as shown in Figure 6.9.

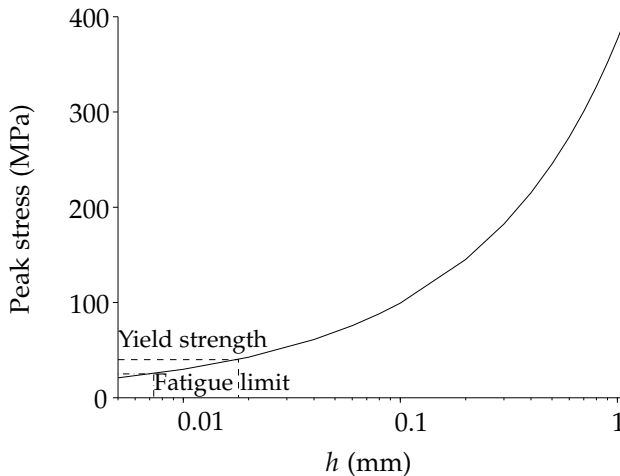


Figure 6.9: Maximum longitudinal stress in a circular flexible hinge under a 45° rotation for various values of the hinge thickness (h). The dashed line (---) and the dash-dot line (-.-) respectively mark the yield strength and the fatigue limit of the material.

To satisfy the fatigue limit condition, the joint should be as thin as $5\ \mu\text{m}$. This is an unrealistic value for manufacturing a hinge. Investigation of the principles behind the characteristics of the polypropylene living hinge provides a partial answer to this problem. The strength of the living hinge lies in the orientation phenomenon happening at the level of the polymer chains in the material. The internal structure of the polymer hinge consists of polymer chains perpendicular to the hinge axis of rotation that provides a large stiffness under tension and a very low bending stiffness as shown in Figure 6.10 [161, 164]. The surrounding area is prone to necking and plastic deformation because of the large strains [164].

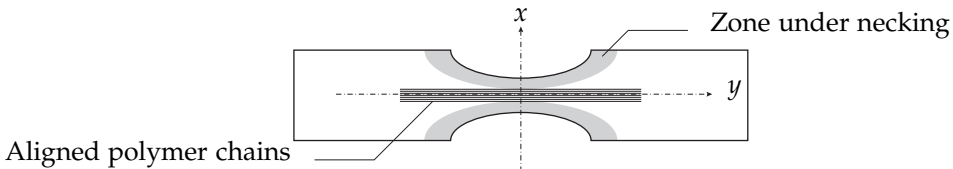


Figure 6.10: Sketch of the internal structure of a polypropylene hinge.

The fact that the material around the hinge is under plastic deformation does not imply that the hinge properties will decrease and will cause a premature failure [161, 164]. Studying the stresses in a 0.08 mm polypropylene joint under 45° rotation reveals that the most important part of the joint is within reasonable limits as shown in Figure 6.11. These results suggest that such a polymer joint may be able to handle repetitive deformations and still be capable of handling the loads for this application. A thorough fatigue study of the joint and its properties needs to be performed to verify its capabilities.

Another approach is the manufacturing of a hinge that combines fibres and a polymer in order to mimic the internal structure of the polypropylene flexible hinge. Hardick B.V. is producing Teflon/Glass composite films that are as thin as 0.06 mm with excellent bending properties [172]. Using a composite allows accurate control of the direction of the fibres and their placement through the hinge and, therefore, allows tuning of the bending stiffness and strength of the hinge.

Such a study goes beyond the purpose of this work and will not be pursued. For modelling the hinge in the Finite Element simulations a 0.04 mm thick flexible hinge is considered and the material properties of polypropylene are applied to the hinge. Although the stresses are exceeding the fatigue limit and yield strength of the material, the behaviour of the hinges is similar to a pin-joint as shown in Figure 6.12.

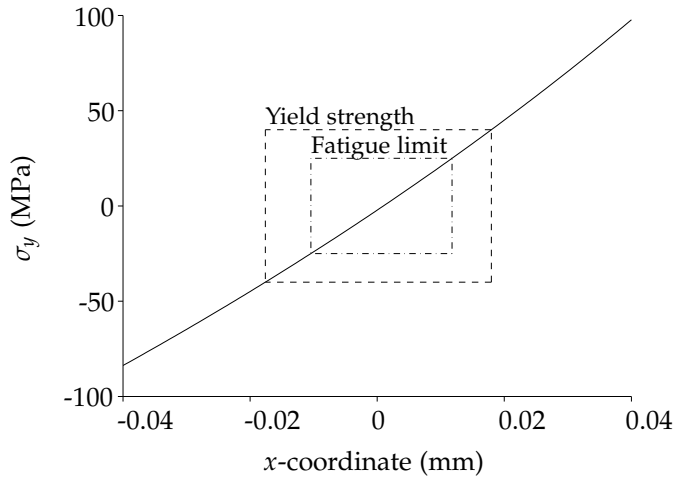


Figure 6.11: Stress across a 0.08 mm thick polypropylene hinge under 45° of rotation. The dashed line (---) and the dash-dot line (-.-.) respectively mark the yield strength and the fatigue limit of the material.

Additional actuator

A FEM simulation of the refined geometry almost completes the rotation of the flap using only the horizontal motion provided by the piezoelectric actuator. Nevertheless, a second actuation system is necessary on the structure to finish the motion and to fully fold the Gurney flap in the profile skin. A 90° rotation is not necessary as an 80° rotation is sufficient to bring the Gurney flap into alignment with the rotor blade profile as shown in Figure 6.12.

The second actuator is bonded on the lower arm as shown in Figure 6.12. Its dimensions are based on the maximum length fitting inside the profile without contact during the deformation of the mechanism (22 mm). The second actuator acts as a pure bender on the bottom arm. This second actuator works in contraction whereas the actuator on the top arm works in extension. Therefore, a negative voltage profile is applied to the additional actuator in order to provide an upward vertical displacement to the tip of the lower arm. Operating the second actuator in contraction means that the strains delivered are lower due to the asymmetric actuation profile of piezoelectric actuators as detailed in Chapter 2. A voltage of -40 V is necessary to fold the Gurney flap. A cheaper d_{31} patch actuator which works primarily in contraction can be considered here. The force requirement is very low on this actuator, the purpose of which is to complete the rotation of the Gurney flap. Its actuation occurs when the Gurney flap is partially folded and the forces are much lower as shown in Chapter 4.

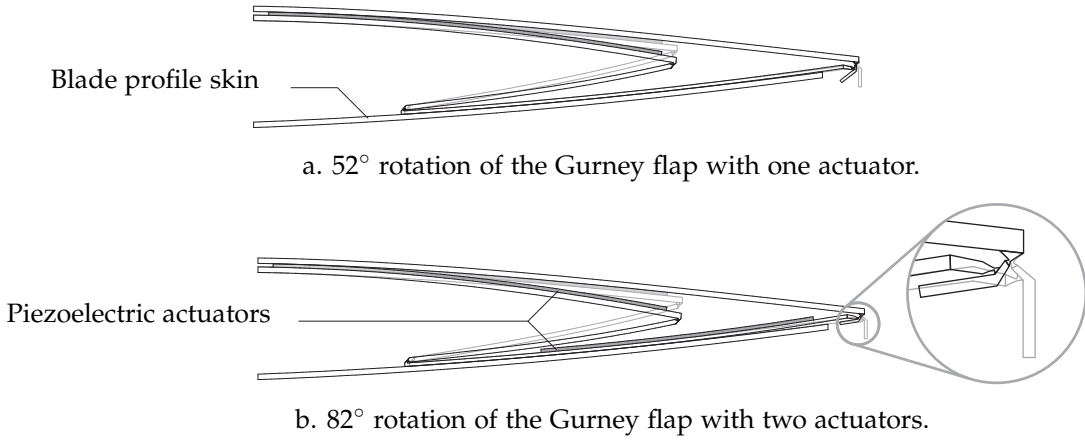


Figure 6.12: Simulation results of the Gurney flap rotation with and without actuator on the lower beam.

Deployment control of the Gurney flap

The second actuator provides enough vertical displacement to allow the connection to the Gurney flap to describe an 80° circle arc around the connection to the profile skin. However, the input voltage of each actuator follows the same step function although only the horizontal motion is required at the start of the displacement. The aim is to drive the piezoelectric actuators such that the flap is deployed within 1 ms and the deployment goes as smoothly as possible. To improve the rotational motion, the input profile sent to the additional actuator (V_2) is set independently from the input of the first actuator (V_1). Both profiles follow an analytical approximation ($\theta(t)$) of the Heaviside step function [106]:

$$\theta(t) = \frac{1}{1 + e^{-2\kappa t}} \quad (6.1)$$

where κ is a parameter that determines how sharp the transition is. κ is arbitrarily set equal to 8 to complete the transition within 1 ms. The voltages directly relate to the position of the flap. The system can be seen as describing a circle using each actuator as a component in a 2D plane. Harmonic functions are therefore used to describe a quarter of a circle taking $\theta(t)$ as the driving function to go from 0 to $\frac{\pi}{2}$. Finally, the driving voltage of the top and bottom actuator (respectively V_1 and V_2) is scaled for each actuator (A_1 and A_2) to obtain the required deformation from each actuator:

$$V_1(t) = A_1 \sin\left(\theta(t) \frac{\pi}{2}\right) \quad (6.2)$$

$$V_2(t) = A_2 \left[\cos\left(\theta(t) \frac{\pi}{2}\right) - 1 \right] \quad (6.3)$$

A_1 is set equal to 95 V as detailed in Chapter 5 and A_2 is set to -40 V. The resulting input functions allows to smoothly apply a driving voltage to each actuator in order to follow a step input function for the Gurney flap deployment angle as shown in Figure 6.13.

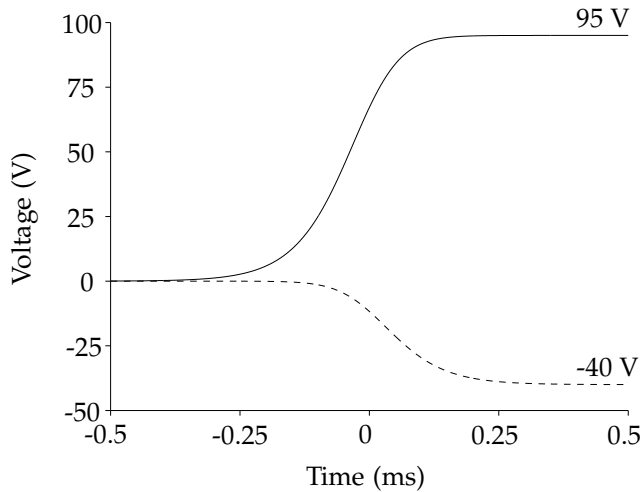


Figure 6.13: Input voltages V_1 (—) and V_2 (- - -) for each actuator controlling the z-shaped mechanism.

A transient analysis of the folding of the Gurney flap reveals that the folding and the deployment are achieved within 1 ms as shown in Figure 6.14. This duration meets the specifications set on the actuation system in Chapter 5.

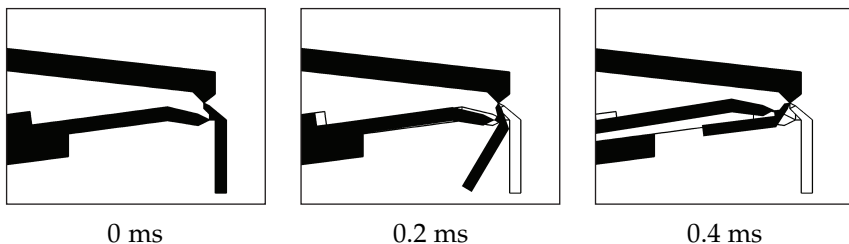


Figure 6.14: The flexible mechanism folds the Gurney flap within 0.4 ms.

6.4 Conclusion

This chapter shows the feasibility of the z-shaped mechanism for the deployment of the Gurney flap for the model blade. Refinements of the conceptual design obtained in Chapter 5 are obtained by means of FEM simulations and stress analysis of the structure. Materials and manufacturing considerations are also taken into account, although concessions must be made on the feasibility of flexible hinges to connect the Gurney flap. The resulting mechanism characteristics are presented in Table 6.3.

Length	50 mm
Weight per metre of wingspan	175 g/m
Gurney flap rotation	82°
Maximum voltage	95 V
Deployment/Folding duration	0.4 ms

Table 6.3: Characteristics of the final design of the z-shaped mechanism.

Refining such a system requires a truly multidisciplinary approach. To overcome all the challenges: mathematical and geometrical approaches are required to optimise displacements and forces, the capabilities of the material must be taken to the limit and complex manufacturing processes have to be investigated. Validating the mechanism requires analyses in many more disciplines. The following chapter investigates the constraints linked to the rotation of the model blade using a rigid body model. These constraints are combined with the aerodynamic forces from Chapter 4 to study the mechanism motion under external loads.

Dynamic simulation

7.1 Introduction

In the previous chapter, the flexible z-shaped mechanism and its connection to the Gurney flap was presented. The full mechanism consists of a flexible structure that amplifies the strains developed by two patch actuators into a circular motion. Such a motion allows the Gurney flap to be deployed within the 1 ms duration required to efficiently improve the lift of the rotorcraft. The aim of this chapter is to validate the behaviour of the mechanism under loads from the blade motion and the aerodynamic forces on the Gurney flap. The external constraints coming from the blade rotation are investigated by a rigid-body model of the blade and the rotor hub. The aerodynamic forces have been determined in Chapter 4 as a function of the blade orientation and deployment angles of the Gurney flap. A multi-body simulation is detailed in this chapter to obtain the loads resulting from the blade rotation. Finally, the calculated loads are implemented in a transient analysis of the mechanism to verify its performance under these external constraints.

7.1.1 A multi-domain problem

Simulating the complete actuation system in the helicopter blade is very complex and involves multiple interacting physical domains as shown in Figure 7.1 [173]. The piezoelectric is part of an electro-mechanical domain, the actuation mechanism and the blade are part of a mechanical domain and the blade behaviour is influenced by the aerodynamic domain. A complete simulation should implement the relations between these domains and assign for each a dedicated

simulation tool. Co-simulation procedures allow such connections to be made in order to perform the simulation of each domain in parallel [173, 174, 175]. The assumption that the mechanism is not affecting the overall behaviour of the blade is reasonable. The focus in this chapter is the validation of the mechanism under external loads and not the synchronised simulation of the blade, the rotor and the actuation mechanism. The constraints are therefore treated as independent contributions.

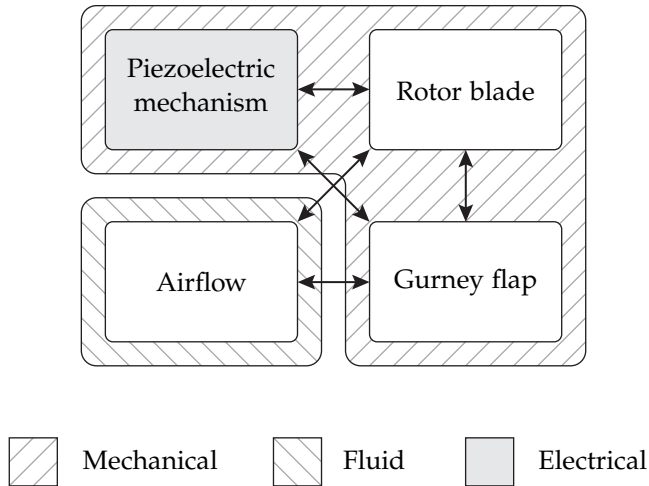


Figure 7.1: Distribution of physics domains across the system components.

7.1.2 Simulation environments

The simulation for the validation of the mechanism is done using three simulation tools.

- A multi-body simulation of the rotor blade and the rotor hub is performed with LMS Virtual.Lab Motion software [176].
- The piezoelectric mechanism is modelled through Comsol Multiphysics within the piezoelectric physics module [106].
- The aerodynamic simulations are performed with Comsol Multiphysics and the turbulent flow module.

These software modules were chosen for their capability to interface with Matlab: Comsol can be executed as part of a Matlab script and Virtual.Lab Motion

models can be exported as Simulink models where a Simulink or Virtual.Lab Motion solver can process them. The rigid body simulation and the CFD simulation calculate the loads on the actuation mechanism. The transient analysis performs the simulation of the mechanism under the calculated loads. The output of the transient analysis is the Gurney flap angle during the actuation cycle.

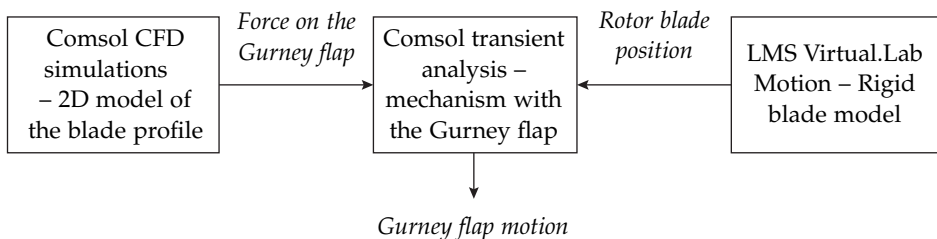


Figure 7.2: Sketch of the software modules utilised and their resulting data.

7.2 Multi-body simulation – Rigid blade simulation

The multi-body simulation is performed using LMS Virtual.Lab Motion. The model of the blade is a Mach-scaled version of the blade defined in the baseline blade definition document from GRC [102].

7.2.1 Model

Blade geometry

The baseline blade definition document provides detailed characteristics of the blade geometry, elastic and dynamic properties [127]. Many parameters such as the location of the centre of gravity, the location of the attachments for the connection to the hub are specified relative to the chord length (c) and radius (R) of the blade. The blade is defined from $0.2 R$. The connection to the rotor hub is ensured by a tension link. The centre of gravity is located at $0.4 R$. At the tip of the blade, the chord length is reduced as shown in Figure 7.3. The dimensions and the mass of the blade are scaled down: dimensions are divided by 8.15, the mass depends on the volume and is therefore divided by 8.15^3 . Table 7.1 shows the parameters necessary to build a rigid blade model of the model blade.

The rigid dynamic model of the blade is compared against the modal analysis of the blade performed by Agusta Westland and detailed in the baseline blade definition document [102]. The first flapping frequency (1.0771/rev) is very close to

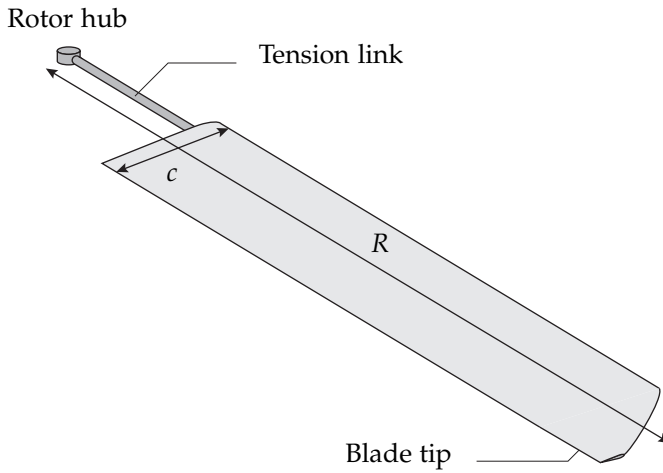


Figure 7.3: Sketch of the blade for the multi-body simulation.

Table 7.1: Scaled-down characteristics of the baseline blade.

Characteristics	Full-scale	Model blade
Chord length	650 mm	81 mm
Radius	8.15 m	1 m
Mass	186 kg	0.34 kg
Angular rotation	26.26 rad/s	210 rad/s
Moment of inertia	2812 kg/m ²	0.078 kg/m ²

the reference value from the document (1.0423/rev). Higher modes are not available for comparison because it is a rigid blade model.

Rotor components

The helicopter blade is linked to the rotor with a spherical hinge [102] as shown in Figure 7.4. The location of the hinge is at $0.05 R$. The blade pitching angle is controlled by the track rod. The connection and specifications of the track rod are taken from the baseline blade specification document [102]. The hinge range is limited to $\pm 20^\circ$ in every direction. This prevents the blade from coming into unrealistic positions before it reaches the correct rotation velocity.

The collective and cyclic control of the blade pitch during rotation is provided by the position of the connection point of the track rod. The position is adjusted to provide a cyclic pitch of $\pm 5^\circ$ during rotation. This trim condition does not

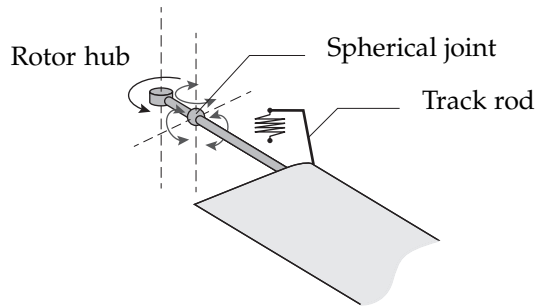


Figure 7.4: Sketch of the blade for the multi-body simulation.

correspond to a specific flight condition in particular, but is a realistic value. It provides an input to vary the orientation of the blade and obtain a realistic range of inertia constraints.

Rotation speed input

The simulation is driven by the rotation speed of the rotor. Its rotational velocity is gradually increased up to 210 rad/s as shown in Figure 7.5. This value is reached after one second, then the simulation continues until 5 seconds. Only the last second is considered for the loads evaluation to avoid transient effects from the rotation acceleration.

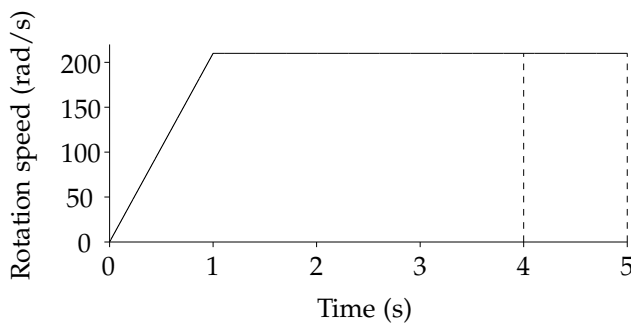
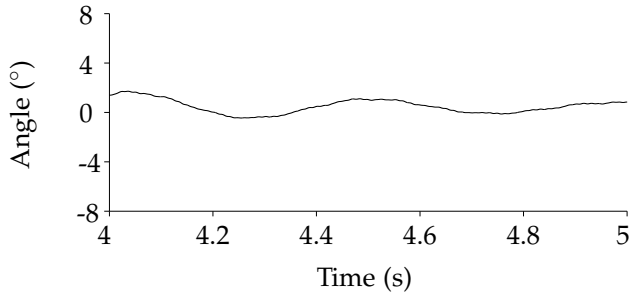


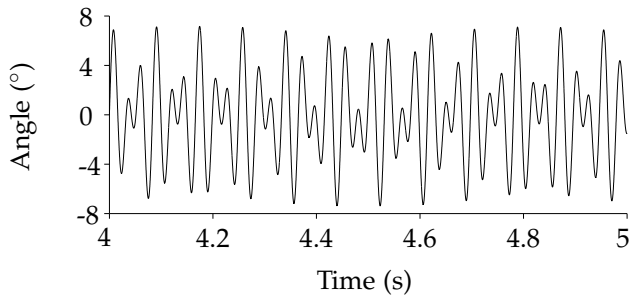
Figure 7.5: Rotational velocity of the rotor input function. The dashed lines (---) show the part of the simulation considered for the evaluation of the loads on the actuation system.

Results from the rotor simulation

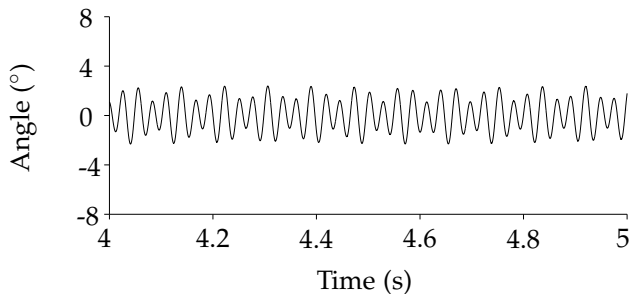
The lead-lag, flap and pitch angle of the rotor blade are shown in Figure 7.6. The lead-lag angle data shows low frequency oscillations (~ 2 Hz) due to the damping brought by the lag-damper. The flap and pitch angle show significant oscillations at 36 Hz, corresponding to the first flapping frequency.



a. Lead-lag angle



b. Pitch angle



c. Flap angle

Figure 7.6: Results of the multi-body blade and rotor simulation.

This data allows the determination of the acceleration due to the vibration of

the blade at the location of the actuation mechanism. This is used as an input to the subsequent transient FEM analysis of the actuation mechanism itself.

7.3 The Gurney flap mechanism – Constraints calculations

In this section, the constraints on the Gurney flap are calculated using the results of the multi-body simulation and the CFD data determined in Chapter 4. The location and size of the Gurney flap mechanism determine the magnitude of the acceleration and the aerodynamic forces. The Gurney flap cannot extend to the tip of the blade as shown in Figure 7.3. A realistic extension for the Gurney flap is between $0.5 R$ and $0.7 R$ [127]. The mechanism characteristics given in Chapter 5 are updated and are shown in Table 7.2.

Table 7.2: Characteristics of the actuation mechanism

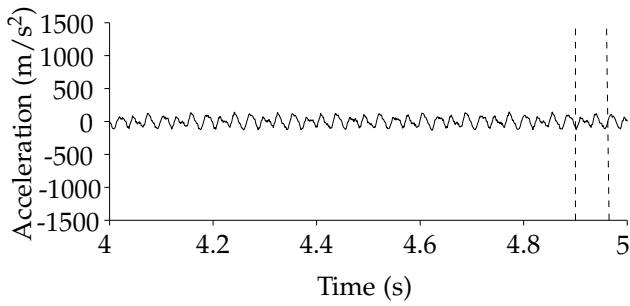
Width	200 mm
Length	50 mm
Gurney flap length	1.625 mm
Mass	35 g
Centre of mass (spanwise location)	$0.6 R$
Centre of mass (chordwise location)	$0.66 c$

7.3.1 Inertia loads on the mechanism

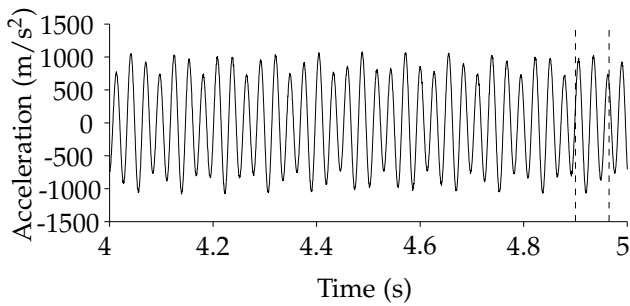
Using the results of the multi-body simulation, the acceleration at the centre of mass of the mechanism is calculated by means of coordinate transformation and differentiation, taking the second derivative of the position. Figure 7.7 shows the two acceleration components in the plane of the blade cross-section.

7.3.2 Aerodynamic loads

The aerodynamic loads are determined using the set of quasi-static CFD simulations detailed in Chapter 4. For the deployed Gurney flap, the normal force on the flap can be derived taking the motion of the blade into account and the location of the mechanism. Figure 7.8 shows the normal force on a fully deployed Gurney flap due to the airflow on the rotor blade for the last second of simulation. The motion of the rotor blade affects the orientation of the Gurney flap through the flow and modifies the applied force. The combination of both the accelerations at the location of the mechanism and the normal force on the Gurney flap provides a set of realistic constraints to faithfully simulate the mechanism.



a. Acceleration along the lead-lag axis



b. Acceleration along the flapping axis

Figure 7.7: Acceleration on the mechanism. The dashed lines (– –) show the data considered for the actuation cycle in the transient analysis.

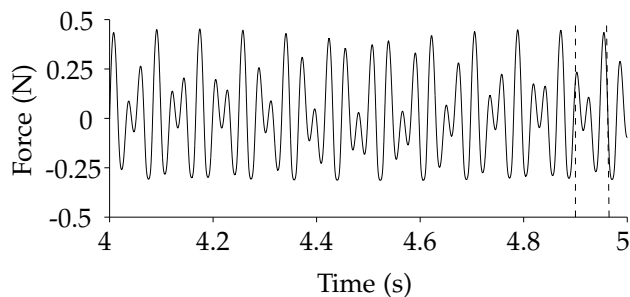


Figure 7.8: Normal force on a fully deployed Gurney flap calculated for one second of the rotor blade simulation. The dashed lines (– –) show the data considered for the actuation cycle in the transient analysis.

7.4 The mechanism validation

7.4.1 FEM transient analysis – Mechanism simulation

The FEM model is identical to the model presented in Chapter 6. It is a fully coupled electro-mechanical transient FEM simulation. It includes a contact model between the top arm of the mechanism and the skin of the profile. The input voltage for the two actuators is set using the driving voltage function detailed in Chapter 6. The aerodynamic force constraint is imposed on the Gurney flap surface, changing as a function of the Gurney flap deployment and the motion of the blade during the cycle. Finally, the two acceleration components in the plane of the blade cross-section are added to the mechanism's flexible structure. The mechanism motion is defined for one actuation cycle. The simulation starts with a deployed Gurney flap. The Gurney flap is quickly folded after the simulation has started. 30 ms later, the Gurney flap is deployed as shown in Figure 7.9. This duration equals the time for the blade to achieve half a rotation around the helicopter. The actuation cycle corresponds to the active lift control strategy where the Gurney flap is deployed within 1 ms over half a blade rotation (30 ms).

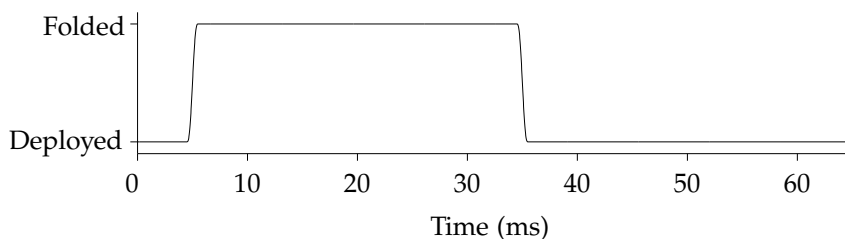


Figure 7.9: Actuation cycle for the deployment of the Gurney flap.

7.4.2 Results

The result of the simulation shows that the flexible mechanism is capable of developing sufficient mechanical power to fully fold and deploy the Gurney flap within the 1 ms duration requirement as shown in Figure 7.10.

The simulation shows that the mechanism authority is sufficient to follow the positioning specified by the input function. Some vibrations are present at the end of each step input. For the first step input at 5 ms, the deployment angle is allowed to reach amplitudes larger than -90° and to oscillate because no contact is implemented for between the Gurney flap and the mechanism. However, in the case of the deploying motion at 35 ms, the overshoot amplitude is reduced because the top part of the mechanism makes contact with the blade skin when reaching

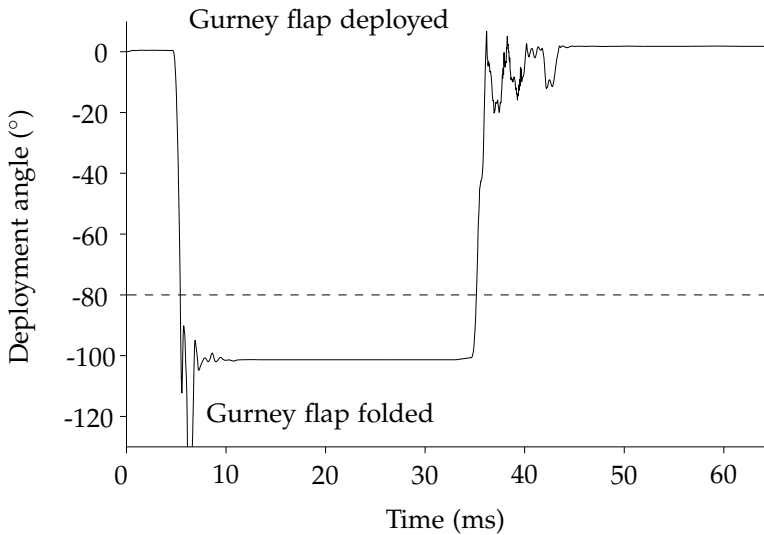


Figure 7.10: Deployment angle of the Gurney flap during the actuation cycle. The dashed line (– –) marks the angle where the Gurney flap is aligned with the profile skin, and therefore fully folded.

the deployed position. This prevents the Gurney flap from deploying further than its intended position.

7.4.3 Additional research

The vibrations shown in Figure 7.10 need to be alleviated to provide an accurate positioning of the Gurney flap in each position. This work is beyond the scope of the research done in this chapter. Possible improvements are listed below.

- Addition of damping material on the flexible structure
- Design of a damper at the end of the Gurney flap motion to absorb the extra energy due to the Gurney flap motion
- Control feedback loop on the actuation input profile

Controlling the mechanism with additional authority is possible because the full capabilities of the top actuator are not utilised. The work path of the actuation mechanism presented in Chapter 5 shows that more of the actuator force and displacement can be utilised.

7.5 Conclusion

Various simulation components are combined in a common framework in order to validate the performance of the Z-shape mechanism. It has been shown that the mechanism allows deployment and control of the Gurney flap under the combined loads due to the blade motion and the aerodynamics. A multi-body simulation of the rotor blade and rotor hub was performed. It provides the inertia loads, while the aerodynamic forces are obtained through a steady-state FEM analysis. The constraints are combined in a transient FEM analysis. The results show that the z-shaped actuation system is capable of folding or deploying the Gurney flap within 1 ms in a rotating blade, under aerodynamic loads. The addition of a control feedback loop and damping material to block the Gurney flap once in the blade profile would improve the motion.

Smart actuation mechanisms are difficult to analyse due to the lack of availability of cross-domain simulation tools. In the case of validating a mechanism behaviour, the investigation of the external loads independently is sufficient. However, for further simulations to fine-tune the control of an actuation system and to investigate its effects, an integrated multi-physics tool is necessary. The following chapter focuses on manufacturing a prototype of the z-shaped mechanism to verify that its behaviour is according to the models developed.

Prototyping

8.1 Introduction

In this research, a method to design an actuation system has been followed to develop a novel actuation system suitable for integration inside a model helicopter blade. Optimisation and refinements have been necessary to provide a design that is capable of delivering the required actuation under the dynamics and aerodynamic loads of a rotating blade. Manufacturing and testing a prototype of the geometry is the last step of this development process. The objective in this chapter is to validate the deformation simulations of the z-shaped geometry without the Gurney flap. This constitutes a partial validation of the mechanism. Here, the topology, the shape of the mechanism's hinges and the bottom sliding boundary condition are validated. A full validation of the mechanism requires testing the mechanism driven by piezoelectric actuators, enclosed in a blade section, under external loads. To manufacture the geometry, spark erosion machining has been chosen for its accuracy and for the level of detail it can provide.

8.1.1 Spark erosion

The spark erosion technique is a process for machining metallic material that consists of removing material using an electrical discharge [163, 177, 178, 179]. The frequency and duration of the discharge controls the amount of material removed. The advantages of this technique are its accuracy, the low roughness of the machined surfaces and the low residual stresses. The accuracy of such a

manufacturing technique allows components with complex shapes to be made, such as the flexure hinge presented in Chapter 6 [163, 178]. A typical spark erosion machine is composed of a wire/electrode mounted on a moving head, a fixed table onto which the block to be cut is clamped and a tank to retrieve the eroded material washed away, as shown in Figure 8.1. The shape to be cut is controlled by a computer that translates a numerical drawing into trajectories for the moving head.

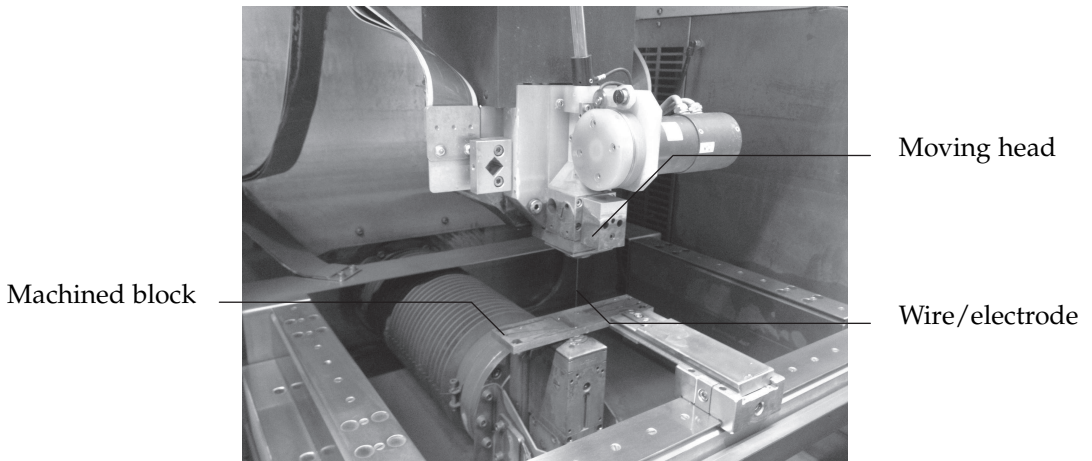


Figure 8.1: Picture of an AGIE spark erosion machine (courtesy of the laboratory of the Faculty of Electrical Engineering at the University of Twente).

The material chosen for manufacturing the z-shaped mechanism using the spark erosion technique is Stavax: a hard steel used for tooling and precision machining [168]. It is especially suited to allow the manufacturing of small features in complex structures. Its properties are listed in Table 8.1. This is not a typical material for manufacturing such a mechanism. However, this machining technique is able to deliver a prototype for quickly verifying this complex geometry.

Table 8.1: Stavax characteristics [168].

Young's modulus	200 GPa
Tensile strength	1420 MPa
Yield strength	1280 MPa

8.1.2 Geometry modifications

The size of the features the machine can achieve depends on the size of the wire/electrode. The size of the electrode is determined by the thickness of the

block that is cut. A good compromise is a thickness of 8 mm which sets the wire radius to 0.12 mm. It gives a reasonable thickness to work with, while providing enough resolution to resolve the majority of the geometry details. In the FEM model presented in Chapter 6, some of the features, such as curvatures close to the flexible hinges, are below this size. As a consequence, the geometry needs to be slightly adjusted for machining. However, the difference in geometry is limited between the FEM model and the machine z-shaped as shown in Figure 8.2. The spark erosion method is accurate enough to machined the flexible joints with a thickness of 0.08 mm as specified in Chapter 6. The main difference is the change in material properties. As a result, the flexible joints have a much larger bending stiffness. A good approximation for the bending stiffness k of circular flexible hinges is [160]:

$$k = 0.093 \sqrt{\frac{h}{D}} E w h^2 \quad (8.1)$$

where h is the thickness of the joint, D the diameter of the notches on each side of the hinge, E the Young's modulus of the material and w the width of the joint. As expected, the bending stiffness of the steel hinge of the prototype is 100 times stiffer than the polypropylene hinges selected for the final design of the mechanism in Chapter 6, as illustrated in equation 8.1. The prototype presented cannot be used to assess the performance of the final mechanism. However, it makes it possible testing of the complex deformation of the z-shaped mechanism and a comparison with a numerical model.

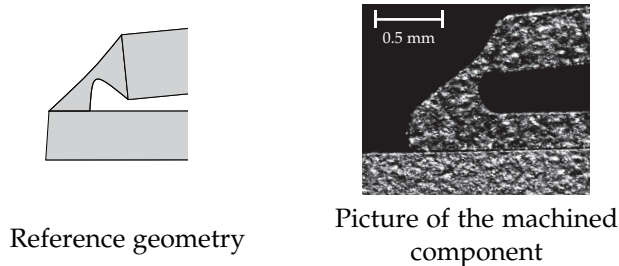


Figure 8.2: Comparison of the geometry defined in Chapter 6 and the resulting geometry of the machined component for the hinge connecting two arms of the z-shaped mechanism.

8.2 Prototype manufacturing and testing

The prototype machined using the spark erosion technique consists of the z-shaped geometry with a support block representing the lower skin of the blade profile as

shown in Figure 8.3. A large block is added to the z-shaped mechanism to represent the clamping boundary condition on the D-spar, as explained in Chapter 4.

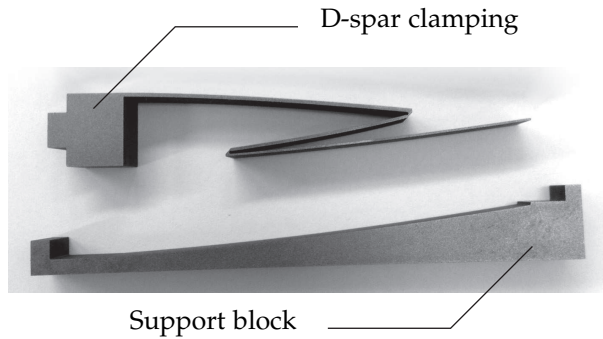


Figure 8.3: Picture of the prototype consisting of the z-shaped and a support block.

8.2.1 Experimental setup

The prototype has been made to test the accuracy of the deformation of the structure under load. The setup consists of an adjustable micrometer that pushes on the upper z-shaped arm as shown in Figure 8.4. The curve of the displacement at the tip of the mechanism as a function of the input displacement is compared against an updated FEM simulation that takes into account the larger Young's modulus of the material. The displacement at the tip of the bottom arm is measured by an optical microscope coupled with a CCD camera.

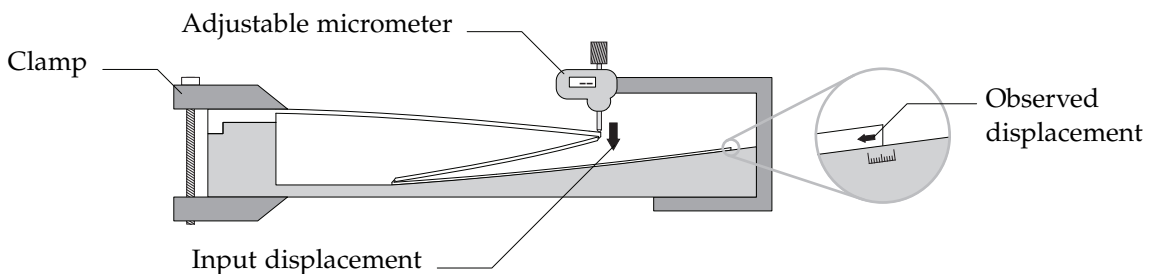


Figure 8.4: Sketch of the experimental setup to assess the z-shaped geometry.

Pictures are taken for four values of increasing and decreasing input displacements. The displacement of the tip of the end arm is retrieved based on the difference between successive pictures as shown in Figure 8.5.

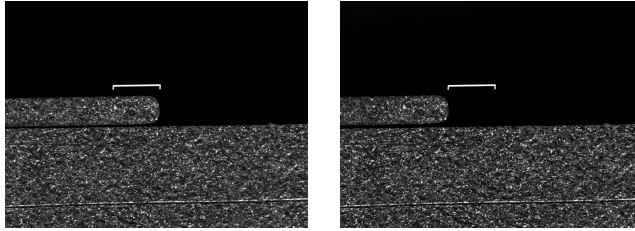


Figure 8.5: Displacement of 0.4 mm recorded between two pictures.

8.2.2 Results

The displacement curve is compared with a modified FEM simulation of the z-shaped mechanism as shown in Figure 8.6. For this simulation, Stavax is the material specified. The load of the micrometer is applied as a prescribed displacement on the nodes at the same location as in the experiment.

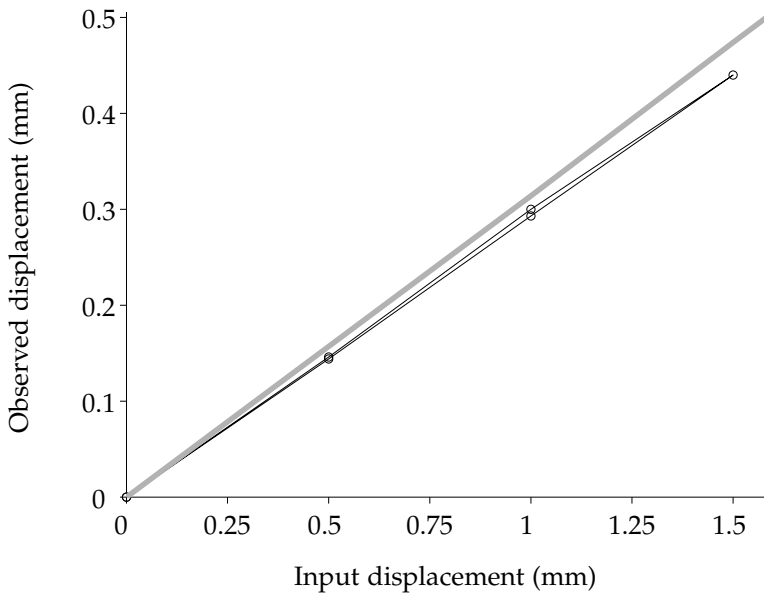


Figure 8.6: Deformation of the z-shaped mechanism for a displacement on the tip of the top arm of the mechanism. The experimental curve (—○—) is compared with the modified simulation (—).

The deviation of the slope of the measured data is less than 7% relative to the simulation data. For the displacement considered, there is no plastic deformation because the tip of the blade comes back to the starting position after one loading

cycle. No loss of contact is observed between the bottom arm and the surface of the supporting block during the displacement. This validates the sliding boundary condition used for the bottom arm. Larger displacements cause plastic deformation and a loss of contact due to the permanent deformation of the hinges.

8.3 Conclusion

The z-shaped mechanism prototype manufactured by spark erosion showed good agreement with the displacement predicted by the numerical model. It demonstrates the behaviour of the z-shaped mechanism for converting a bending motion into a horizontal displacement. The experiment also highlights the work done in Chapter 6 on the material selection for the flexible hinges. The full range of motion is not available to the prototype because of the material plastic deformation. The material available for prototyping is not the optimal material for these joints. The experiment is therefore only valid up to the onset of plastic deformation.

A study of polypropylene hinges is recommended to carry on this investigation and experimentally assess the performance of the mechanism with a Gurney flap. Knowledge of the capabilities of this material will help the manufacturing of the Gurney flap deployment mechanism as envisioned in this work.

Conclusions and recommendations

9.1 Conclusions

Progress in transportation is a continuous process towards the increase of fuel-efficiency, speed and comfort. Current helicopters are the result of collaborative work performed in various engineering disciplines. To further improve their performance, research is now heading towards active blade systems. The objective is to adapt the blade aerodynamic characteristics to the local aerodynamic conditions. Active blade systems can improve the blade efficiency, the rotorcraft maximum velocity and reduce its vibrations.

Smart blade concepts for helicopters require high performance actuation mechanisms. Developing specific mechanisms for these concepts is especially challenging due to the large variety of constraints, ranging from the internal centrifugal loading to the external aerodynamic forces. Piezoelectric-based actuation systems have the potential of addressing many of the constraints. Furthermore, they are available in many forms and offer ease of integration inside helicopter blades. Piezoelectric-based systems present the advantage of sustaining the large forces associated with the blade motion while providing a large specific work.

The present thesis focused on three research objectives. The following section discusses how each objective was met and what contribution was made by this research.

Objective 1: Development of a generic process to differentiate and select piezoelectric actuation technologies.

The selection process for piezoelectric actuators was established in Chapter 2. A straightforward procedure has been developed to assess the suitability of a set of piezoelectric actuators, knowing the mechanical work required by a specific application. In this selection process, many aspects of piezoelectric actuators are taken into account, such as their specific performance, their reliability and their ease of integration. The procedure is generic and can be extended for selecting other types of actuation systems. It gives a good starting point for the design of actuation systems.

Objective 2: Development of a multi-domain approach for designing and optimising smart actuation mechanisms.

Designing a smart actuation system is a multi-domain problem. The approach defined starts with the investigation of the required actuation loads followed by the optimisation of the actuation system geometry (detailed in Chapter 5). Smart actuation systems aim at interacting with an external physical domain. Therefore, care needs to be taken to evaluate the external domain before investigating the structure and performing the design process. It is essential to reduce the number of parameters for an efficient optimisation. The developed approach evaluates a large number of computer generated structures prior to the optimisation. This procedure has been proven to lead to an efficient optimisation and resulted, for the particular problem of the Gurney flap treated in this thesis, in a new structure.

Objective 3: Development of procedures to validate and test smart actuation systems.

A validation procedure for smart actuation systems has been developed in Chapter 6. It involves decoupling the complex relationships between the various physical domains of the system. The external constraints on the mechanism could be determined by means of this procedure. This allowed the use of dedicated tools for solving each domain separately and it provided realistic constraints. The testing procedure focused on the experimental validation of the actuator geometry and its numerical modelling. For this purpose, an accurate prototype of the actuation system was machined of which the deformations were in agreement with the model predictions. This is the first step of the mechanism experimental validation and recommendations are proposed to carry on experimental tests.

Among various active blade concepts, the active Gurney flap has currently the highest potential, as shown in Chapter 1. The procedures and approaches developed in this thesis were applied to the conception of an actuation system for deploying an active Gurney flap in the case of a Mach-scaled helicopter blade. For this application, the selection process led to d_{33} piezoelectric actuators. The multi-domain approach was carried out to determine the aerodynamic loads on the flap in Chapter 4 and to start the design process. The structure resulting from the optimisation procedure showed a new characteristic “Z” shape. In Chapter 6, the structure has been refined, taking into account additional details to provide a more realistic mechanism. Finally the testing procedure was applied. Dynamic and aerodynamic constraints were determined in Chapter 7. Simulation of the final mechanism under external constraints demonstrated its capability to perform under demanding environments. The development of this actuation system has been concluded with an experimental verification of the actuation system behaviour in Chapter 8, which constitutes a partial validation of the actuation system. The complete validation of the z-shape mechanism requires further studies to experimentally verify its capabilities under external loads within a blade section. The processes developed in this research have been successfully applied to design a suitable actuator system for an active Gurney flap.

9.2 Recommendations

This thesis defines frameworks and processes to design and develop smart actuation mechanisms. It resulted in a unique z-shaped design for the actuation of the Gurney flap. Although this is a fundamental step towards the development of actuation mechanisms for smart systems, additional research is still required to implement the proposed geometry.

The importance of flexible hinges for the final structure was detailed in Chapter 6. Further developments of the z-shaped geometry towards manufacturing involves the investigation of flexible polypropylene hinges. The potential of composite hinges was also highlighted. Composite hinges mimic the micro-structure of polypropylene hinges but with far more control on the material property by means of fibre density and orientation.

A full experimental validation of the mechanism remains to be performed. A first step consists in testing the structure deformation with piezoelectric actuators. The following experiments must include the response of the system inside a blade section under external loads.

The results of the transient analysis in Chapter 7 showed the successful authority of the z-shaped mechanism to fold and deploy the Gurney flap under external loads.

A dynamic analysis of the mechanism is necessary to investigate the vibrations present at the end of the folding and deployment motion. The addition of damping materials and the use of feedback control on the actuators are potential solutions to alleviate these vibrations.

Within the Clean Sky European project, experimental campaigns will be performed in the near future. The data generated will allow refinements of the numerical models. Coupling these models together is a challenge which remains difficult but necessary to further improve the design of smart systems.

Nomenclature

Roman

A	Surface area	[m ²]
A_i	Scaling voltage for actuator i	[V]
c	Chord length	[m]
C	Capacitance	[F]
c_d	Section drag coefficient	[-]
c_l	Section lift coefficient	[-]
d	Displacement	[m]
d_{ij}	Components of the piezoelectric coefficient matrix	[m/V]
D	Diameter of notches for a hinge	[m]
D_i	Components of the dielectric displacement vector	[C/m ²]
e_{bn}	Thickness of the first element in the CFD model	[m]
E	Young's modulus	[Pa]
E_{vi}	Components of the electrical field vector	[V/m]
f	Frequency	[Hz]
f_d	Drag per unit span of wing	[N/m]
f_l	Lift per unit span of wing	[N/m]
F_{bl}	Block force	[N]
F_d	Drag force	[N]
F_l	Lift force	[N]
h	Hinge thickness	[m]
H	Actuator height	[m]

k	Hinge rotational stiffness	[N · m]
K	Structure stiffness	[N/m]
l_e	Spacing between two electrodes	[m]
L	Actuator length	[m]
N	Number of mesh elements	[-]
Ma	Mach number	[-]
M_{GF}	Moment exerted by the flow on the Gurney flap	[N · m]
p	Pressure	[Pa]
P_{avg}	Average power	[W]
r	Coordinate along the blade	[m]
Re	Reynolds number	[-]
Re_s	Local Reynolds number	[-]
R	Blade length	[m]
s	Surface coordinate	[m]
t	Time coordinate	[s]
t_e	Thickness of a piezoelectric layer	[m]
T_c	Curie temperature	[°C]
U_{pp}	Peak to peak voltage	[V]
v	Air velocity	[m/s]
v_n	Air velocity normal to the blade	[m/s]
V	Voltage across electrodes	[V]
$V_i(t)$	Driving voltage function for actuator i	[V]
V_{max}	Maximum operating voltage	[V]
w	Width of the joint	[m]
W	Mechanical work	[J]
W_{GF}	Mechanical work to actuate the Gurney flap	[J]
$\hat{y}(x)$	Estimation of the surrogate function	[-]
x, y, z	Cartesian coordinates	[m]

Greek

β	Deployment angle of the Gurney flap	[°]
γ_i	Shear components of the strain vector	[-]
δ_{bn}	Boundary layer thickness	[m]
Δ_{free}	Free displacement	[m]
$\Delta_{\bar{F}_l}$	Loss of lift	[N]
ε_i	Normal strain components of the strain vector	[-]
η	Constant used in the estimation of the surrogate function	[-]
$\hat{\eta}$	Estimation of the base function in a Kriging model	[-]
σ_y	Stress along axis y	[N/m ²]
$\theta(t)$	Approximation function of the Heaviside step function	[-]

κ	Transition parameter for the Heaviside function approximation	[-]
μ	Dynamic viscosity	[Pa · s]
$\zeta(x)$	Function estimating data at the sampling points	[-]
ρ	Density	[kg/m ³]
ω	Rotational velocity	[rad/s]

Matrices

$[d]$	Piezoelectric matrix
$[\epsilon^T]$	Permittivity matrix under constant stress
$\hat{\mathbf{R}}$	Correlation matrix
$[S^{E_v}]$	Compliance matrix at constant electrical field
\mathbf{T}	Viscous stress tensor

Vectors

$\{D\}$	Dielectric displacement vector
$\{E_v\}$	Electrical field vector
\mathbf{f}	External force vector
\mathbb{I}	Unit vector
\mathbf{r}	Correlation vector
$\{S\}$	Strain vector
$\{T\}$	Stress vector
\mathbf{v}	Flow velocity vector
x	Parameter vector for the surrogate function

Mesh convergence for CFD simulations

A.1 Introduction

The CFD simulation performed in Chapter 4 uses a C-grid mesh. The mesh is defined with 150 elements in front, top and bottom of the aerofoil and 100 elements in the wake of the aerofoil. The rotor blade aerofoil section is described with 400 points to guarantee a smooth discretization. The resulting mesh consists of 92,790 elements. The convergence of the simulation is verified by reducing and increasing the number of elements of the mesh. The thickness of the element at the aerofoil contour is determined using the following rule to keep its thickness significantly smaller than the boundary layer, as detailed in section 4.2.2:

$$e_{bn} = \frac{10c}{Re} \quad (\text{A.1})$$

where c is the chord length of the aerofoil and Re is the Reynolds number. Therefore, although the number of elements is modified, the thickness of the first element is still smaller than the thickness of the boundary layer. The lift on the entire profile and the normal force on the Gurney flap have been computed for meshes containing as small as 17,289 elements to meshes containing up to 732,100 elements. The case for which the solution procedure converges the most slowly is taken: Mach 0.6 with 10° of angle of attack and a fully deployed Gurney flap ($Re = 11.4 \times 10^5$).

A.2 CFD simulation convergence

The mesh convergence curve is plotted for the lift section coefficient and for the normal force on the Gurney flap as shown in Figures A.1 and A.2. There is little improvement in the calculated section lift when increasing the number of elements compared to the reference simulation, whereas the deviation is much more significant when decreasing the number of elements. Finally, the mesh density has little influence on the calculation of the normal force on the Gurney flap as shown in Figure A.2.

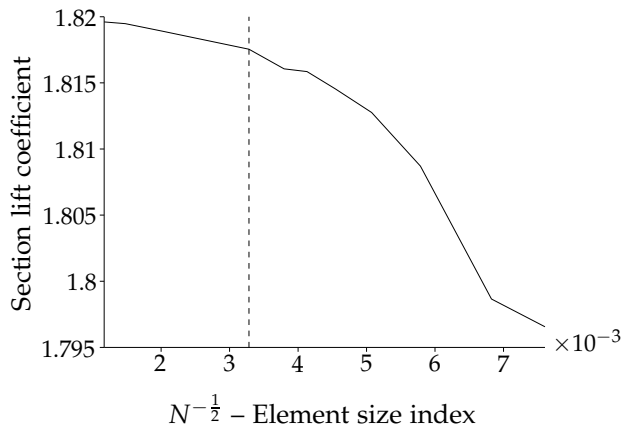


Figure A.1: Mesh convergence curve for the section lift coefficient. N is the number of mesh elements. The dashed line (---) indicates the mesh density chosen.

A.3 Computation time

The computation time required for each numerical simulation depends directly on the resolution of the mesh. 550 simulations are required to obtain the force and moment on the Gurney flap for the combination of angles of attack (10), deployment angles (10) and Mach numbers (5) chosen. Taking a mesh with 732,100 elements would result in just over 300 days of computed time using the dedicated computer detailed in Table A.1. The total simulation time with the chosen mesh parameters is under 10 days as shown in Figure A.3. This figure is brought down to just over 5 days by parallelizing the simulations. Each simulation is limited to 4 threads and two simulations are performed in parallel.

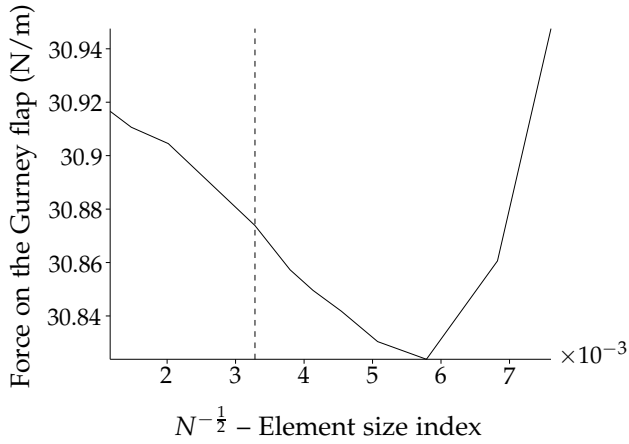


Figure A.2: Mesh convergence curve for the normal force on the Gurney flap. N is the number of mesh elements. The dashed line (- -) indicates the mesh density chosen.

Table A.1: Specifications of the computer used for CFD simulations.

Operating system	Linux CentOS 5.8
Cpus type	2 × Intel® Xenon® E5520 @ 2.27 GHz
Cpu cores	2 × 4
Threads available	8
RAM type	DDR2
RAM capacity	24 GB
RAM frequency	1333 MHz

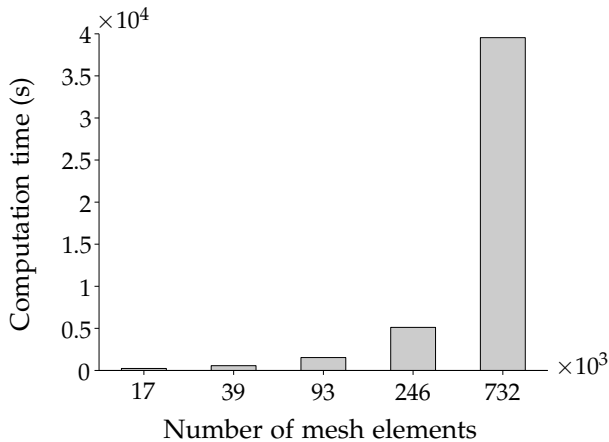


Figure A.3: Computation time required for five simulations.

A.4 Conclusion

The convergence of the simulation for the chosen mesh settings has been verified. The mesh resolution used constitutes the right balance between computation time and accuracy of the solution for this application.

The ordinary Kriging model

An ordinary Kriging model can be defined as a base function which represents the global trend of the data with a stochastic function that approaches the data computed at the sampling points.

A Kriging model can be defined as:

$$\hat{y}(x) = \eta + \zeta(x) \quad (\text{B.1})$$

where $\hat{y}(x)$ is the estimation of the surrogate function for a set of parameters x , η is a constant value corresponding to the base function of the ordinary Kriging model and $\zeta(x)$ is the function which estimates data modelled at the sampling points.

A Gaussian correlation is used for this model:

$$R(x_i, x_j) = e^{-\theta(x_i - x_j)^2} \quad (\text{B.2})$$

where x_i and x_j are parameters values. θ is a scaling parameter for the correlation function, of which the value depends on the problem considered.

Then the base function is estimated:

$$\hat{\eta} = \frac{X^T \hat{R}^{-1} y}{X^T \hat{R}^{-1} X} \quad (\text{B.3})$$

Where $\hat{\eta}$ is the estimation of the base function, \hat{R} is the correlation matrix and X is a unit vector (ordinary Kriging case).

Therefore the prediction of the Kriging model is:

$$\hat{y} = \hat{\eta} + \mathbf{r}^T \hat{\mathbf{R}}^{-1} (\mathbf{y} - \mathbb{I} \hat{\eta}) \quad (\text{B.4})$$

Where \hat{y} is the estimation of y , \mathbf{r} is the correlation vector between the set of parameters y is evaluated at and the parameters at which the surrogate function has been evaluated and \mathbb{I} is a unit vector.

Bibliography

- [1] J. Gordon Leishman. *Principles of Helicopter Aerodynamics*. 2006.
- [2] L. Breguet. Revolving Supporting Surfaces. *US Patent 1,919,089*, 1933.
- [3] K.M. Rosen. A Prospective: The Importance of Propulsion Technology to the Development of Helicopter Systems with a Vision for the Future. The 27th Alexander A. Nikolsky Lecture. *Journal of the American Helicopter Society*, 53(4):31.
- [4] J.A.J. Bennett. Helicopter and Gyroplane. *US patent 2,344,967*, 1944.
- [5] I. Sikorsky. Helicopter and Controls therefor. *US Patent 2,318,260*, 1943.
- [6] L. LePage. Flight on rotating wings. *Journal of the Franklin Institute*, 222, 1936.
- [7] A.R.S. Bramwell, G. Done, and D. Balmford. *Bramwell's Helicopter Dynamics*. Elsevier, 2000.
- [8] G.H. Saunders. *Dynamics of helicopter flight*. Wiley-Interscience, 1975.
- [9] L. Breguet. Flying machine having revolving supporting surfaces. *US Patent 1,986,709*, 1935.
- [10] I. Sikorsky. Helicopter rotor. *US Patent 2,627,929*, 1947.
- [11] R.P. Pescara. Screw propeller of helicopter flying machines. *US Patent 1,449,129*, 1923.

- [12] N.A. Koratkar and I. Chopra. Wind Tunnel Testing of a Mach-Scaled Rotor Model with Trailing-Edge Flaps. *Journal of the American Helicopter Society*, 47(4):263–272.
- [13] J. Shen and I. Chopra. A Parametric Design Study for a Swashplateless Helicopter Rotor with Trailing-Edge Flaps. *Journal of the American Helicopter Society*, 49(1):43, 2004.
- [14] I-G. Lim and I. Lee. Aeroelastic analysis of rotor systems using trailing edge flaps. *Journal of Sound and Vibration*, 321(3-5):525–536, April 2009.
- [15] I. Chopra. Review of State of Art of Smart Structures and Integrated Systems. *AIAA Journal*, 40(11):2145–2187, November 2002.
- [16] A. Altmikus, A. Dummel, R. Heger, and D. Schimke. Actively controlled rotor: aerodynamic and acoustic benefit for the helicopter today and tomorrow. In *34th European Rotorcraft Forum*, Liverpool, 2008.
- [17] S. Viswamurthy and R. Ganguli. An optimization approach to vibration reduction in helicopter rotors with multiple active trailing edge flaps. *Aerospace Science and Technology*, 8(3):185–194, April 2004.
- [18] P.P. Friedmann, M. de Terlizzi, and T.F. Myrtle. New developments in vibration reduction with actively controlled trailing edge flaps. *Mathematical and Computer Modelling*, 33(10-11):1055–1083, May 2001.
- [19] J-S. Kim, K.W. Wang, and E.C. Smith. Development of a resonant trailing-edge flap actuation system for helicopter rotor vibration control. *Smart Materials and Structures*, 16(6):2275–2285, December 2007.
- [20] Y.H. Yu, B. Gmelin, and W. Splettstoesser. Reduction of helicopter blade-vortex interaction noise by active rotor control technology. *Progress in Aerospace*, 33(97):647–687, 1997.
- [21] M.K. Singh, K. Dhanalakshmi, and S.K. Chakrabarty. Navier-Stokes Analysis of Airfoils with Gurney Flap. *Journal of Aircraft*, 44(5):1487–1493, September 2007.
- [22] M. Thiel. *Actuation of an active Gurney flap for rotorcraft applications*. PhD thesis, The Pennsylvania State University, 2006.
- [23] K. Yee, W. Joo, and D-H. Lee. Aerodynamic Performance Analysis of a Gurney Flap for Rotorcraft Application. *Journal of Aircraft*, 44(3):1003–1014, May 2007.
- [24] M.D. Maughmer and G. Bramesfeld. Experimental Investigation of Gurney Flaps. *Journal of Aircraft*, 45(6):2062–2067, November 2008.

-
- [25] J.J. Wang, Y.C. Li, and K-S. Choi. Gurney flap-Lift enhancement, mechanisms and applications. *Progress in Aerospace Sciences*, 44(1):22–47, January 2008.
- [26] L. Liu, A. Padthe, and P. Friedmann. Computational Study of Microflaps with Application to Vibration Reduction in Helicopter Rotors, 2011.
- [27] B.C. Kuo and S-K. Nesrin. Conceptual study of micro-tab device in airframe noise reduction: (I) 2D computation. *Aerospace Science and Technology*, 14(5):307–315, July 2010.
- [28] S. Lee and K.W. McAlister. Characteristics of deformable leading edge for high performance rotor. *AIAA Journal*, 35, 1993.
- [29] P.B. Martin, K.W. McAlister, and M.S. Chandrasekhara. Dynamic Stall Measurements and Computations for a VR-12 Airfoil with a Variable Droop Leading Edge. Technical report, 2003.
- [30] W. Geissler and M. Trenker. Numerical investigation of dynamic stall control by a nose-drooping device. Technical Report C, 2002.
- [31] M.S. Chandrasekhara. Compressible dynamic stall vorticity flux control using a dynamic camber airfoil. *Sadhana*, 32(1-2):93–102, August 2007.
- [32] M.S. Chandrasekhara. Optimum Gurney flap height determination for lost-lift recovery in compressible dynamic stall control. *Aerospace Science and Technology*, 14(8):551–556, December 2010.
- [33] E. Breitbach and A. Büter. The main sources of helicopter vibration and noise emissions and adaptive concepts to reduce them. *Journal of Structural Control*, 3(1-2):21–32, June 1996.
- [34] E. Stanewsky. Adaptive wing and flow control technology. *Progress in Aerospace Sciences*, 37(7):583–667, October 2001.
- [35] F. Gandhi, M. Frecker, and A. Nissly. Design Optimization of a Controllable Camber Rotor Airfoil. *AIAA Journal*, 46(1):142–153, January 2008.
- [36] H.P. Monner. Realization of an optimized wing camber by using formvariable flap structures. *Aerospace Science and Technology*, 5:445–455, 2001.
- [37] R. Barrett and J. Stutts. Design and testing of a 1/12th-scale solid state adaptive rotor. 491, 1997.
- [38] M.L. Wilbur, P.H. Mirick, W.T. Yeager, C.W. Langston, C.E.S. Cesnik, and S. Shin. Vibratory Loads Reduction Testing of the NASA/Army/MIT Active Twist Rotor. *Journal of the American Helicopter Society*, 47(2):11, 2002.

- [39] S.J. Shin, C.E.S. Cesnik, W.K. Wilkie, and M.L. Wilbur. Design and Manufacturing of a Model-scale Active Twist Rotor Prototype Blade. *Journal of Intelligent Material Systems and Structures*, 19(12):1443–1456, May 2008.
- [40] D. Thakkar and R. Ganguli. Induced shear actuation of helicopter rotor blade for active twist control. *Thin-Walled Structures*, 45(1):111–121, January 2007.
- [41] J. Riemenschneider, S. Opitz, M. Schulz, and V. Plassmeier. Active Twist Rotor for Wind Tunnel Investigations. In *Proceedings of the ASME 2010 Conference on Smart Materials, Adaptive Structures and Intelligent Systems*, pages 371–378. ASME, January 2010.
- [42] E.R. Booth and M.L. Wilbur. Acoustic Aspects of Active-Twist Rotor Control. *Journal of the American Helicopter Society*, 49(1):8, 2004.
- [43] T. Liu, J. Montefort, W. Liou, S.R. Pantula, and Q.A. Shams. Lift Enhancement by Static Extended Trailing Edge. *Journal of Aircraft*, 44(6):1939–1947, November 2007.
- [44] D. Greenblatt and I. Wygnanski. The control of flow separation by periodic excitation. *Progress in Aerospace Science*, 36, 2000.
- [45] J.M. Tomas, A.E.T. van der Weide, H. de Vries, and H. Hoeijmakers. Numerical simulation of flow control by synthetic jet actuation. In *27th Congress of International Council of the Aeronautical Sciences*, 2010.
- [46] G. Hong. Effectiveness of micro synthetic jet actuator enhanced by flow instability in controlling laminar separation caused by adverse pressure gradient. *Sensors And Actuators*, 132(2006):607–615, 2006.
- [47] A.S. Yang, J.J. Ro, M.T. Yang, and W.H. Chang. Investigation of piezoelectrically generated synthetic jet flow. *Journal of Visualization*, 12(1):9–16, 2009.
- [48] J. Meijerink and H. Hoeijmakers. Plasma Actuators for Active Flow Control on Wind Turbine Blades. In *29th AIAA Applied Aerodynamics Conference*, 2011.
- [49] D. Sturzebecher and W. Nitsche. Active cancellation of Tollmien-Schlichting instabilities on a wing using multi-channel sensor actuator systems. *International Journal of Heat and Fluid Flow*, 24(4):572–583, August 2003.
- [50] L.N. Cattafesta, Q.I. Song, D.R. Williams, C.W. Rowley, and F.S. Alvi. Active control of flow-induced cavity oscillations. *Progress in Aerospace Sciences*, 44:479–502, 2008.
- [51] R. Duvigneau and M. Visonneau. Simulation and optimization of stall control for an airfoil with a synthetic jet. *Aerospace Science and Technology*, 10(4):279–287, May 2006.

-
- [52] F.K. Straub, D.K. Kennedy, and A.D. Stemple. Development and whirl tower test of the SMART active flap rotor. *SPIE Conf. on Smart*, 2004.
- [53] S. Kota, G. Ervin, and R. Osborn. Design and Fabrication of an Adaptive Leading Edge Rotor Blade. *American Helicopter Society Annual Forum*, 2008.
- [54] B. Watson, J. Friend, and L. Yeo. Piezoelectric ultrasonic micro/milli-scale actuators. *Sensors and Actuators A: Physical*, 152(2):219–233, June 2009.
- [55] NewScaleTechnologies. New Scale Technologies - precision motion for micro imaging and vision systems. <http://www.newscaletech.com/>, 2012.
- [56] M.R. Thiel and G.A. Lesieutre. New Actuation Methods for Miniature Trailing-Edge Effectors for Rotorcraft. *AIAA Proceedings*, (May), 2009.
- [57] A. Paternoster, R. Loendersloot, A. de Boer, and R. Akkerman. Geometric Optimisation of Hinge-less Deployment System for an Active Rotorblade. In *Proceedings of the ASME 2011 Conference on Smart Materials, Adaptive Structures and Intelligent Systems*. ASME, November 2011.
- [58] J-H. Kwon, K-J. Hwang, S-S. Kim, P-J. Kim, and C-S. Kim. Fatigue life evaluation in composite rotor blade of multipurpose helicopter. In *Proceedings 6th Russian-Korean International Symposium on Science and Technology. KORUS-2002 (Cat. No.02EX565)*, pages 15–20. IEEE.
- [59] E. Head. Blade Trouble | Vertical - Helicopter News. 2012.
- [60] J.W. Bennett, B.C. Mecrow, A.G. Jack, D.J. Atkinson, S. Sheldon, B. Cooper, G. Mason, C. Sewell, and D. Cudley. A prototype electrical actuator for aircraft flaps and slats. *IEEE International Conference on Electric Machines and Drives, 2005.*, pages 41–47, 2005.
- [61] A. Haber and S.A. Jacklin. Development, manufacturing, and component testing of an individual blade control system for a UH-60 Helicopter Rotor. *American Helicopter*, 2002.
- [62] CleanSky. Clean Sky Joint Technology Initiative. <http://www.cleansky.eu>, 2012.
- [63] P. Curie and J. Curie. Développement, par pression, de l'électricité polaire dans les cristaux hémihédres à faces inclinées. *Comptes rendus hebdomadaires des séances de l'Académie des Sciences*, 91:294–295, 1880.
- [64] R.J. Bobber. Twenty years of sonar calibration methods – USRL research report no 56. *Department of the Navy – Underwater sound reference laboratory*, 1961.
- [65] K. Graff. Historical highlights in ultrasonics. In *Proceedings of the 2004 IEEE International Frequency Control Symposium and Exposition*, pages 5–10. IEEE, 2004.

- [66] M.H. Oude Nijhuis. *Analysis tools for the design of active structural acoustic control systems*. PhD thesis, University of Twente, November 2003.
- [67] V. Giurgiutiu. *Structural Health Monitoring with Piezoelectric Wafer Active Sensors*. Academic Press, 2008.
- [68] Smart Material. Smart Material Corp. Production, Engineering and Design of Advanced Piezo Composite Actuators, Ultrasonic Transducer, Piezo Electronics and Energy Harvester. <http://www.smart-material.com/>, 2012.
- [69] Piezomechanik GmbH. PIEZOMECHANICS – the innovative motion control. <http://www.piezomechanik.com/>, 2012.
- [70] Physik Instrumente. PI Leader in: Precision Nano-Positioning & Piezo Engineering, NanoAutomation, Piezo Stage, Hexapod, PZT, Piezo Actuator, Transducer: Sub-Nanometer Resolution, Metrology, Photonic Packaging Automation, Piezo Linear Motor, Steering Mirror, Translation. <http://www.physikinstrumente.com/>, 2012.
- [71] A. Vinogradov and F. Holloway. Electro-mechanical properties of the piezoelectric polymer PVDF. *Ferroelectrics*, 226(1):169–181, April 1999.
- [72] G.A. Atkinson and Z. Ounaies. Polymer Microsystems: Materials and Fabrication. In M. Gad-El-Hak, editor, *MEMS: Design and Fabrication*. CRC Press Taylor & Francis Group, 2006.
- [73] D.J. Hourston and I.D. Hughes. Poly(vinylidene fluoride) - poly(methyl methacrylate) blends. *Polymer*, 18(11):1175–1178, November 1977.
- [74] C-H. Nguyen. A Comparison of Dynamic Piezoactuation of Fiber-based Actuators and Conventional PZT Patches. *Journal of Intelligent Material Systems and Structures*, 17(1):45–55, January 2006.
- [75] S. Mekid and B. Lim. Characteristics comparison of piezoelectric actuators at low electric field: analysis of strain and blocking force. *Smart Materials and Structures*, 13(5):N93–N98, October 2004.
- [76] A. Deraemaeker and H. Nasser. Numerical evaluation of the equivalent properties of Macro Fiber Composite (MFC) transducers using periodic homogenization. *International Journal of Solids and Structures*, 47(24):3272–3285, December 2010.
- [77] A.E. Glazounov, Q.M. Zhang, and C. Kim. Torsional Actuator and Stepper Motor Based on Piezoelectric d 15 Shear Response. *Journal of Intelligent Material Systems and Structures*, 11(6):456–468, June 2000.

-
- [78] A.E. Glazounov, Q.M. Zhang, and C. Kim. Torsional actuator based on mechanically amplified shear piezoelectric response. *Sensors and Actuators A: Physical*, 79(1):22–30, January 2000.
- [79] M. Gall and B. Thielicke. Life-span investigations of piezoceramic patch sensors and actuators. In *The 14th International Symposium on: Smart Structures and Materials & Nondestructive Evaluation and Health Monitoring*, pages 65260P–65260P–12, April 2007.
- [80] S. Wang and K.X. Liu. Experimental research on dynamic mechanical properties of PZT ceramic under hydrostatic pressure. *Materials Science and Engineering: A*, 528(21):6463–6468, August 2011.
- [81] J.A. Juuti, H. Jantunen, V.P. Moilanen, and S. Leppävuori. Manufacturing of prestressed piezoelectric unimorphs using a postfired biasing layer. *IEEE transactions on ultrasonics, ferroelectrics, and frequency control*, 53(5):838–46, May 2006.
- [82] D. Damjanovic. *The Science of Hysteresis*, volume III. Elsevier, 2006.
- [83] H.M.S. Georgiou and R.B. Mrad. Dynamic electromechanical drift model for PZT. *Mechatronics*, 18(2):81–89, March 2008.
- [84] H. Janocha and K. Kuhnen. Real-time compensation of hysteresis and creep in piezoelectric actuators. *Sensors and Actuators A: Physical*, 79(2):83–89, February 2000.
- [85] H.-W. Joo, C.-H. Lee, J.-S. Rho, and H.-K. Jung. Analysis of temperature rise for piezoelectric transformer using finite-element method. *IEEE Transactions on Ultrasonics, Ferroelectrics and Frequency Control*, 53(8):1449–1457, August 2006.
- [86] S.-W. Zhou and C. A. Rogers. Heat Generation, Temperature, and Thermal Stress of Structurally Integrated Piezo-Actuators. *Journal of Intelligent Material Systems and Structures*, 6(3):372–379, May 1995.
- [87] M.W. Hooker. Properties of PZT-Based piezoelectric ceramics between -150 and 250C. *NASA/CR-1998-208708*, 1998.
- [88] CedratTechnologies. CEDRAT TECHNOLOGIES: Innovation in Mechatronics. *www.cedrat-technologies.com*, 2012.
- [89] P. Bouchilloux, F. Claeysen, and R. Le Letty. Amplified piezoelectric actuators: from aerospace to underwater applications. In Eric Udd, Yoseph Bar-Cohen, Kon-Well Wang, Dimitris C. Lagoudas, Eric H. Anderson, Vijay K. Varadan, Alison B. Flatau, Shih-Chi Liu, Ralph C. Smith, and Daniele Inaudi, editors, *Smart Structures and Materials*, pages 143–154, July 2004.

- [90] F. Claeysen, R. Le Letty, F. Barillot, N. Lhermet, H. Fabbro, P. Guay, M. Yorck, and P. Bouchilloux. Mechanisms based on piezoactuators. In Vittal S. Rao, L. Porter Davis, Eric Udd, Yoseph Bar-Cohen, S.-C. Liu, Daniel J. Inman, Anna-Maria R. McGowan, Christopher S. Lynch, Vijay K. Varadan, and Daniele Inaudi, editors, *SPIE's 8th Annual International Symposium on Smart Structures and Materials*, pages 225–233, June 2001.
- [91] J. Li, R. Sedaghati, J. Dargahi, and D. Waechter. Design and development of a new piezoelectric linear Inchworm actuator. *Mechatronics*, 15(6):651–681, July 2005.
- [92] H. Marth. Method for operating a piezo linear drive with a group of piezo stack actuators. *EU Patent 2209202A2*.
- [93] P. Hagedorn and J. Wallaschek. Travelling wave ultrasonic motors, Part I: Working principle and mathematical modelling of the stator. *Journal of Sound and Vibration*, 155(1):31–46, May 1992.
- [94] K. Uchino. Piezoelectric actuators/ultrasonic motors-their developments and markets. In *Proceedings of 1994 IEEE International Symposium on Applications of Ferroelectrics*, pages 319–324. IEEE, 1995.
- [95] J.L. Petitniot, H-M. Rochettes, and P. Leconte. Experimental assessment and further development of amplified piezo actuators for active flap devices. In *Actuator*, number June, pages 10 – 12, 2002.
- [96] F. Claeysen, A. Ducamp, F. Barillot, R. Le Letty, T. Porchez, O. Sosnicki, and C. Belly. Stepping actuators based on APAs. In *Proceedings of Actuator 2008*, pages 28–32, Bremen, 2008.
- [97] J.M. Lloyd. *Electrical Properties of Macro-Fiber Composite Actuators and Sensors*. PhD thesis, Virginia Polytechnic Institute and State University, 2004.
- [98] M. Melnykowycz, X. Kornmann, C. Huber, M. Barbezat, and A.J. Brunner. Performance of integrated active fiber composites in fiber reinforced epoxy laminates. *Smart Materials and Structures*, 15(1):204–212, February 2006.
- [99] V.K. Wickramasinghe and N.W. Hagood. Material characterization of active fiber composites for integral twist-actuated rotor blade application. *Smart Materials and Structures*, 13(5):1155–1165, October 2004.
- [100] TenCate. TenCate - Materials that make a difference. <http://www.tencate.com>, 2012.
- [101] R. Paradies and M. Melnykowycz. Numerical Stress Investigation for Piezoelectric Elements with a Circular Cross Section and Interdigitated Electrodes. *Journal of Intelligent Material Systems and Structures*, 18(9):963–972, January 2007.

-
- [102] W. Maybury, A. D'Andrea, R. Hilditch, P. Beaumier, and C. Garcia-Duffy. Baseline Blade Definition for GRC1.1. Technical report, GRC Report CS JU/ITD GRC/RP/1.1/31002, 2009.
- [103] N.A. Koratkar and I. Chopra. Wind tunnel testing of a Mach-scaled rotor model with trailing-edge flaps. *Smart Materials and Structures*, 10(1), 2001.
- [104] F. Straub, H.T. Ngo, V. Anand, and D. Domzalski. Development of a Piezoelectric Actuator for Trailing Edge Flap Control of Full Scale Rotor Blades. *Smart Materials and Structures*, Vol. 10, No., 1:101088/0964–1726/10/1/303, 2001.
- [105] J.D. Anderson. *Introduction to Flight*. McGraw-Hill Series in Aeronautical and Aerospace Engineering. McGraw-Hill, 2004.
- [106] COMSOL. COMSOL Multiphysics Engineering Simulation Software. <http://www.comsol.com>, 2012.
- [107] G.K. Batchelor. *An Introduction to Fluid Dynamics*. Cambridge Mathematical Library. Cambridge University Press, 1967.
- [108] D.J. Acheson. *Elementary Fluid Dynamics*. Oxford Applied Mathematics and Computing Science Series. Oxford University Press, USA, 1990.
- [109] J.D. Anderson. *Fundamentals of aerodynamics*. McGraw-Hill, 2001.
- [110] A. Roshko. Experiments on the flow past a circular cylinder at very high Reynolds number. *Journal of Fluid Mechanics*, 10(03):345–356, May 1961.
- [111] D. Kuzmin, O. Mierka, and S. Turek. On the implementation of the k- ϵ turbulence model in incompressible flow solvers based on a finite element discretisation. *International Journal of Computing Science and Mathematics*, 1(2):193–206, 2007.
- [112] H.K. Versteeg and W. Malalasekera. *An Introduction to Computational Fluid Dynamics: The Finite Volume Method*. Pearson Education Limited, 2 edition, 2007.
- [113] D.C. Wilcox. *Turbulence Modeling for CFD*. DCW Industries, Inc., 1994.
- [114] C.H. Park and S.O. Park. On the limiters of two-equation turbulence models. *International Journal of Computational Fluid Dynamics*, 19(1):79–86, January 2005.
- [115] P.R. Spalart. Strategies for turbulence modelling and simulations. *International Journal of Heat and Fluid Flow*, 21(3):252–263, June 2000.
- [116] U. Bunge, C. Mockett, and F. Thiele. Guidelines for implementing Detached-Eddy Simulation using different models. *Aerospace Science and Technology*, 11(5):376–385, June 2007.

- [117] R.D. Sandberg and L.E. Jones. Direct numerical simulations of low Reynolds number flow over airfoils with trailing-edge serrations. *Journal of Sound and Vibration*, 330(16):3818–3831, August 2011.
- [118] H. Shan, L. Jiang, and C. Liu. Direct numerical simulation of flow separation around a NACA 0012 airfoil. *Computers & Fluids*, 34(9):1096–1114, November 2005.
- [119] T.J. Baker. Mesh generation: Art or science? *Progress in Aerospace Sciences*, 41(1):29–63, January 2005.
- [120] D. Ait-Ali-Yahia, G. Baruzzi, W.G. Habashi, M. Fortin, J. Dompierre, and M-G. Vallet. Anisotropic mesh adaptation: towards user-independent, mesh-independent and solver-independent CFD. Part II. Structured grids. *International Journal for Numerical Methods in Fluids*, 39(8):657–673, July 2002.
- [121] T.J. Baker. Mesh generation for the computation of flowfields over complex aerodynamic shapes. *Computers & Mathematics with Applications*, 24(5-6):103–127, September 1992.
- [122] T-C. Wong. Mitigation of dynamic stall using small controllable devices. In *AHS Aeromechanics Specialists Conference 2010*, pages 915–932, 2010.
- [123] D.J. Mavriplis. Unstructured-mesh discretizations and solvers for computational aerodynamics. *AIAA Journal*, 46(6):1281–1298, 2008.
- [124] I.H. Abbott and A.E. Von Doenhoff. *Theory of Wing Sections: Including a Summary of Airfoil Data*. Dover Books on Physics and Chemistry. Dover Publications, 1959.
- [125] C.P. van Dam. Recent experience with different methods of drag prediction. *Progress in Aerospace Sciences*, 35(8):751–798, November 1999.
- [126] J.L. Price. *Unsteady Measurements and Computations on an Oscillating Airfoil with Gurney Flaps*. PhD thesis, North Carolina State University, 2001.
- [127] W. Maybury, M. Carrus, A. Visingardy, R. Donelli, S.C. van’t Hoff, R.J.J. Bakker, J.F. Hakkaart, J. Betran, M. Pavel, A. de Boer, A. Paternoster, and P. de Jong. GRC1.1 Technology Review Document. CS JU/ITD GRC/RP/1.1/31005. Technical report, GRC Report CS JU/ITD GRC/RP/1.1/31005, 2010.
- [128] L. Lee and T. Lee. Effect of Gurney Flap on Unsteady Wake Vortex. *Journal of Aircraft*, 44(4):1398–1401, July 2007.
- [129] C. Jang, J. Ross, and R. Cummings. Numerical Investigation of an Airfoil with a Gurney Flap, 1998.

-
- [130] Y. Li, J. Wang, and P. Zhang. Effects of Gurney Flaps on a NACA0012 Airfoil. *Flow, Turbulence and Combustion*, 68(1):27–39, 2002.
- [131] B.L. Storms and C. Jang. Lift enhancement of an airfoil using a Gurney flap and vortex generators. *Journal of Aircraft*, 31(3):542–547, May 1994.
- [132] D.R. Troolin, E.K. Longmire, and W.T. Lai. Time resolved PIV analysis of flow over a NACA 0015 airfoil with Gurney flap. *Experiments in Fluids*, 41(2):241–254, April 2006.
- [133] D. Jeffrey, X. Zhang, and D.W. Hurst. Aerodynamics of Gurney flaps on a single-element high-lift wing, March 2000.
- [134] S.A. Solovitz and J.K. Eaton. Dynamic Flow Response Due to Motion of Partial-Span Gurney-Type Flaps. May 2012.
- [135] S.A. Solovitz and J.K. Eaton. Spanwise Response Variation for Partial-Span Gurney-Type Flaps. May 2012.
- [136] A. Chakrabarti. *Engineering Design Synthesis: Understanding, Approaches and Tools*. Springer, 2002.
- [137] A. Chakrabarti, K. Shea, R. Stone, J. Cagan, M. Campbell, N.V. Hernandez, and K.L. Wood. Computer-Based Design Synthesis Research: An Overview, June 2011.
- [138] G. Pahl, W. Beitz, H.J. Schulz, U. Jarecki, K. Wallace, and L.T.M. Blessing. *Engineering Design: A Systematic Approach*. Solid mechanics and its applications. Springer, 2007.
- [139] C.W. Trowbridge. An overview of computer based design synthesis and optimisation. In *IEE Seminar Practical Electromagnetic Design Synthesis*, volume 1999, pages 1–1. IEE, 1999.
- [140] G. Diodati, M. Ciminello, and A. Concilio. Piezoelectric and electromagnetic solutions aimed at realizing an active Gurney flap. *Journal of Intelligent Material Systems and Structures*, August 2012.
- [141] C.G. Matalanis, B.E. Wake, D. Opoku, B-Y. Min, N. Yeshala, and L. Sankar. Aerodynamic Evaluation of Miniature Trailing-Edge Effectors for Active Rotor Control. May 2012.
- [142] C.P. Van Dam, D.T. Yen, R.L. Smith, and S.D. Collins. Microfabricated translational stages for control of aerodynamic loading. *US Patent 7028954*, 2006.
- [143] M. Brissaud, S. Ledren, and P. Gonnard. Modelling of a cantilever non-symmetric piezoelectric bimorph. *Journal of Micromechanics and Microengineering*, 13(6):832–844, November 2003.

- [144] M. Papila, M. Sheplak, and L.N. Cattafesta. Optimization of clamped circular piezoelectric composite actuators. *Sensors and Actuators A: Physical*, 147(1):310–323, September 2008.
- [145] D.A. Ende, B. Bos, and W.A. Groen. Non-linear electromechanical behaviour of piezoelectric bimorph actuators: Influence on performance and lifetime. *Journal of Electroceramics*, 22(1-3):185–191, March 2008.
- [146] Q. Yao, J. Dong, and P.M. Ferreira. Design, analysis, fabrication and testing of a parallel-kinematic micropositioning XY stage. *International Journal of Machine Tools and Manufacture*, 47(6):946–961, May 2007.
- [147] M. Jouaneh and R. Yang. Modeling of flexure-hinge type lever mechanisms. *Precision Engineering*, 27(4):407–418, October 2003.
- [148] K-B. Choi, J.J. Lee, and G.H. Kim. A miniaturized nano-motion stage driven by piezo stacks. In *2008 International Conference on Control, Automation and Systems*, pages 1321–1324. IEEE, October 2008.
- [149] K.-B. Choi, J.J. Lee, and M.Y. Kim. Cartwheel flexure-based compliant stage for large displacement driven by a stack-type piezoelectric element. In *2007 International Conference on Control, Automation and Systems*, pages 2754–2758. IEEE, 2007.
- [150] P.H. de Jong. *Power harvesting using piezoelectric materials – Applications in helicopter rotors*. PhD thesis, 2013.
- [151] A.J. Ferreira. *MATLAB Codes for Finite Element Analysis*, volume 157 of *Solid Mechanics and its Applications*. Springer Netherlands, Dordrecht, 2009.
- [152] D. Akcay Perdahcioglu. *Optimizing the dynamic behavior of structures using substructuring and surrogate modeling*. PhD thesis, Enschede, July 2010.
- [153] Forrester A.I.J., Sóbester A., and Keane A.J. *Engineering design via surrogate modelling: a practical guide*. John Wiley & Sons Ltd., 2008.
- [154] T.W. Simpson, T.M. Mauery, J.J. Korte, and F. Mistree. Kriging Models for Global Approximation in Simulation-Based Multidisciplinary Design Optimization. May 2012.
- [155] P. Bogaert. Comparison of kriging techniques in a space-time context. *Mathematical Geology*, 28(1):73–86, January 1996.
- [156] D. Zimmerman, C. Pavlik, A. Ruggles, and M. Armstrong. An Experimental Comparison of Ordinary and Universal Kriging and Inverse Distance Weighting. *Mathematical Geology*, 31(4):375–390, 1999.

-
- [157] D.E. Huntington and C.S. Lyrintzis. Improvements to and limitations of Latin hypercube sampling. *Probabilistic Engineering Mechanics*, 13(4):245–253, October 1998.
- [158] M.D. McKay, R.J. Beckman, and W.J. Conover. Comparison the three methods for selecting values of input variable in the analysis of output from a computer code. *Technometrics; (United States)*, 21:2, May 1979.
- [159] Y. Tian, B. Shirinzadeh, D. Zhang, and Y. Zhong. Three flexure hinges for compliant mechanism designs based on dimensionless graph analysis. *Precision Engineering*, 34(1):92–100, January 2010.
- [160] P. Koster. *Constructieprincipes voor het nauwkeurig bewegen en positioneren*. PPI, 2005.
- [161] L.L. Howell. *Compliant Mechanisms*. Wiley-Interscience publication. Wiley, 2001.
- [162] H.S. Kim, J.S. Son, and Y.T. Im. Gate location design in injection molding of an automobile junction box with integral hinges. *Journal of Materials Processing Technology*, 140(1-3):110–115, September 2003.
- [163] S. Henein. *Conception des guidages flexibles*. Collection Meta. Presses polytechniques et universitaires romandes, 2001.
- [164] C. Maier and T. Calafut. *Polypropylene: The Definitive User's Guide and Databook*. Plastics Design Library. Elsevier Science, 1998.
- [165] J.H. Kyung, B.G. Ko, Y.H. Ha, and G.J. Chung. Design of a microgripper for micromanipulation of microcomponents using SMA wires and flexible hinges. *Sensors and Actuators A: Physical*, 141(1):144–150, January 2008.
- [166] S. Zelenika, M.G. Munteanu, and F. De Bona. Optimized flexural hinge shapes for microsystems and high-precision applications. *Mechanism and Machine Theory*, 44(10):1826–1839, October 2009.
- [167] P.K. Johnson. Airfield Models - Hinges for Model Airplanes. http://airfieldmodels.com/information_source/model_aircraft_hardware/hinges.htm, 2012.
- [168] Matweb LLC. Online Materials Information Resource. <http://www.matweb.com>, 2012.
- [169] M.P. Luong. Fatigue limit evaluation of metals using an infrared thermographic technique. *Mechanics of Materials*, 28(1-4):155–163, July 1998.
- [170] H. Chen, G.Y. Grondin, and R.G. Driver. Characterization of fatigue properties of ASTM A709 high performance steel. *Journal of Constructional Steel Research*, 63(6):838–848, June 2007.

- [171] A. Berrehili, Y. Nadot, S. Castagnet, J.C. Grandidier, and C. Dumas. Multiaxial fatigue criterion for polypropylene – Automotive applications. *International Journal of Fatigue*, 32(8):1389–1392, August 2010.
- [172] Hardick B.V. Hardick - PTFE Transportbanden. <http://www.hardick.nl>, 2012.
- [173] A. Paternoster, R. Loendersloot, A. Boer, and R. Akkerman. Simulation of Flexible Mechanisms in a Rotating Blade for Smart-Blade Applications. In *Proceeding of the European Rotorcraft Forum*, pages 1–8, 2012.
- [174] J.L.M. Hensen. A Comparison of Coupled and Decoupled Solutions for Temperature and Air Flow in a Building. *ASHRAE Transactions*, (105):962–969, 1999.
- [175] M. Trčka, J.L.M. Hensen, and M. Wetter. Co-simulation for performance prediction of integrated building and HVAC systems – An analysis of solution characteristics using a two-body system. *Simulation Modelling Practice and Theory*, 18(7):957–970, August 2010.
- [176] LMS. LMS Virtual.Lab Motion simulation software. <http://www.lmsintl.com>, 2012.
- [177] E.C. Jameson. *Electrical Discharge Machining*. Society of Manufacturing Engineers, Machining Technology Association, 2001.
- [178] P. Giesen and N. van der Lee. Design of a flexure-based alignment device for adjustable and stable mounting of optical components. In *Proc. of SPIE Vol*, volume 5528, page 273, 2004.
- [179] K.H. Ho and S.T. Newman. State of the art electrical discharge machining (EDM). *International Journal of Machine Tools and Manufacture*, 43(13):1287–1300, October 2003.

Publications

Journal papers

Paternoster, A.R.A., Loendersloot, R., Boer, A. de & Akkerman, R. (2012). Geometrical optimization of a hingeless deployment system for an active rotor blade. *Journal of Intelligent Material Systems and Structures*.

Submitted papers

Paternoster, A.R.A., Loendersloot, R., Boer, A. de & Akkerman, R. (2012). Comparison of d33 patch actuators and Macro Fiber Composite actuators. *Journal of Intelligent Material Systems and Structures*.

Book chapters

Paternoster, A.R.A., Loendersloot, R., Boer, A. de & Akkerman, R. (2012). Smart actuation for helicopter rotorblades. In *Smart actuation and sensing systems - Recent advances and future challenges*.

Paternoster, A.R.A., Jong, P.H. de & Boer, A. de (2012). Piezoelectric energy conversions. In A. Reinders, J. Carel Diehl & H. Brezet. *The Power of Design, Product Innovation in Sustainable Energy Technologies*. John Wiley.

Conference presentations and proceedings

Paternoster, A.R.A., Loendersloot, R., Boer, A. de & Akkerman, R. (2012). Simulation of Flexible Mechanisms in a Rotating Blade for Smart-Blade

Applications. In Proceeding of the European Rotorcraft Forum. Amsterdam: ERF.

Paternoster, A.R.A., Loendersloot, R., Boer, A. de & Akkerman, R. (2011). Geometric optimisation of a gurney flap hinge-less deployment system for a helicopter model blade. In Proceeding of the European Rotorcraft Forum. Milaan, Italy: ERF.

Paternoster, A.R.A., Loendersloot, R., Boer, A. de & Akkerman, R. (2011). Geometric Optimisation of Hinge-less Deployment System for an Active Rotorblade. In Thomas Sattelmayer, Proceedings of ASME 2011 Conference on Smart Materials, Adaptive Structures and Intelligent Systems. Phoenix, USA: ASME.

Paternoster, A.R.A., Boer, A. de, Loendersloot, R. & Akkerman, R. (2010). Actuators for smart applications. In D. Brei & M. Frecker, Proceedings of ASME 2010 Conference on Smart Materials, Adaptive Structures and Intelligent Systems New York, USA: ASME.

Unpublished technical reports

Paternoster, A.R.A. (2012) Summary of Actuator Development Work at Twente University. GRC technical report CS JU/ITD GRC/RP/1.4/31034. University of Twente – Faculty CTW – Applied Mechanics group.

Paternoster, A.R.A. (2010) Piezo-Actuators for Gurney flap concept. In Maybury, W. et al., GRC1.1 Initial Technology Review Document. GRC technical report GRC-D111-1 GRC/RP/1.1/31005. University of Twente – Faculty CTW – Applied Mechanics group.

Paternoster, A.R.A., Boer, A. de & Akkerman, R. (2009) Actuator review for smart rotor blades. Technical report. University of Twente – Faculty CTW – Applied Mechanics group.

Paternoster, A.R.A., Boer, A. de & Akkerman, R. (2009) Piezo-Actuators for Synthetic-Jets. Technical report. University of Twente – Faculty CTW – Applied Mechanics group.

Acknowledgements

After four years of research, I am delighted and proud to present this work. I would like to seize the opportunity to acknowledge all the people who supported me during this process.

Firstly, I heartily acknowledge my promoter André de Boer, head of the Structural Dynamics and Acoustics group, who supported my ideas, encouraged my initiatives and helped me find a path between academic developments and research applications. Then, I would like to thank Remko Akkerman, head of the Production Technology group and co-promoter of this thesis, for inviting me to Enschede and for helping me to see the bigger picture of my research. Next comes Richard Loendersloot for his supervision and help on writing and presenting my work. On the experimental side, camarade and compatriote Laurent Warnet helped me manufacture the components needed for the experimental part of my work and was always enthusiastic to put new ideas into practice.

This project involved many industrial partners who greatly contributed to the completion of this work. Peter Wierach from the German Aerospace Center DLR is acknowledged for its participation in testing new piezoelectric materials from Physik Instrumente. Yves Lemmens from LMS is acknowledged for its collaboration and expertise for the dynamic simulation of a rotor blade in rotation. Partners of the Clean Sky European project are also acknowledged for their technical expertise and feedback during the various sessions hosted within the Green Rotorcraft Joint Technology Initiative. At the University of Twente,

Paul Lormans, from the Science and Technology faculty, is acknowledged for the manufacturing of components using spark erosion machining.

Four years as a PhD candidate are definitely not an easy journey, but I met great people and built strong friendships on this path. Many thanks to Debbie, secretary of the Structural Dynamics and Acoustics group for all the help you offered me since I arrived in Enschede. I am very grateful to my colleagues of the Applied Mechanics department for sharing their knowledge, and making the department a pleasant and stimulating working environment. Among them, a special thanks to my office mates, Pieter and Arjan. Pieter, thanks for your broad knowledge of the English language that greatly spiced up our discussion topics. Arjan, thanks for your every day investment in the group coffee breaks as an expert in speculaas and for standing by my side on the day of my defense. Juan, we went through a lot together: PhDs, bachelor parties, weddings (what's next?); thanks for taking part in my defense as a paranimf.

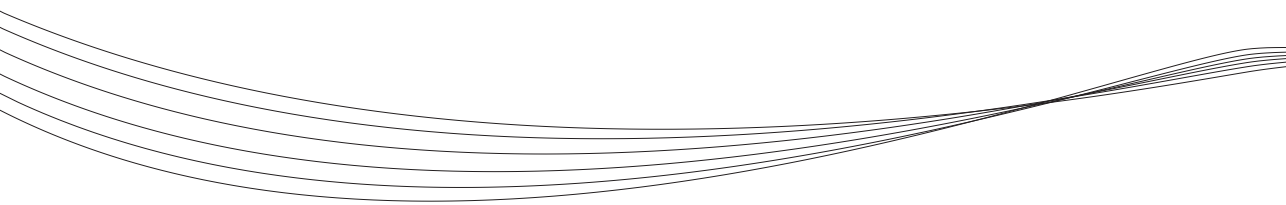
I would like to keep it short but still acknowledge all my friends from various organisations: the beer brewing club, the asocial club and the portuguese connection. I am also deeply thankful to Gérard, Paulette and José, my grand-parents, for their curiosity and faith in me; to Brigitte and Benoît, my parents, for their support and presence; to Régine and Jean-Philippe, my parents-in-law, for their interest and encouragements.

Charlène, I became the man I am today because you believed I could. Thanks for being always at my side and for helping me completing this work with your acute sense of beauty, balance and aesthetics. I love you first and foremost.

Merci à tous!

*"Success is not final, failure is not fatal:
it is the courage to continue that counts."*

Winston Churchill



UNIVERSITY OF TWENTE.